

**DISCONTINUOUS FINITE/BOUNDARY ELEMENT METHOD FOR
RADIATIVE HEAT TRANSFER WITH APPLICATION IN LASER CANCER
THERAPY**

By

XIAOMING CUI

A dissertation submitted in partial fulfillment of
the requirement for the degree of

DOCTOR OF PHILOSOPHY
(Mechanical Engineering)

WASHINGTON STATE UNIVERSITY
The school of Mechanical and Materials Engineering

DECEMBER 2005

© Copyright by XIAOMING CUI, 2005
All Rights Reserved

To the Faculty of Washington State University:

The members of the Committee appointed to examine the dissertation of XIAOMING CUI find it satisfactory and recommend that it be accepted.

Chair

ACKNOWLEDGMENTS

The author wishes to record here his indebtedness and gratitude to many who have contributed their time, knowledge and effort towards the fulfillment of this work. Particularly, he would like to express his heartfelt gratitude and thanks to Dr. Ben Q. Li for his invaluable guidance, supervision, encouragement and patience during the investigation.

The author would like to thank Dr. Robert F. Richards, Dr. Prashanta Dutta, and Dr. Hongming Yin for their input in the thesis, their time and energy to serve on the examination committee. The colleagues in the Dr. Li's Laboratory are also to be thanked for their assistance during the phase of the investigation.

The financial support of this work from the VLOC, Inc. (Grant No.: VAN00138704451) and by NASA (Grant #: NAG8-1693), and the school of Mechanical and Materials Engineering is gratefully acknowledged.

The author also wants to express his appreciation to his wife, Ying Liu, for her love, support and understanding throughout my studies. The author finally expresses his gratitude to his parents, Yue Cui and Huiying Wang, his family, his parents-in-law, his sisters, and his friends for their continuous support and encouragement.

**DISCONTINUOUS FINITE/BOUNDARY ELEMENT METHOD FOR
RADIATIVE HEAT TRANSFER WITH APPLICATION IN LASER CANCER
THERAPY**

Abstract

by Xiaoming Cui PhD.
Washington State University
December 2005

Chair: Ben Q. Li

The present study presents new algorithms that are developed on the basis of the boundary element method discontinuous or finite element formulation for the computation of thermal radiation problems. Since the external and internal thermal radiation problems are described using different mathematical formulations, based on the two different control equations of surface radiation exchanges (external thermal radiation) and radiative transfer in a medium (internal thermal radiation), the discontinuous boundary/finite element methods are developed to solve these two different type problems. The corresponding algorithms of thermal radiation for different geometries and applications are developed, and the coupling problems are also presented.

A Galerkin boundary element numerical method for surface radiation exchange has been developed in this study, which includes 1) two dimensional geometries without/with blockages and 2) three dimensional geometries without/with blockages. The parallel algorithm for boundary element method is also developed by PVM (Parallel Virtual Machine). For integral radiative heat transfer problems, the discontinuous finite element

method is implemented to solve one-dimensional and multidimensional problems. These include 1) one-dimensional problems with emitting, absorbing, and/or scattering effects. 2) Two dimensional and three dimensional problems with emitting, absorbing, and/or scattering effects. 3) Axisymmetric problems with emitting, absorbing, and/or scattering effects. For internal radiative heat transfer problems, the parallel computation techniques are also developed for discontinuous finite element method. 4) Numerical simulations of radiative transport in laser hyperthermia.

The techniques we developed for calculating the external and internal radiation problems are proved more accurate and faster, compared with the techniques being used commonly, and the methodologies are easy to couple with calculations of heat transfer and fluid flow.

TABLE OF CONTENTS

	Page
ACKNOWLEDGEMENTS.....	iii
ABSTRACT.....	iv
LIST OF FIGURES.....	ix
LIST OF TABLES.....	xxi
NOMENCLATURE.....	xvii
CHAPTERS	
1. INTRODUCTION.....	1
1.1. INTRODUCTION.....	1
1.2. LITERATURE REVIEW	4
1.3. OBJECTIVES OF PRESENT RESEARCH	12
1.4. SCOPE OF PRESENT RESEARCH	14
2. PROBLEM STATEMENT.....	16
2.1. RADIATION HEAT EXCHANGE IN COMPLEX GEOMETRIES.....	19
2.2. INTERNAL RADIATION HEAT TRANSFER	21
3. TWO-DIMENSIONAL SIMULATION OF SURFACE RADIATION EXCHANGE BETWEEN GREY SURFACES.....	28
3.1. INTRODUCTION.....	30
3.2. PROBLEM STATEMENT.....	31
3.3. THE GALERKIN BOUNDARY ELEMENT METHOD.....	36
3.4. THE SEARCHING AND SORTING ALGORITHM	37

3.5. RESULTS AND DISCUSSION.....	46
4. 3-D SIMULATION OF RADIATION EXCHANGE BETWEEN GREY SURFACES	53
4.1. INTRODUCTION.....	53
4.2. SHADOWING ALGORITHM.....	54
4.3. PARALLEL COMPUTING ALGORITHM AND ITS IMPLEMENTATION..	69
4.4. COUPLED WITH FE FOR MIXED MODE HEAT TRANSFER PROBLEMS.....	71
4.5. RESULTS AND DISCUSSION	75
4.6. CONCLUDING REMARKS.....	88
5. ONE-DIMENSIONAL RADIATIVE HEAT TRANSFER IN PARTICIPATING MEDIA.....	90
5.1. INTRODUCTION	90
5.2. DISCONTINUOUS FINITE ELEMENT FORMULATION	92
5.3. COUPLING OF CONVENTIONAL AND DISCONTINUOUS FINITE ELEMENTS.....	97
5.4. RESULTS AND DISCUSSION.....	101
5.5. CONCLUDING REMARKS.....	116
6. A DISCONTINUOUS FINITE ELEMENT FORMULATION FOR MULTI-DIMENSIONAL RADIATIVE TRANSFER IN ABSORBING, EMITTING AND SCATTERING MEDIA.....	117
6.1. INTRODUCTION.....	117
6.2. THE DISCONTINUOUS FINITE ELEMENT FORMULATION.....	118

6.3. NUMERICAL IMPLEMENTATION.....	124
6.4. 3-D CALCULATIONS.....	131
6.5. PARALLEL ALGORITHM.....	135
6.6. RESULTS AND DISCUSSION	139
7. A DISCONTINUOUS FINITE ELEMENT FORMULATION FOR RADIATIVE TRANSFER IN AXISYMMETRIC FINITE CYLINDRICAL ENCLOSURES AND COUPLING WITH OTHER MODE HEAT TRANSFER	160
7.1. INTRODUCTION.....	160
7.2. INTERNAL RADIATION HEAT TRANSFER.....	162
7.3. THE DISCONTINUOUS FINITE ELEMENT FORMULATION.....	164
7.4. NUMERICAL IMPLEMENTATION.....	172
7.5. RESULTS AND DISCUSSION	186
7.6. CONCLLUDING REMARKS.....	199
8. NUMERICAL SIMULATIONS OF RADIATIVE HEAT TRANSFER IN LASER HYPERTHERMIA	201
8.1. INTRODUCTION	201
8.2. RESULTS AND DISCUSSION	208
8.3. CONCLUSION REMARKS.....	219
BIBLIOGRAPHY.....	221

LIST OF FIGURES

	Page
Figure 2.1 Schematic of thermal radiation exchange between two surfaces A_i and A_j	18
Figure 2.2 Schematic representation of internal radiation heat transfer.....	21
Figure 2.3 Schematic illustrations for opaque diffuse boundary condition	24
Figure 2.4 Schematic of symmetric boundary condition	25
Figure 2.5 Schematic illustration of periodic boundary condition.....	26
Figure 3.1 Schematic of thermal radiation exchanges: exchange among surfaces in an enclosure.....	31
Figure 3.2 Geometric relations between mutually seen and unseen elements: radiation emitted from point i can reach point j but is unable to reach point j' because of the self-blockage by the element J'	39
Figure 3.3 Primary and second clip windows for screening out third party shadowing elements for blocking the radiation exchange between elements I and J	40
Figure 3.4 Three geometric arrangements for third party obstruction of radiation exchange between point i and element J in relation with the testing triangle: (a) no obstruction, (b) total obstruction and (c) partial obstruction.....	42

Figure 3.5	Detailed testing of blockage of radiation between points i and j by a third party element K.....	44
Figure 3.6	Comparison of strategies for detecting third party shadowing by the traditional and Galerkin boundary element methods. The traditional method uses the triangle formed by 1'12, where the Galerkin used triangle 1'12 and other triangles such as a12	45
Figure 3.7	Boundary element mesh and comparison of numerical and analytical solutions of thermal radiation exchange in a simple 2-D geometry: (a) heat flux along bottom wall, (b) along side wall and (c) along bottom wall. Parameters used for calculations: $\varepsilon=0.5$ for all the walls, $L=3m$, and other conditions and boundary discretization are shown in the insert of figure 3.7(a).....	49
Figure 3.8	Heat flux distributions for a 2-D cavity with three protrusions that result in partial or total blocking of radiation between some surfaces of the enclosure. Parameters used for calculations: $\varepsilon=0.5$ for all walls, $T=400$ K at, left side and bottom walls, and $T=900$ K at the rest.....	51
Figure 4.1	unseen surfaces	57
Figure 4.2	3 rd blocking out of primary clipping window	59
Figure 4.3	Four different scenarios of third party element blockage of thermal rays emitted from point i to element J : (a) no third part blocking; (b) total third part blocking; (c) and (d) partial third part blocking.....	63
Figure 4.4	Check if P is in the plane.....	64

Figure 4.5	Procedures used to determine the blockage of the thermal ray emitted from i to j by element K : (a) element K is not parallel $\mathbf{m} \cdot \mathbf{n}_k \neq 0$ to the thermal ray ij and k is the interception point between the thermal ray and element K ; and (b) third party elements are parallel $\mathbf{m} \cdot \mathbf{n}_k = 0$ to the thermal ray ij , and element K blocks thermal ray ij , but element L does not.	65
Figure 4.6	Flow chart for the searching and adaptive integration algorithm used for surface radiation calculations.	68
Figure 4.7	Schematic of master–slave communication in parallel processing.	70
Figure 4.8	Illustration of geometry of furnace	71
Figure 4.9	(a):Boundary element meshes. (b): calculated heat flux distribution on the top wall for a 3-D enclosure (dimensions: 2m x 1m x 0.5m). Parameters used for calculations: $\varepsilon = 0.5$ and $T=700$ K for top wall; $\varepsilon = 0.5$ and $T=300$ K for all side walls, and $\varepsilon = 0.1$ and $T=400$ K for bottom wall. The analytically calculated heat flux for the bottom wall is -466.4129w/m^2	78
Figure 4.10	Surface radiations in an enclosure with one internal obstruction. Conditions used for calculations: the temperature of outer enclosure is at 1700 K, the inner block is at 1400 K, the emissivity of all surfaces is 0.8; the outer enclosure is $1.2 \times 1.2 \times 1.2 \text{ m}^3$, the temperature used to normalize the heat flux is 1400 K, and the inner block is $0.4 \times 0.4 \times 0.4\text{m}^3$ located at the centre of the enclosure. The front surface is removed for the purpose of illustration.	80

Figure 4.11 Surface radiation calculations in a complex 3-D geometry: (a) meshes and thermal conditions used for calculations; (b) heat flux on the left lateral surface of the enclosure; and (c) heat flux on the top surface of the enclosure. The dimension of the enclosure is $1.2 \times 1.2 \times 1.2 \text{ m}^3$ and the temperature used to normalize the heat flux is 1400 K. Emissivity of all surfaces is 0.5 and side surface temperatures of the internal obstructions vary from 400 to 1700 K. The front surface is removed for the purpose of illustration..... 82

Figure 4.12 Performance of parallel computations for the 3-D surface radiation exchange problems: (a) CPU time (log time in s) versus the number of processors used with different numbers of elements; and (b) expense budget of CPU times for searching and numerical integration. The CPU times exclude those used for matrix inversion by the LU decomposition. The geometry and thermal conditions used for the computations are given in Figure 4.10(a)..... 84

Figure 4.13 Calculated results of mixed mode heat transfer in an industrial furnace using the coupled Galerkin boundary/finite element method: (a) temperature distribution in the furnace; (b) body-cut view of temperature distribution; (c) body-cut view of velocity distribution in the liquid pool—maximum velocity is 1.9 mm/s; and (d) particle trajectory plot. Parameters for calculations: liquid pool is $0.15 \times 0.3 \times 0.3 \text{ m}^3$ and filled with Ga melt. The top surface temperature is 340 K and the environment is at 295 K. The emissivity of all surface is 0.5

and the thermal conductivity and specific heat of the furnace walls are 10 W/m K and 130 kJ/kg K, respectively. The gravity is in the opposite x-direction (see Figure 4.8)..... 88

Figure 5.1 Schematic illustrations of one-dimensional radiative heat transfer problems..... 90

Figure 5.2 Thermal radiation in a slab filled with an absorbing and scattering medium..... 93

Figure 5.3 Thermal radiation in a slab filled with an absorbing and scattering medium..... 102

Figure 5.4 Radiation intensity distributions calculated by analytical solutions, two flux model, and the discontinuous finite element method with linear and constant elements. Parameters used for calculations: two 1-D plates, $T_2=T_1=0$ K, the emissivity of the plates=1.0, $\kappa=1.0$, $\sigma=0$. The temperature of media is 100 K..... 102

Figure 5.5 Computed results for the distributions of heat fluxes and (b) divergence of radiative heat fluxes (divq). The parameters used for calculations are the same as in Figure 5.4. 104

Figure 5.6 Convergence rate of the discontinuous method, measured by L_2 -error norm vs. the mesh size with (a) uniform mesh distribution (b) non-uniform mesh distribution. Parameters used for calculations: $T_2=T_1=0$ K, the emissivity of both plates is 1.0. $\kappa=1.0$, $\sigma=0$. The temperature of media is 100 K in case (a), but $T=100*(z-0.5)^{1/2}$ in case (b)..... 107

Figure 5.7 Mesh convergence for the local h-adaptive mesh refinement for radiative heat transfer calculations. Parameters used for calculations are as same as Figure 5.6(b).. 110

Figure 5.8 Effect of scattering on the radiative heat transfer in participating media between two infinite long plates: (a) intensity distribution, (b) heat flux distribution, (c) divergence of heat flux distribution and (d) boundary heat flux distribution. Parameters used for calculations are same as Figure 5.4, but the σ varies with different cases. In (d), The results of DFE are compared with the reported results in [Siegel, 1992], where $Q = q_r / (\sigma T_g^4 - \sigma T_s^4)$ is the non-dimensionalized radiative heat flux and ω is the scattering albedo. The parameters are used in this case $T_g=100$ K, $T_1 = T_2 = T_s = 0$ K, the emissivity of both plates is 1.0..... 113

Figure 5.9 Dependence of temperature distribution across the slab on the radiation number N. Combined heat conduction and internal radiation are considered. The parameters used for calculations as the same as in Figure 5.4, except that $T(0)=1$, $T(L)=0.5$ 115

Figure 6.1 Schematic representation of radiative transfer in a participating medium and definition of the direction of radiation intensity and symmetry boundary condition..... 119

Figure 6.2 Illustration of discontinuous finite-element formulation for 2-D internal radiation transfer in absorbing and emitting media using unstructured triangular meshes: (a) element i, its boundary normals, and its

	neighboring elements; (b) local node number and side number of a typical triangular element (or i th element).....	120
Figure 6.3	Schematic sketch of discontinuous finite-element broken space.....	122
Figure 6.4	Illustration of discontinuous finite-element formulation for 3-D internal radiation transfer in absorbing and emitting media using unstructured tetrahedral meshes: (a) element i , its surface normals, and its neighboring elements; (b) local node number and side number of a typical tetrahedral element (or i th element).....	132
Figure 6.5	Two types of partitioning for parallel computation of internal radiation transfer problems: (a) domain decomposition; (b) solid-angle decomposition.....	137
Figure 6.6	Master-slave concept used for parallel implementation of discontinuous finite element formulation for internal radiation transfer problems.....	138
Figure 6.7	(a) Illustration of temperature distribution and boundary condition of two dimensional case. (b) Unstructured mesh for two dimensional case, which consists of 1,142 triangle elements. (c) Schematic illustration of angular space discretization. $0 \leq \theta \leq \pi$, $0 \leq \phi \leq 2\pi$, $\mathbf{s} = \sin \theta \cos \phi \hat{i} + \sin \theta \sin \phi \hat{j} + \cos \theta \hat{k}$. (d) The heat flux q_x distribution respect to x/L obtained by DFE method is compared with analytical solution at various extinction coefficients $\beta = 0.1$, $\beta = 0.5$ and $\beta = 1.0$	141

Figure 6.8 (a) Schematic illustration of unstructured mesh for 2-D irregular domain, which consists of 2473 triangle elements. (b) Comparison of heat flux on the boundary $y=0.0$ between DFE method and Ray tracing method at different absorption coefficients $k=0.1$ and $k=1.0$ 144

Figure 6.9 (a) Schematic illustration of unstructured mesh for the 3-D case, which consists of 2313 unstructured tetrahedral elements. The temperature of media T is constant and all walls are black and cold. (b) Comparison of heat flux q_z^* respect to x/L at middle line of top surface $y/L=0.5$, and $z/L=1.0$. The extinction coefficient varies from $\beta=0.1$ and $\beta=1.0$ 147

Figure 6.10 (a) Illustration of scattering functions of different models. (b) Comparison of heat flux q_z^* distribution on the top surface of cube $y/L=0.5$, and $z/L=1.0$ with isotropic scattering between DFE, FVM and Monte Carlo method. The scattering coefficient is 0.5. (c) Comparison of heat flux q_z^* distribution on the top surface of cube $y/L=0.5$, and $z/L=1.0$ with anisotropic scattering between DFE and Monte Carlo method. The different scattering functions are chosen and extinction coefficient is 1.0. (d) Comparison of heat flux q_z^* distribution on the top surface of cube $y/L=0.5$, and $z/L=1.0$ with anisotropic scattering between DFE and Monte Carlo method. The different scattering functions are chosen and extinction coefficient is 2.0..... 151

Figure 6.11	3-D discretization and calculated radiative heat flux q^* along the middle line of top surface $y/L=0.5$, and $z/L=1.0$. (a) The cube is discretized with 3072 tetrahedral elements, or 1024 wedge elements, or 512 hexahedral elements or 736 elements of mixed hexahedra and pentahedra. (b) Comparison of radiative heat fluxes calculated using different meshes shown in (a). The absorption coefficient varies from $\kappa = 0.1$ to $\kappa=1.0$. (c) Comparison of the DFE and the Finite Volume methods for the solution of RTE for $\kappa = 10$	156
Figure 6.12	The CPU time respect to the number of CPUs in parallel computation ...	159
Figure 7.1	Radiative transfer in axisymmetric geometry and the cylindrical coordinate system used for numerical analysis.....	162
Figure 7.2	Domain and element types used for axisymmetric radiative transfer calculations: (a) the 3-D domain generated by the rotation of the axisymmetry plane and (b) three types of 3-D elements used for the discontinuous finite element formulation.....	166
Figure 7.3	(a) Schematic illustration of the mesh of DFE formulation for radiation in absorbing and emitting media. (b) Local node number and side number of a typical triangular element used for discontinuous finite element formulation of internal radiation transfer problems.....	170
Figure 7.4	Illustration of axisymmetric and periodic conditions used in mapping procedure for axisymmetric radiative transfer calculations.....	179
Figure 7.5	Computed non-dimensional heat flux distribution along the sidewall of a finite cylinder: (a) comparison with the results reported in the	

literature at $\kappa=0.1$, $\kappa=1.0$ and $\kappa=5.0$ and (b) effects of angular discretization on calculated wall heat flux distribution. 190

Figure 7.6 Radiative transfer in an irregular quadrilateral of axisymmetry: (a) structured mesh consisting of 400 structured triangular elements and (b) comparison of heat flux q^* on the wall (defined by points (0.5, 1.0) and (1.5, 1.2)) calculated by the DFE and finite volume methods for different absorption coefficients, $\kappa=0.1$, $\kappa=1.0$ and $\kappa=5.0$ 191

Figure 7.7 Computed results for radiative transfer in a cylinder filled with scattering media: (a) scattering phase functions and (b) comparison of heat flux distribution on the side wall between DFE and Discrete Ordinates method for different scattering phase functions (Isotropic, F2, F3, B1, and B2). Conditions used for calculations: $\beta =1.0$ and $\omega=1.0$ 193

Figure 7.8 Coupled FE/DFE calculation of mixed-mode heat transfer in a rotating cylinder filled with semi-transparent melt: (a) schematic representation of the mixed mode problem involving swirling flows, (b) and (c) distribution of the temperature field and flow field for $\kappa=0.1$ m-1, (d) and (e) distribution of the temperature field and flow field for $\kappa=10$ m-1. Conditions used for calculations are as follows: rotating speed $\omega=0.05$, $R=0.05$ m, and $H= 0.05$ m. All the boundaries are black. The side wall ($R=0.05$ m) temperature is fixed at $T=1300$ K, and the bottom surface ($H=0$ m) temperature is 1250K. The ambient temperature is

	$T_{amb} = 1240$ K and $\varepsilon = 1$. The material properties are: $\rho = 4073$ kg/m ³ , k=4.0 W/m·K, $\mu = 0.046$ kg/s·m, and Cp=687.0 J/kg·K.....	196
Figure 8.1	Schematic illustration of tumor, normal tissue and laser beam.....	209
Figure 8.2	Illustration of ideal model for numerical simulation.....	210
Figure 8.3	Radiative heat flux divergence at both absorption and scattering coefficients of tissue and cancer are 1.0.....	212
Figure 8.4	Distribution of the radiative heat flux at the following optical parameters: The absorption coefficient of skin is 0.5, scattering coefficient is 1.0; the absorption coefficient of cancer is 1, scattering coefficient is 10.0...	213
Figure 8.5	The distribution of the radiative heat flux divergence for three different laser beam schemes; the absorption coefficient of the normal tissue is 0.01cm^{-1} , and the scattering coefficient of the normal tissue is 10cm^{-1} ; the absorption coefficient of the tumor is 0.05cm^{-1} , and the scattering coefficient of the tumor is 50cm^{-1} . (a): one laser beam, and the intensity of is $10000\frac{w}{\text{cm}^2\text{sr}}$. (b) two laser beams, and the intensity of each laser beam is $5000\frac{w}{\text{cm}^2\text{sr}}$; (c) four laser beams, and the intensity of each laser beam is $2500\frac{w}{\text{cm}^2\text{sr}}$	216
Figure 8.6.	The distribution of the radiative heat flux divergence for three different laser beam schemes; the absorption coefficient of the normal tissue is 0.01cm^{-1} , and the scattering coefficient of the normal tissue is 10cm^{-1} ; the absorption coefficient of the tumor is 0.25cm^{-1} , and the scattering	

coefficient of the tumor is 250cm^{-1} . (a) one laser beam, and the intensity of is $10000\frac{w}{\text{cm}^2\text{sr}}$. (b) two laser beams, and the intensity of each laser beam is $5000\frac{w}{\text{cm}^2\text{sr}}$; (c) four laser beams, and the intensity of each laser beam is $2500\frac{w}{\text{cm}^2\text{sr}}$ 218

LIST OF TABLES

Table 6.1 the expansion coefficients for the phase functions.....	164
---	-----

NOMENCLATURE

A, B, C, D	matrix
c_0	speed of light
A or Ae	area
d	distance
E_b	blackbody emissive power
F or K	matrix
f_{ij}	the ij-th element of matrix f
H	length of element sides or characteristic length of geometry
h	Plank constant
I	radiation intensity
J	Jacobian
j	jth node
K	view factor
K_{ij}	the ij-th element of matrix K
L	length of 2-D element side or distance between two plates
m	the ith element of mesh
n	normal of boundary
N	total number of control angles or radiation parameter
\mathbf{n}, \mathbf{n}_w	outnormal of boundary, wall normal
NB	neighboring element
Nd	number of the boundaries of an element

N_g	number of integration points
N_j	number of discretized polar angles
N_s	number of phase function terms
q	heat flux
q^*	nondimensionalized heat flux
q, q'''	heat flux, heat source
R	rotating matrix
\mathbf{r}	coordinates
r, z	cylindrical coordinates
S	source function
\mathbf{s}, \mathbf{s}'	direction vector for radiative intensity
\mathbf{t}	tangential vector
T	temperature
t	time
T_{ref}	reference temperature
\mathbf{u}	velocity vector
V	volume
w	weights of integration quadrature

Greek

β	extinction coefficient
κ	absorption coefficient

ε	emissivity
λ	frequency
σ_b	Stefan-Boltzmann constant
σ	scattering coefficient
θ	polar angle measured from the z-axis or azimuthal angle
ϕ	azimuthal angle measured from the x-axis, shape function
Φ	scattering phase function
φ	polar angle
Γ	boundary
ρ	reflectivity
ω	scattering albedo
Ω, Ω'	radiation direction
$\Delta\Omega$	control angle

Subscripts and superscripts

b	black body
e	element
l	the l th direction of radiation
R	radiation
p	on the middle plane

ref	referenced value
φ	in φ direction
*	symmetric vector or non-dimensionalized value

CHAPTER 1

INTRODUCTION

1.1 INTRODUCTION

Thermal Radiation is becoming more important in a wide range of engineering research and applications. This importance arises from several areas: combustion processes, high-temperature phenomena in hypersonic flows, energy transfer in propulsion systems, solar energy devices, space station power systems, energy leakage in cryogenic systems, high temperature single crystal growth processes, and laser applications, and many others. [Modest, 1993]. The importance of the thermal radiation has motivated the need to develop useful engineering tools with which information on energy transport can be obtained for system design and energy performance improvement. The radiation problems can be divided into two different categories, the first one is the thermal radiation exchange between surfaces that are separated by vacuum or by a transparent medium. The examples include crystal furnaces, solar energy devices, etc. The second category is radiative transport in an absorbing, emitting, and/or scattering medium. Examples in the heat transfer area include the burning of any fuel, rocket propulsion, nuclear explosions, and laser transport in biological materials. The former is referred to as external radiation, while the latter is internal radiation. The mathematical formulations

are different for these two cases, which naturally lead to the use of different approaches to their solutions.

Surface radiation exchanges play an important role in many high temperature materials processing systems. Some of these processing systems involve complex geometric arrangements that either are designed to obstruct radiation exchanges or are an integral part of an overall thermal system design. Accurate prediction of surface radiation exchange phenomena and their effects on other heat transfer modes in these processing systems is of vital importance, since it is the fundamental understanding of the physics that controls the processes, and it is the development of guidelines for optimizing the performance of the existing processes and designing the new generation of energy efficient processing systems.

Radiative transport in medium describes the energy transport in an intervening medium that directly affects the radiation transfer via mechanisms of absorption, emission and scattering, this kind of radiation is also named internal radiation. For the problems of radiative transfer in a participating medium, the absorption, emission and/or scattering effects must be considered in order to provide an accurate estimate of thermal energy transfer in the system [Modest 1993].

The intention of this study is to describe the algorithms that are developed on the basis of the boundary element or discontinuous Galerkin finite element formulations for the computation of thermal radiation problems. Since the external and internal thermal

radiation problems are described using different mathematical formulations, based on the two different control equations of surface radiation exchanges and radiative transfer in a medium, the discontinuous boundary/finite element methods are developed to solve these two different type problems. The corresponding algorithms of thermal radiation for different geometries and applications are developed, and the coupling problems are also presented.

In this study, the boundary element numerical method developed for surface radiation exchange is presented, which includes 1) two dimensional geometries without/with blockages 2) three dimensional geometries without/with blockages. The parallel algorithm for boundary element method is also developed by PVM (Parallel Virtual Machine) language. For radiative heat transfer in media problems, the discontinuous finite element method is implemented to solve one-dimensional and multidimensional problems. These include 1) one dimensional problems with emitting, absorbing, and/or scattering effects. 2) Two dimensional and three dimensional problems with emitting, absorbing, and/or scattering effects. 3) Axisymmetric problems with emitting, absorbing, and/or scattering effects. For internal radiative heat transfer problems, the parallel computation techniques are also developed for discontinuous finite element method. 4) Simulation of laser transport in laser hyperthermia.

The techniques we developed for calculating the internal and surface radiation problems are proved more accurate and faster, compared with the techniques being used

commonly, and the methodologies are easy to couple with calculations of heat transfer problems and fluid flow.

1.2 LITERATURE REVIEW

An accurate determination of radiation energy exchange among surface elements in an enclosure is of crucial importance for a wide range of engineering applications that involve heat transfer, illumination design and applied optics. Examples of these applications include combustion processes, high-temperature phenomena in hypersonic flows, energy transfer in nuclear propulsion systems, high temperature single crystal growth processes, etc. [Modest 1993, Siegel *et al.* 1992]. The importance of the thermal radiation exchange has motivated the need to develop useful analytical and numerical techniques to enhance our understanding of the fundamentals governing the surface energy radiation exchanges and to provide rational guidelines for process improvements and system optimization.

In order to calculate the energy exchange in an enclosure, there are several different techniques have been developed in last decade. Sparrow (1960) developed a variational method to solve the surface heat exchange problems. Monte Carlo method developed by Howell and Perlmutter (1964) is the first numerical technique to solve the radiation heat exchange problems, and Naraghi and Chung (1984) extended Monte Carlo method by using statistical theory to diffuse and specular surfaces. Based on an

assumption that the surfaces of enclosure are flat and the temperature of surface is constant, Hottel (1931) introduced a net radiation method. The basic idea is that the net radiant heat flux between two surfaces of enclosure is constant, and which is only decided by the temperature and emissivity of the surface and the relative geometric position of these two surfaces. In the calculation of surface radiation exchange, the quantity used to describe the geometric position between surfaces is named view factor, or angle factor. By discretizing the surfaces of enclosure, the view factor between discretized surfaces can be calculated numerically or analytically. Due to the difficulty to analytically calculate view factor of complex geometries in engineering applications, the numerical methods are widely used in the engineering community, and several different numerical techniques to solve view factors have been developed and proved to work well.

Since the calculation of view factor is a geometric problem, several numerical schemes have been derived from computer graphics area. Nusselt (1928) developed unit sphere method which is from computer graphics applications. Emery *et al.* (1987) first developed a numerical scheme to solve view factor for the intrusion geometries by using computer graphics techniques. Finite element method is another great technique to calculate view factors in last several years. Chung and Kim (1982) used finite element method to directly solve radiant heat exchange based on net flux, but their method is based on the assumption that the temperature of surface is constant, which can not solve real problems in engineering. Breitbach *et al.* (1990) introduced a finite element solution

for view factor based on the variational theory, but slow convergence speed and the error increased with increasing the order of integration. Kuppurao and Derby (1993) developed a Galerkin finite element to solve view factor to solve diffuse grey surface radiation, but they didn't consider the most important and difficult problems in the calculation of view factor, blocking.

The boundary integral formulation represents a natural approach to surface radiation exchange calculations in that the energy exchange takes between the surface elements and requires the information along the surface only. The use of the boundary element method for this purpose has been explored recently by Blobner *et al.* (2001). Their studies presented a *traditional* boundary element integral formulation for the thermal radiation heat transfer and coupled it with conduction for 2-D geometries. In their algorithm, as in many others, extreme caution has been exercised in treating the kernel function, which experiences abrupt discontinuity when a ray of radiation emitted from one surface to another is blocked by a geometric obstruction. In their studies, a coupled solution is also presented for a problem that involves a mixed mechanism of conduction and surface radiation. One critical drawback associated with the application of the traditional boundary element method for this type of calculations is the detection of the geometric obstruction may not be exclusive in some complex geometric arrangements, thereby causing numerical errors in the calculation of the kernel function and hence the prediction of the energy exchanges. Nonetheless, their work has clearly demonstrated that

the boundary element method can be a very powerful tool for thermal radiation interchange calculations.

In this study, a novel algorithm for the prediction of surface radiation energy inter-exchanges between gray surfaces is presented. The work is motivated by the need to further improve the computational efficiency by taking advantage of updated development in both computer hardware and software algorithms. It also constitutes part of effort in developing integrated solutions to engineering problems arising from materials processing and manufacturing systems that involve multi-physics and multi-time and multi-length scale phenomena. Unlike the Blobner's (2001) method, the approach we developed is based on the Galerkin boundary element method, which improves the traditional method, and allows a full detection of any geometric blockages between any two points at two surfaces involving the radiation exchange. The method is further enhanced with an efficient searching and sorting algorithm developed based on the accumulated experience with suitable data structure (Bastian and Li 2002), and computer graphics (Rogers 1998, Foley 1997, Zhang 2001, Honda *et al.* 2001) to increase the computational efficiency for blockage detection, which turns out to be the most CPU consuming part of all the calculations. It is stressed here that the *Galerkin*, rather than *traditional*, boundary integral formulation, is essential to ensure that the geometric obstruction is fully detected in any complex geometries. In what follows, the Galerkin boundary integral formulation is presented, along with the design of shadowing

determination algorithm, based on sorting and searching schemes used in advanced computer graphics. The coupling of the Galerkin boundary element method with the Galerkin finite element method for the solution of heat transfer problems involving mixed mechanisms such as conduction, convection and surface radiation is presented. The algorithm we developed should form a strong basis to study the principles of surface radiation exchanges and will help engineering designs involving surface radiation heat transfer.

Internal thermal radiation is a significant mode of heat transfer, which describes the energy transport in an intervening medium that directly affects the radiation transfer via mechanisms of absorption, emission and scattering. Some of the engineering thermal systems in which thermal radiation plays a crucial role include the growth of optical single crystals from high temperature melts [Song and Li, 2003], the particle laden high temperature fluidized bed combustion systems, and the space crafts upon re-entry. Radiation heat transfer is not only important in high temperature applications, but also in remote sensing, laser measurement, and the applications in which the energy transfer is interacting with participating media.

Thermal radiation in participating media is governed by the radiation transfer equation of hyperbolic type, which describes the optical energy balance along a thermal ray. Owing to the importance of internal radiation transfer in thermal engineering

applications, many numerical techniques have been developed to predict the phenomena and to assist in thermal designs involving radiative heat transfer.

Monte Carlo [Steward and Cannon, 1971] is one of the most accurate methods to solve the radiative heat transfer problems. This method is based on one-dimensional differential equations of RTE. By solving the intensity along arbitrarily oriented rays, the radiative heat transfer problems can be solved very accurately, but a lot of computational times and memory are needed, these disadvantages limit Monte Carlo method applications, and not popular in engineering community.

One of the early used numerical algorithms is the two-flux method, which was introduced by Schuster (1905) and Schwarzschild (1906) for solving one-dimensional radiative heat transfer problems. The two-flux method approximates the radiation intensity with two directions in one-dimensional problems. In multiple-dimension problem, intensity is approximated in each of coordinate direction, and kept the same positive or negative sign with coordinates. Based on this approximation, the intensity is uniform in every flux direction. By using this method, the Radiative Transfer Equation is reduced to two ordinary differential equations, which can be easily solved analytically or numerically. Apparently the accuracy of this approximation is not good, since in real radiation problems, the intensity is anisotropic in every direction, but this method is very simple and easy to understand.

Since the two-flux method is not accurate to solve radiative heat transfer problems, Chandrasekhar (1960) proposed the discrete-ordinates method, which was developed from neutron transport applications. Fiveland (1982) first reports the discrete-ordinates method to solve radiative heat transfer problem in axisymmetric enclosure, and after that, a lot of research on the discrete-ordinates method were reported. The discrete-ordinates can be considered as the extension of the two-flux method, since instead of limited number of directions in the two-flux method, the discrete-ordinates method divided the 4π solid angles to much more ordinates. The number of ordinates can be arbitrary, but in convenience to integrate, the control angles usually are set a quadrature set, which is a collection of the discrete ordinate directions and the corresponding weight, and the quadrature set will affect the accuracy of simulations [Lathrop and Carlson, 1964, Fiveland, 1991]. The discrete-ordinates method reduces RTE to by a set of coupled differential equations at the discrete ordinate directions; therefore, the accuracy is better than the two-flux method.

The finite volume method is originally designed to solve fluid mechanic and convective heat transfer problems, and Raithby and Chui (1990) developed the finite volume model for radiative heat transfer problems. The finite volume method is based on the control volume method, the basic idea is to discretize the RTE in every control volume and control angle so that radiation energy can keep conservation. The finite volume method is the similar to the discrete ordinates method, both of them can be also

considered as an extension of the two-flux method. The difference is the finite volume method can use arbitrary control angle discretization, but the discrete ordinates method has to choose a certain quadrature set.

Discontinuous Galerkin finite element (DFE hereafter) methods, also called discontinuous Galerkin methods, have undergone rapid development recently and become increasingly popular in the numerical computational community. A comprehensive review of the history, development and current trends of discontinuous finite elements has been presented by Cockburn, et al. (2000). The DFE methods have some very attractive properties that make them good alternatives to the existing methods for diffusion-type problems and can be particularly powerful for pure convection or hyperbolic problems as those encountered in describing the thermal radiation intensity distribution in absorbing and scattering media. These properties include the high order local approximation, ease of parallelization and incorporating adaptivity strategies, element-wise conservation and geometric flexibility of conventional finite elements.

In this study, a discontinuous Galerkin finite element method for the solution of the internal radiation heat transfer problems and its integration with the continuous (or conventional) Galerkin finite element method for mixed heat transfer problems involving conduction and radiation is presented. It is noted that discontinuous finite element methods have been used for the solution of the Boltzmann integral-differential equations to study the neutron transport phenomena in nuclear engineering design systems

(Asadzadeh 1998). To my best knowledge, there appears to be very limited information on the use of the DFE method for the solution of internal radiative heat transfer problems, and its coupling with the conventional finite element method for those involving mixed heat transfer modes. More importantly, its numerical performance for radiative heat transfer in participating media and for mixed heat transfer calculations is largely unknown.

In this study, the discontinuous finite element formulation is presented for internal radiation heat transfer in participating media. The examples are given for a pure internal radiation problem and for a mixed heat transfer problem involving heat conduction, fluid flow, and internal radiation. The solutions are compared with analytical solutions whenever available. The convergence rate and adaptive algorithm in one dimensional problems for the DFE formulation are also discussed.

1.3 OBJECTIVES OF PRESENT RESEARCH

The Galerkin boundary element method to solve the external radiation exchange problems has been developed. Started with the basic concept of external radiation, an integral representation of the surface energy exchange mechanisms has been developed. The use of the Galerkin method for the solution of the integral equation is then discussed for 2-D and 3-D geometries. One of the most important parts of the algorithm development for the numerical solution of the external radiation is the accurate estimation

of kernel functions, which would require the detection of a third party blockage in complex geometric arrangements. These algorithms are very efficient schemes. Based on the algorithm for two dimensional geometries without blockage, the algorithm to detect and calculate the shadowing in two dimensional geometries is developed. After finishing the algorithm for two dimensional geometries, the algorithms are extended to three dimensional geometries. The algorithms for all two different geometries are tested under different benchmark problems, and the results of the algorithms agree very well with analytical solution or the results from literatures. The numerical solution of the mixed heat transfer problems involving conduction, convection and surface radiation exchanges is also discussed.

The internal radiative transport is the other type of radiation. A discontinuous finite element method to solve internal radiation in different dimensions is developed, and this technique has not been used by others so far. The discontinuous finite element method works very well in one-dimensional, two-dimensional, three-dimensional, and axisymmetric geometries, The nonscattering, isotropic scattering, and anisotropic scattering are also implemented by the discontinuous finite element method. Since this method is new in the radiation area, the error analysis and convergence are also discussed in one-dimensional problems. The coupling problems which involve internal radiation, heat conduction, and fluid flow are also presented.

The laser interactions with biological materials have attracted a great deal of interest in recent years, particularly for applications in biomedical treatment and diagnostics, such as optical tomography, laser surgery, photodynamic therapy, and low-power interstitial laser hyperthermia. Fundamental to these laser applications is the determination of laser transport in tissues, which influences the rate of heat generation, energy distribution of laser, heat conduction, optothermal properties, and the safety and quality of laser treatment and surgery. Based on the numerical method and algorithm we developed for internal radiation, simulation of the laser transport in the biological materials is presented.

1.4 SCOPE OF PRESENT RESEARCH

In the present study, eight major sections are discussed. Complete mathematical statement of physical phenomena in external and internal radiation problems are listed in Chapter 2. In Chapter 3, the radiation heat transfer between grey surfaces in two-dimensional geometries is discussed, and the detailed formulation derivation and results are presented. In Chapter 4, the formulations of boundary element method for three-dimensional problems are presented, and a new parallel searching and detecting algorithm for complex three-dimensional geometries are discussed. The coupling of external radiation and heat conduction and Maragoni flow is also discussed, and several computing results are presented. Chapter 5 discusses the one dimensional radiative heat

transfer problem and a new numerical simulation technique, the discontinuous finite element method is presented. In Chapter 5 the convergence and adaptive refinement techniques of the discontinuous finite element are also discussed. Chapter 6 is the extension of Chapter 5, in this section, the discontinuous finite element method for solving radiative heat transfer in absorbing, emitting, and scattering media in two-dimensional or three dimensional enclosures is discussed, and detailed formulations of the problems are also presented. The parallel computing algorithm for this problem is also discussed. In Chapter 7, the discontinuous finite element method for axisymmetric enclosure is introduced, and a new mapping of control angle algorithm is also discussed. The coupling problem of other type of heat transfer and fluid problem is also presented, and several different computing results are presented. In Chapter 8, the laser hyperthermia application in cancer treatment and the radiative heat transfer model in laser hyperthermia are introduced. The new numerical techniques we derived to solve laser hyperthermia problems is also discussed, and some simulation results are presented.

CHAPTER 2

PROBLEM STATEMENT

2.1 RADIATION HEAT EXCHANGE BETWEEN GREY SURFACES

Surface radiation exchanges play an important role in high temperature materials processing systems, for instance, the melt growth of semiconductor and oxide optical single crystals and the metals refining and remelting processes. In some of these processing systems, complex geometric arrangements that either are designed to obstruct radiation exchanges or are an integral part of an overall thermal system design. Accurate prediction of surface radiation exchange phenomena and their effects on other heat transfer modes in these systems is of vital importance to the fundamental understanding of physics that controls the processes and to the development of guidelines for optimizing the performance of the existing processes and for designing a new generation of energy efficient processing systems.

Unlike the diffusion-type problems where the field lines bend by diffusion around internal geometric obstructions, the surface exchange problems are concerned with the energy balance based on the thermal rays emitting from one surface that are intercepted by the other surface elements. Since these thermal rays travel in straight lines, an internal geometric object may block the rays from reaching other surface elements. The boundary

integral formulation for diffusion-based and the surface radiation exchange problems is similar in form. In fact, except for the difference in kernel function evaluation, the basic calculations are the same when internal geometric obstructions are absent. However, the kernel functions for surface radiation calculations can have abrupt discontinuities when the blockage of the thermal rays occurs in complex geometries. This is in sharp contrast with the boundary integral formulation for diffusion-based problems, where the kernel function is smooth and singularity may be treated analytically. Detection of these geometric obstructions can be extremely difficult and computationally intensive, despite the simple form of the kernel functions, and must be an integral part of any emerging numerical schemes for thermal radiation exchange calculations.

A detailed examination of the surface radiation problem formulations suggests that this type of calculations is well suited for parallel computation and thus the modern computer hardware architecture may be exploited to expedite the computations. Moreover, an accurate estimation of kernel functions requires a computational procedure that is capable of performing complex and tedious geometric checking. This may be facilitated by improving upon some of the best ideas (algorithms and data structures) developed over the past several decades for computer graphics applications.

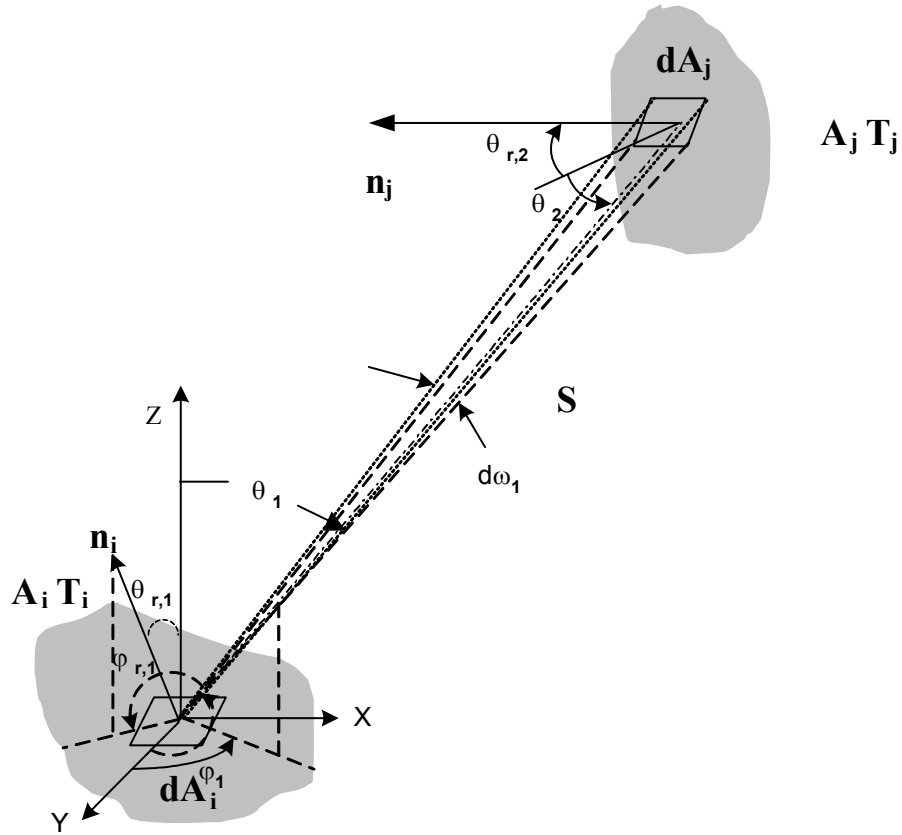


Figure 2.1

Figure 2.1 Schematic of thermal radiation exchange between two surfaces A_i and A_j .

Let us now consider the radiation exchange among surfaces that form an enclosure, as illustrated in Figure 2.1. It is assumed that there is no radiation absorbing or scattering media in the enclosure. Surface element j emits the energy to the other surfaces of the enclosure and also receives the energy from these surfaces. The heat flux $q(\mathbf{r}_j)$ is supplied to the surface element j to sustain the radiation heat transfer and is determined by the heat balance on element j involving incoming and outgoing radiation energy fluxes.

Referring to Figure 2.1, the general expression for the heat flux is given by the following integral for two-dimensional and three-dimensional geometries,

$$\begin{aligned}
q(\mathbf{r}_i) &= \int_{\lambda=0}^{\infty} \int_{\varphi_i=0}^{\varphi_i=2\pi} \int_{\theta_i=0}^{\theta_i=\pi/2} \varepsilon_{\lambda,i}(\lambda, \varphi_i, \theta_i, \mathbf{r}_i) I_{b\lambda,i}(\lambda, \mathbf{r}_i) \cos \theta_i \sin \theta_i d\theta_i d\varphi_i d\lambda \\
&\quad - \sum_{j=1}^N \int_{\lambda=0}^{\infty} \int_{A_j} \alpha_{\lambda,i}(\lambda, \varphi_i, \theta_i, \mathbf{r}_i) I_{\lambda,j}(\lambda, \varphi_j, \theta_j, \mathbf{r}_i) \frac{\cos \theta_i \cos \theta_j}{|\mathbf{r}_i - \mathbf{r}_j|^2} dA_j d\lambda
\end{aligned} \tag{2.1}$$

where the radiation intensity emitted from surface j is defined by,

$$\begin{aligned}
I_{\lambda,j}(\lambda, \varphi_{r,j}, \theta_{r,j}, \mathbf{r}_i) &= \varepsilon_{\lambda,j}(\lambda, \varphi_{r,j}, \theta_{r,j}, \mathbf{r}_i) I_{b\lambda,j}(\lambda, \mathbf{r}_i) \\
&\quad - \sum_{k=1}^N \int_{A_k} \rho_{\lambda,j}(\lambda, \varphi_{r,j}, \theta_{r,j}, \varphi_j, \theta_j, \mathbf{r}_i) I_{\lambda,k}(\lambda, \varphi_k, \theta_k, \mathbf{r}_i) \frac{\cos \theta_j \cos \theta_k}{|\mathbf{r}_k - \mathbf{r}_j|^2} dA_k
\end{aligned} \tag{2.2}$$

In the above equations, λ is the frequency, I the radiation intensity, ε the emissivity, ρ the reflectivity, θ the angle between the surface outward normal and the radiation exchange direction, and φ the azimuthal angle. Note here that subscript b refers to the blackbody radiation and thus by its definition the radiation intensity is directionally independent. Subscript r refers to the reflected radiation. Also, $\theta_{r,j}$ is the angle between the normal of surface j and the direction of the reflected radiation at surface j and $\varphi_{r,j}$ the azimuthal angle similarly defined.

While the above formulations are general, for most engineering applications the surfaces of an enclosure can be well approximated as gray, diffuse surfaces. Within the framework of these approximations, the integration over the wavelength λ can be carried

out analytically. After these analytical operations and rearranging, one has the following boundary integral formulation for the radiative heat flux $q(\mathbf{r})$ at the surface of an enclosure,

$$q(\mathbf{r}) + \varepsilon(\mathbf{r})E_b(\mathbf{r}) = \varepsilon(\mathbf{r}) \oint \left[E_b(\mathbf{r}') + \frac{1 - \varepsilon(\mathbf{r}')}{\varepsilon(\mathbf{r}')} q(\mathbf{r}') \right] K(\mathbf{r}, \mathbf{r}') d\Gamma(\mathbf{r}') \quad (2.3)$$

where E_b is the blackbody emissive power and is calculated by the integration of the blackbody radiation intensity over the entire spectrum of wavelengths,

$$E_b(\mathbf{r}) = \int_{\lambda=0}^{\infty} \int_{\varphi=0}^{\varphi=2\pi} \int_{\theta=0}^{\theta=\pi/2} I_{b\lambda}(\lambda, \mathbf{r}) \cos\theta \sin\theta d\theta d\varphi d\lambda = \sigma T^4(\mathbf{r}) \quad (2.4)$$

with σ being the Stefan-Boltzmann constant. Here use has been made of the spectral distribution of the Plank's blackbody radiation,

$$I_{b\lambda}(\lambda, T) = \frac{2hc_0^2}{\lambda^5 [\exp(hc_0/\lambda kT) - 1]} \quad (2.5)$$

where h is the Plank constant, c_0 the speed of light and k the Boltzmann constant. Notice that the subscript i on \mathbf{r}_i has been dropped out and \mathbf{r}_j replaced by \mathbf{r}' to simplify the notation. This will remain true hereafter unless indicated otherwise. Also, in the above equation, $K(\mathbf{r}, \mathbf{r}')$ is the kernel function for the integral, which takes the following form,

$$K(\mathbf{r}, \mathbf{r}') = \int_{A_i} \int_{A_j} \frac{\cos\theta_1 \cos\theta_2}{\pi \mathbf{s}(\mathbf{r}, \mathbf{r}')^2} \chi dA_1 dA_2 \quad (2.6)$$

where χ assumes a value of one when the surface element I sees the surface element J as illustrated by the ray connecting i to j , and otherwise it is zero if the ray is blocked. Thus the parameter χ is a strong function of geometric configuration and makes the kernel function highly irregular for a geometrically complex enclosure.

2.2 INTERNAL RADIATION HEAT TRANSFER

The radiative transport equation describes the distribution of the radiant intensity $I(\mathbf{r}, \mathbf{s})$, which is a function of both coordinates \mathbf{r} and direction \mathbf{s} [Modest, 1993].

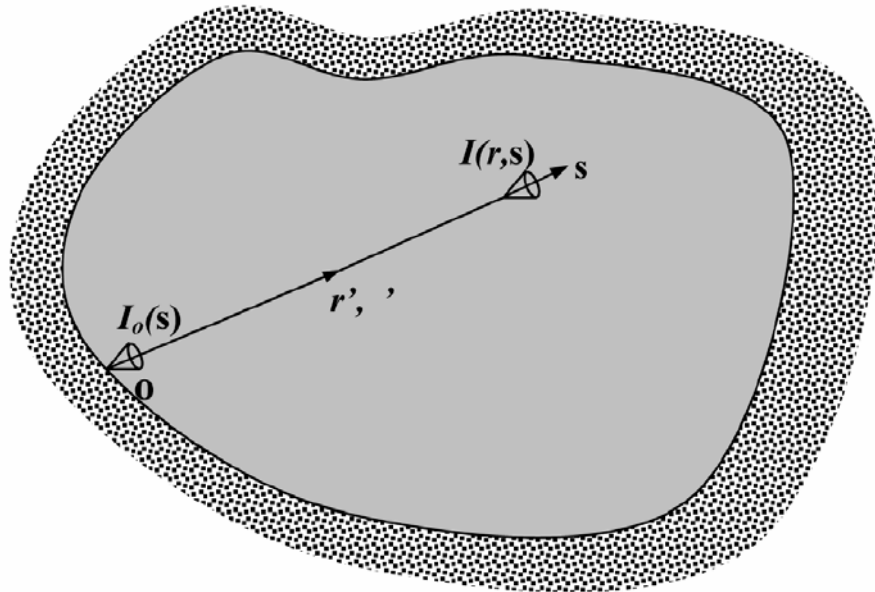


Figure 2.2. Schematic representation of internal radiation heat transfer.

The governing equation is derived based on the local balance of radiation energy, as shown in Figure 2.2. For a steady state, which is often the case for radiative heat

transfer applications, the transient effects may be neglected and we have the integral-differential equation for the distribution of radiation intensity,

$$\left\{ \begin{array}{l} \frac{\partial I(\mathbf{r}, \mathbf{s})}{\partial s} = -\beta(\mathbf{r})I(\mathbf{r}, \mathbf{s}) + \kappa(\mathbf{r})I_b(\mathbf{r}) + \frac{\sigma(\mathbf{r})}{4\pi} \int_{4\pi} I(\mathbf{r}, \mathbf{s}')\Phi(\mathbf{s}, \mathbf{s}')d\Omega' \\ \beta(\mathbf{r}) = \kappa_b(\mathbf{r}) + \sigma(\mathbf{r}) \\ \mathbf{s} = \sin \theta \cos \hat{i} + \sin \theta \sin \phi \hat{j} + \cos \theta \hat{k} \\ 0 \leq \theta < \pi, 0 \leq \phi < 2\pi \end{array} \right. \quad (2.7)$$

where $\beta(\mathbf{r})$ is the extinction coefficient, $\kappa(\mathbf{r})$ is the absorption coefficient, $\sigma(\mathbf{r})$ is the scattering coefficient, and $\Omega(\mathbf{s})$ is the solid angle associated direction \mathbf{s} , with $d\Omega = \sin \theta d\theta d\phi$ being the differential solid angle. The phase function satisfies the following condition,

$$\frac{1}{4\pi} \int_{4\pi} \Phi(\mathbf{s}, \mathbf{s}')d\Omega' = 1 \quad (2.8)$$

where \mathbf{s}' denotes the incident intensity from other directions.

The term in Eq (2.8) $\Phi(\mathbf{s}, \mathbf{s}')$ is named scattering phase function, which is used to describe scattering effects. Scattering effects are usually classified into isotropic scattering and anisotropic scattering. The former scatters energy to all other directions with the same energy distribution, whereas anisotropic scattering scatters radiation energy to different directions with various energy distributions. The isotropic scattering function is simple and easy to calculate by Eq. (2.9),

$$\Phi(\mathbf{s}, \mathbf{s}') = 1 \quad (2.9)$$

Anisotropic scattering is more complex and certainly needs more calculation time since the scattering function is direction dependent, and every direction needs to be calculated. There are two different models being used for anisotropic scattering functions, this is, forward scattering and backward scattering. The forward scattering means more energy is scattered into the forward directions than the backward directions. The backward scattering means just opposite, that is, more energy is scattered into backward direction. The scattering functions, either forward or backward, may be described by the following generic expression [Kim and Lee, 1988],

$$\Phi(s, s') = \sum_{j=1}^{N_s} c_j P_j(\cos \varpi) \quad (2.10)$$

where ϖ is calculated by

$$\varpi = \cos \theta \cos \theta' + (1 - \cos^2 \theta)(1 - \cos^2 \theta')^{1/2} \cos(\phi' - \phi) \quad (2.11)$$

and P_j is the Legend's polynomial, which can be calculated by Eq (2.12)

$$\begin{cases} p_0(x) = 1 \\ p_1(x) = x \\ p_{n+1}(x) = \frac{2n+1}{n+1} x p_n(x) - \frac{n}{n+1} p_{n-1}(x) \end{cases} \quad (2.12)$$

The RTE is solved subject to the different boundary conditions on $I(\mathbf{r}, \mathbf{s})$, which includes an opaque diffuse surface boundary condition, symmetry boundary condition, periodic boundary condition, and collimated boundary condition,

The opaque diffuse surface boundary describes the incoming intensity at \mathbf{s}' direction ($\mathbf{s}' \cdot \mathbf{n} > 0$) is reflected evenly to all directions \mathbf{s} with $\mathbf{s}' \cdot \mathbf{n} < 0$, and plus the contribution of blackbody radiation of boundary at the directions \mathbf{s} , as shown in Fig 2.3.

The opaque diffuse surface boundary condition can be expressed with the following form;

$$I(\mathbf{r}, \mathbf{s}) = \varepsilon(\mathbf{r})I_b(\mathbf{r}) + \frac{1 - \varepsilon(\mathbf{r})}{\pi} \int_{\mathbf{s}' \cdot \mathbf{n} < 0} I(\mathbf{r}, \mathbf{s}') |\mathbf{s}' \cdot \mathbf{n}| d\Omega' \quad (2.13)$$

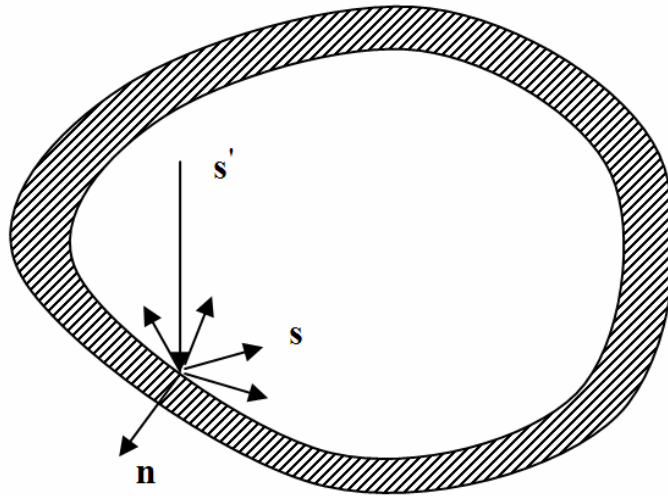


Figure 2.3. Schematic illustration for opaque diffuse boundary condition

The symmetry boundary condition is very useful in computing radiative heat transfer problems in a symmetric enclosure. By taking symmetric boundary condition, the only half of computation is needed. The systemic boundary condition is shown in Figure

2.4, in which the magnitude of intensity in \mathbf{s}^* is equal to the magnitude of intensity in \mathbf{s} . Therefore, if we obtain the value of intensity at \mathbf{s} , the computation for value of intensity at \mathbf{s}^* can be saved.

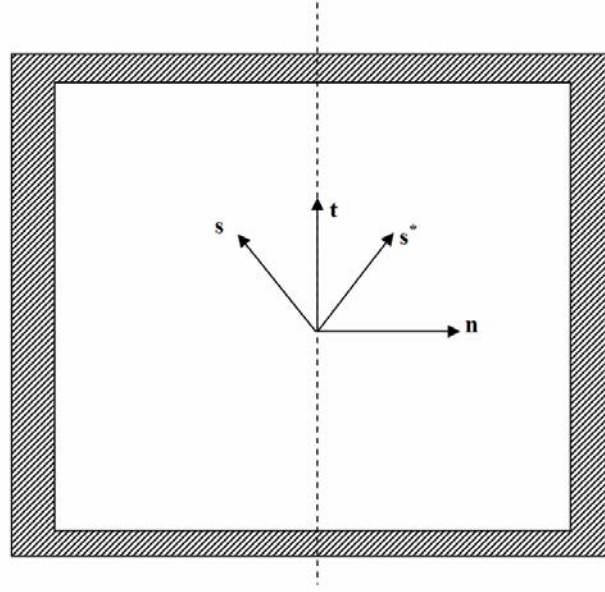


Figure 2.4 Schematic of symmetric boundary condition

The symmetric boundary condition can be described as below,

$$\begin{cases} I(\mathbf{r}, \mathbf{s}) = I(\mathbf{r}, \mathbf{s}^*) \\ \mathbf{n} \cdot \mathbf{s} = -\mathbf{n} \cdot \mathbf{s}^* \\ \mathbf{s} \times \mathbf{s}^* \cdot \mathbf{n} = 0 \end{cases} \quad (2.14)$$

where the \mathbf{s}^* is the symmetric radiation direction of \mathbf{s} respect to the tangent of the boundary, with both \mathbf{s} and \mathbf{s}^* lying on the plane of \mathbf{t} - \mathbf{n} (see Figure 2.4).

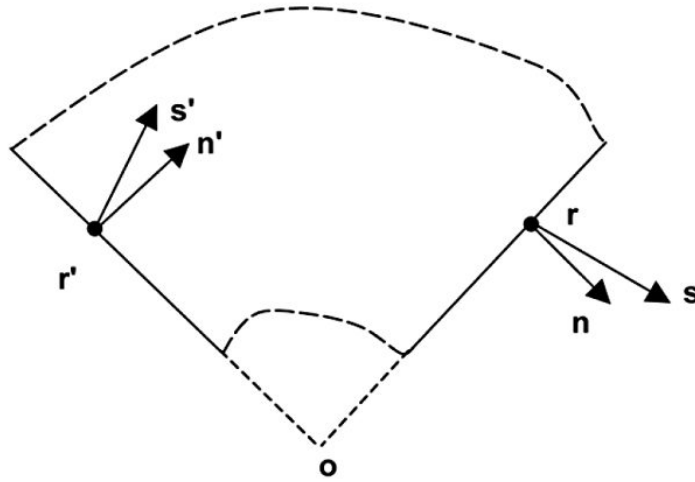


Figure 2.5 Schematic illustration of periodic boundary condition

Periodic boundary condition describes the intensity varies periodically, especially for internal radiation problems in axisymmetric enclosure. As shown in Fig. 2.5, the intensity in \mathbf{s} direction at position \mathbf{r} is equal to the intensity in \mathbf{s}' at position \mathbf{r}' , and the point \mathbf{r} can be rotated from point \mathbf{r}' around point \mathbf{o} , viz.. The symmetric boundary condition can be expressed in below,

$$\mathbf{r} = [\mathbf{R}]\mathbf{r}' \quad (2.15)$$

Where $[\mathbf{R}]$ is the rotation matrix. The normals of two boundaries \mathbf{n} and \mathbf{n}' , and the directions \mathbf{s} and \mathbf{s}' at which the intensities emit from the boundaries also have the following relations [Moder *et al.*, 2000],

$$\mathbf{n} = [\mathbf{R}]\mathbf{n}' \quad (2.16)$$

$$\mathbf{s} = [\mathbf{R}]\mathbf{s}' \quad (2.17)$$

As a result, the intensities in the directions \mathbf{s} and \mathbf{s}' are equal,

$$I(\mathbf{s}) = I(\mathbf{s}') \quad (2.18)$$

Once the distribution of radiation intensity is known, various quantities of interest to internal radiation heat transfer can be calculated. Two of the most important quantities are the heat fluxes and their derivatives, which are determined by Eqs. (2.19) and (2.20),

$$q(\mathbf{r}) \cdot \mathbf{n} = \int_{4\pi} I(\mathbf{r}, \mathbf{s}) \mathbf{s} \cdot \mathbf{n} d\Omega \quad (2.19)$$

$$\nabla \cdot q(\mathbf{r}) = \kappa(4\sigma T^4 - \int_{4\pi} I(\mathbf{r}, \mathbf{s}) d\Omega) \quad (2.20)$$

CHAPTER 3

TWO-DIMENSIONAL SIMULATION OF SURFACE RADIATION EXCHANGE BETWEEN GREY SURFACES

3.1. INTRODUCTION

The boundary integral formulation represents a natural approach to the surface radiation exchange calculations in that the energy exchange takes between the surface elements and requires the information along the surface only. The use of the boundary element method for this purpose has been explored recently by Blobner *et al.* (2001). In their studies, Blobner *et al.* has presented a *traditional* boundary element integral formulation for the thermal radiation heat transfer and coupled it with conduction for 2-D geometries. Here the word *traditional* is used in contrast with the *Galerkin* method to be discussed in this thesis. In their algorithm, as in many others, extreme caution has been exercised in treating the kernel function, which experiences abrupt discontinuity when a ray of radiation emitted from one surface to another is blocked by a geometric obstruction. In their studies, a coupled solution is also presented for a problem that involves a mixed mechanism of conduction and surface radiation. They also suggested an adaptive algorithm for an accurate integration of kernel functions for complex 2-D geometries. The adaptive algorithm, however, was not used in their examples; instead a precise

determination, based on the geometric consideration, of third party blockage is used. One critical drawback associated with the application of the traditional boundary element method for this type of calculations is that the detection of the geometric obstruction may not be exclusive in some complex geometric arrangements, thereby causing numerical errors in the calculation of the kernel function and hence the prediction of the energy exchanges. This point will be illustrated in the section below concerning the detection of third party shadowing. Nonetheless, their work has clearly demonstrated that the boundary element method can be very powerful tool for thermal radiation interchange calculations.

In this chapter, a novel algorithm for the prediction of surface radiation energy inter-exchanges between gray surfaces in two-dimensional geometries is presented. The work is motivated by the need to further improve the computational efficiency by taking advantages of updated development in both computer hardware and software algorithms. It also constitutes part of effort in developing integrated solutions to engineering problems arising from materials processing and manufacturing systems that involve multi-physics and multi-time and multi-length scale phenomena. Present approach is based on the Galerkin boundary element method, which improves upon the traditional method and allows a full detection of any geometric blockages between any two points at two surfaces involving the radiation exchange. The method is further enhanced with an efficient search and sorting algorithm developed based on the accumulated experience

with computer graphics [Zhang 2001, Honda *et al.* 2001] and suitable data structure [Bastian and Li, 2002] to increase the computational efficiency for blockage detection, which turns out to be the most CPU consuming part of the entire calculations. It is stressed here that the *Galerkin*, rather than *traditional*, boundary integral formulation, is essential to ensure that the geometric obstruction is fully detected in any complex geometries. In what follows, the Galerkin boundary integral formulation is presented, along with the design of shadowing determination algorithm, based on sorting and searching schemes used in advanced computer graphics. Examples are given to illustrate the usefulness of the method for surface energy exchange calculations. The coupling of the Galerkin boundary element method with the Galerkin finite element method for the solution of heat transfer problems involving mixed mechanisms such as conduction, convection and surface radiation is also discussed. It is thought that the algorithm described in this chapter should form a strong basis upon which valuable numerical tools can be developed to study the basic principles of surface radiation exchanges and to help engineering designs involving surface radiation heat transfer.

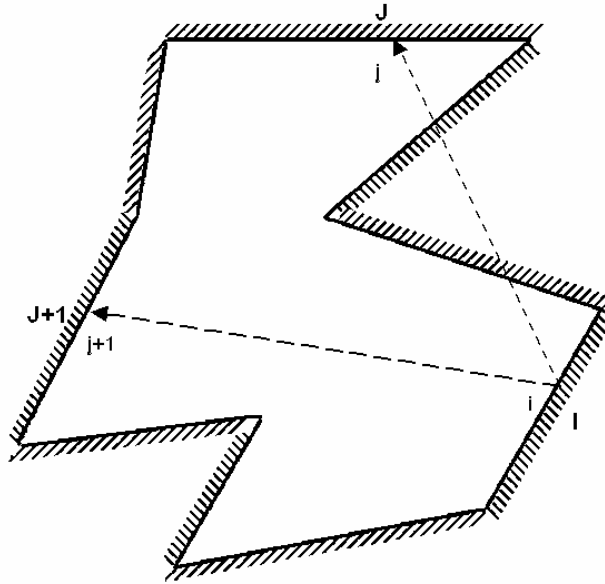


Figure 3.1: Schematic of thermal radiation exchanges: exchange among surfaces in an enclosure.

3.2. PROBLEM STATEMENT

Let us now consider the radiation exchange among surfaces that form an enclosure, as illustrated in Figure 3.1. The surface I emits the energy to other surfaces of the enclosure and meantime receives the energy from other surfaces as well. The heat flux $q(r_i)$ is supplied to the surface element I to sustain the radiation heat transfer and is determined by the heat balance on element I involving incoming and outgoing radiation energy fluxes. Referring to Figure 2.1, the general expression for the heat flux is given by the following expression,

$$\begin{aligned}
q(\mathbf{r}_i) &= \int_{\lambda=0}^{\infty} \int_{\varphi_i=0}^{\varphi_i=2\pi} \int_{\theta_i=0}^{\theta_i=\pi/2} \varepsilon'_{\lambda,i}(\lambda, \varphi_i, \theta_i, \mathbf{r}_i) I_{b\lambda,i}(\lambda, \mathbf{r}_i) \cos\theta_i \sin\theta_i d\theta_i d\varphi_i d\lambda \\
&- \sum_{j=1}^N \int_{\lambda=0}^{\infty} \int_{A_j=0} \alpha'_{\lambda,i}(\lambda, \varphi_i, \theta_i, \mathbf{r}_i) I_{\lambda,j}(\lambda, \mathbf{r}_i) \frac{\cos\phi_i \cos\phi_j}{|\mathbf{r}_i - \mathbf{r}_j|^2} dA_j d\lambda
\end{aligned} \tag{3.1}$$

where the radiation intensity emitted from surface j is given by the following expression,

$$\begin{aligned}
I_{\lambda,j}(\lambda, \varphi_{r,j}, \theta_{r,j}, \mathbf{r}_i) &= \varepsilon'_{\lambda,j}(\lambda, \varphi_{r,j}, \theta_{r,j}, \mathbf{r}_j) I_{b\lambda,j}(\lambda, \mathbf{r}_j) \\
&- \sum_{k=1}^N \int_{A_k=0} \rho'_{\lambda,j}(\lambda, \varphi_{r,j}, \theta_{r,j}, \varphi_j, \theta_j, \mathbf{r}_i) I_{\lambda,k}(\lambda, \varphi_k, \theta_k, \mathbf{r}_i) \frac{\cos\phi_i \cos\phi_k}{|\mathbf{r}_i - \mathbf{r}_k|^2} dA_k
\end{aligned} \tag{3.2}$$

In the above equations, λ is the frequency, I the radiation intensity, ε the emissivity, ρ the reflectivity, θ the angle between the surface outward normal and the radiation exchange direction, and φ the azimuthal angle. Note here that the subscript r refers the reflected radiation and the subscript b refers to blackbody radiation and thus by definition the radiation intensity is directionally independent.

While calculations using the above formulations can be performed for general conditions, for most engineering applications the surfaces of an enclosure can be well approximated as gray, diffuse surfaces. Within the framework of the approximation, the integrations over the wavelength λ and angle θ can be carried out analytically. Moreover, for a 2-D geometry, the kernel function can be further integrated analytically in the z -direction. Collecting the results from these analytical operations and rearranging,

we have the following boundary integral formulation for thermal radiation energy exchange between surfaces in an enclosure,

$$q(\mathbf{r}) + \varepsilon(\mathbf{r})E_b(\mathbf{r}) = \varepsilon(\mathbf{r}) \oint \left[E_b(\mathbf{r}') + \frac{1 - \varepsilon(\mathbf{r}')}{\varepsilon(\mathbf{r}')} q(\mathbf{r}') \right] K(\mathbf{r}, \mathbf{r}') d\Gamma(\mathbf{r}') \quad (3.3)$$

where E_b is the blackbody emissive power and is calculated by the integration of the blackbody radiation intensity over the entire spectrum of wavelengths,

$$E_b(\mathbf{r}) = \int_{\lambda=0}^{\infty} \int_{\varphi_i=0}^{\varphi_i=2\pi} \int_{\theta_i=0}^{\theta_i=\pi/2} I_{b\lambda}(\lambda, \mathbf{r}) \cos\theta \sin\theta d\theta d\varphi_i d\lambda = \sigma T^4(\mathbf{r}) \quad (3.4)$$

with σ being the Stefan-Boltzmann constant and use has been made of the spectral distribution of blackbody radiation,

$$I_{b\lambda}(\lambda, T) = \frac{2hc_o^2}{\lambda^5 [\exp(hc_o/\lambda kT) - 1]} \quad (3.5)$$

Notice that the subscript i on \mathbf{r}_i has been dropped out and \mathbf{r}_j replaced by \mathbf{r}' to simplify the notation. This will remain true hereafter until indicated otherwise. Also, in the above equation, $K(\mathbf{r}, \mathbf{r}')$ is the kernel function for the integral, which for 2-D problems takes the following form,

$$K(\mathbf{r}, \mathbf{r}') = -\frac{\mathbf{n} \cdot (\mathbf{r} - \mathbf{r}') \mathbf{n}' \cdot (\mathbf{r} - \mathbf{r}')}{2\pi |\mathbf{r} - \mathbf{r}'|^3} \chi \quad (3.6)$$

where χ assumes a value of one when the surface element I sees the surface element $J+1$ as illustrated by the ray connecting i to $j+1$, and otherwise it is zero as indicated by the ray connecting i to j , as appear in Figure 3.1. Thus the parameter χ is a strong function of geometric configuration and makes the kernel function highly irregular for a geometrically complex enclosure.

Eq. (3.3) involves the integration over the surface only and thus the boundary element method can be applied naturally to discretize the domain for a numerical solution. Following the general procedures described by Brebbia *et al.*(1984), the surface can be discretized and both E_b and q can be interpolated over each of the boundary elements by use of shape functions, i.e.,

$$q(\mathbf{r}) = \sum_{i=1}^{N_e} \psi_i q_i \quad \text{and} \quad E_b(\mathbf{r}) = \sum_{i=1}^{N_e} \psi_i E_{bi} \quad (3.7)$$

Substituting the above expressions into the boundary integral equation, one has the following equation,

$$q(\mathbf{r}_i) + \varepsilon(\mathbf{r}_i) E_b(\mathbf{r}_i) = \varepsilon(\mathbf{r}_i) \sum_{j=1}^N \int_{A_j} \left\{ \psi_1, \dots, \psi_{N_e} \right\} K(\mathbf{r}_i, \mathbf{r}') d\Gamma(\mathbf{r}') \left\{ \begin{matrix} E_{b1}^j \\ \dots \\ E_{bN_e}^j \end{matrix} \right\} + \int_{A_j} \frac{1 - \varepsilon(\mathbf{r}')}{\varepsilon(\mathbf{r}')} \left\{ \psi_1, \dots, \psi_{N_e} \right\} K(\mathbf{r}_i, \mathbf{r}') d\Gamma(\mathbf{r}') \left\{ \begin{matrix} q_1^j \\ \dots \\ q_{N_e}^j \end{matrix} \right\} \quad (3.8)$$

Here the subscript i denotes the i th global nodal point and the superscript j the j th boundary element. The subscripts $1 \dots N_e$ refer to the nodal points local to element j . Applying the above equation to every nodal point of the cavity and summing up the results, one has a final matrix form that allows the temperature (or E_b) or the heat flux q to be calculated for every nodal point.

This traditional boundary element approach should work very well if the kernel function, $K(\mathbf{r}, \mathbf{r}')$, is a smooth function, as demonstrated repeatedly in the traditional boundary integral solution of a wide range of engineering problems [Brebbia *et al.*, 1984; Song and Li, 1999]. Unfortunately, for most practical applications involving surface thermal radiation exchanges, the kernel function is not smooth and may experience abrupt disruptions or discontinuities due to various types of geometric obstructions, which can be either the third party blocking or self-blocking of the view between point i and a point of element j . Physically, an occurrence of obstruction means that the radiation intensity emitted from surface element j is intercepted by other bodies and hence does not reach point i . This geometric effect poses a serious problem for accurately calculating the kernel functions in general. Blobner *et al.* (2001) illustrated this point by use of the traditional boundary element approach for 2-D thermal radiation calculations. In their solution, care has been taken to group elements in order and to use other techniques to improve the efficiency. However, their algorithm suffers from an important drawback, which is in essence intrinsic with the traditional boundary integral

formulation. In some cases, the triangles constructed to determine the shadowing effects can potentially miss a possible third party shadowing element when it is located very close to the element associated with point i , thereby resulting in an error in their calculations.

3.3. THE GALERKIN BOUNDARY ELEMENT METHOD

Here the Galerkin boundary element method is applied to ensure a full detection of any possible blockages in an enclosure involving thermal radiation exchanges. This approach forces the global residuals to zero by use of orthogonality condition, thereby minimizing the error that possibly arises from the integral stated in Eq. (3.3). More importantly, this approach enables to be detected the shadowing elements that could be missed by the traditional boundary element method. By the Galerkin method, Eq. (3.3) is integrated once again over the entire surface with shape functions used as the weighting functions, viz.,

$$\oint_{=0} \left\{ q(\mathbf{r}) + \varepsilon(\mathbf{r})E_b(\mathbf{r}) - \varepsilon(\mathbf{r}) \oint \left[E_b(\mathbf{r}') + \frac{1 - \varepsilon(\mathbf{r}')}{\varepsilon(\mathbf{r}')} q(\mathbf{r}') \right] K(\mathbf{r}, \mathbf{r}') d\Gamma(\mathbf{r}') \right\} \psi_i d\Gamma(\mathbf{r}) \quad (3.9)$$

Now with the boundary discretized and shape functions chosen as described above, followed by some algebraic manipulations, one has the final matrix equation,

$$[\mathbf{A}]\{\mathbf{q}\} = [\mathbf{B}]\{\mathbf{E}_b\} \quad (3.10)$$

where the elements of matrices \mathbf{A} and \mathbf{B} are calculated by the following expressions,

$$A_{ij} = \int_{BE_k} \psi_i \psi_j d\Gamma(\mathbf{r}) - \int_{BE_k} \varepsilon(\mathbf{r}) \sum_{l=1}^N \int_{BE_l} \frac{1 - \varepsilon(\mathbf{r}')}{\varepsilon(\mathbf{r}')} \psi_j K(\mathbf{r}, \mathbf{r}') d\Gamma(\mathbf{r}') \psi_i d\Gamma(\mathbf{r}) \quad (3.11)$$

$$B_{ij} = - \int_{BE_k} \varepsilon(\mathbf{r}) \psi_i \psi_j d\Gamma(\mathbf{r}) + \int_{BE_k} \varepsilon(\mathbf{r}) \sum_{l=1}^N \int_{BE_l} \psi_j K(\mathbf{r}, \mathbf{r}') d\Gamma(\mathbf{r}') \psi_i d\Gamma(\mathbf{r}) \quad (3.12)$$

Depending on the boundary conditions, Eq. (3.8) can be rearranged into a standard matrix form,

$$[\mathbf{K}]\{\mathbf{u}\} = \{\mathbf{F}\} \quad (3.13)$$

where $[\mathbf{K}]$ is the global matrix, $\{\mathbf{u}\}$ the unknowns and $\{\mathbf{F}\}$ the force vector.

3.4. THE SEARCHING AND SORTING ALGORITHM

To accurately calculate the kernel function $K(\mathbf{r}, \mathbf{r}')$, it is required to determine if a radiation ray emitted from a surface element is able to reach its destination point at the other surface element, as shown in Figure 3.1. Two mechanisms can prevent a radiation ray from reaching its designated destination and must be identified in the algorithm. In the first case, the surface element does not see at all the destination point the ray is supposed to reach. This is essentially the case of self-blocking. In the second case, the

ray is blocked by a third party element due to geometric configuration, which is called the third party blocking. In both cases, the kernel function is zero. The blockage of a ray can also be differentiated into partial blocking and total blocking, which requires different treatments. Our algorithm of integrating the kernel function entails a four-step searching and sorting procedure, which has been applied effectively in 3-D computer graphics for detecting and removing of hidden lines or hidden surfaces for thermal and fluid flow data visualization (Zhang 2001, Honda *et al.*, 2001), coupled with an adaptive integration scheme, to minimize the numerical errors. The procedure is discussed below.

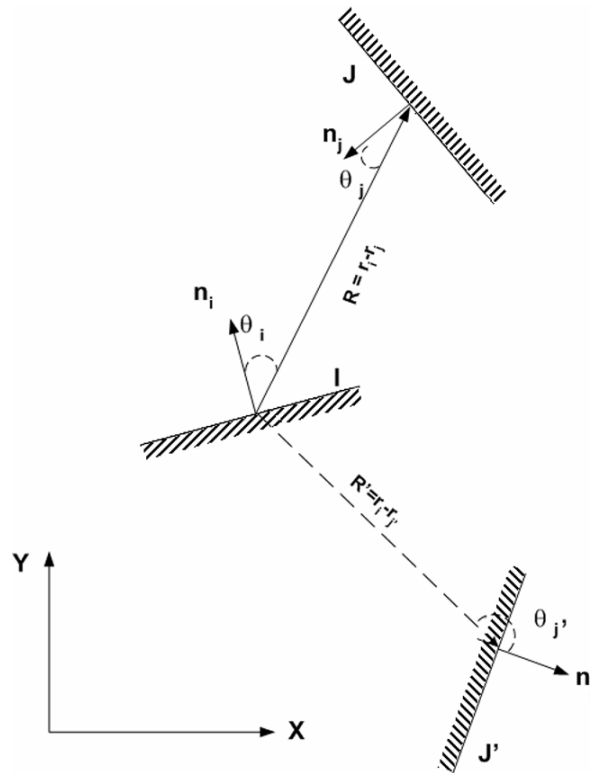


Figure 3.2: Geometric relations between mutually seen and unseen elements: radiation emitted from point i can reach point j but is unable to reach point j' because of the self-blockage by the element J' .

Before starting the search and sort procedure, a list of elements actively engaged in thermal radiation with element I from which radiation emits is created and initialized.

This list is updated as the procedure proceeds. The first step tests the signs of the product of the surface normals of the two elements (e.g. elements i and j) with the vector connecting the two elements (i.e. \mathbf{R} in Figure 3.2). This is equivalent to testing the sign of $\mathbf{n} \cdot (\mathbf{r} - \mathbf{r}') \mathbf{n}' \cdot (\mathbf{r} - \mathbf{r}')$. If the sign of $\mathbf{n} \cdot (\mathbf{r} - \mathbf{r}') \mathbf{n}' \cdot (\mathbf{r} - \mathbf{r}')$ is positive, the two elements can see each other. If $\mathbf{n} \cdot (\mathbf{r} - \mathbf{r}') \mathbf{n}' \cdot (\mathbf{r} - \mathbf{r}')$ is zero or negative, the two elements are considered not seeing each other. Based on this sign test convention, elements i and j can see each other, whereas elements i and j' can not, as shown in Figure 3.2. After this test, the elements that are unseen by element i are discarded from the list. The kernel functions for them are set to zero and no further considerations are given for them in terms of thermal radiation exchange with element I .

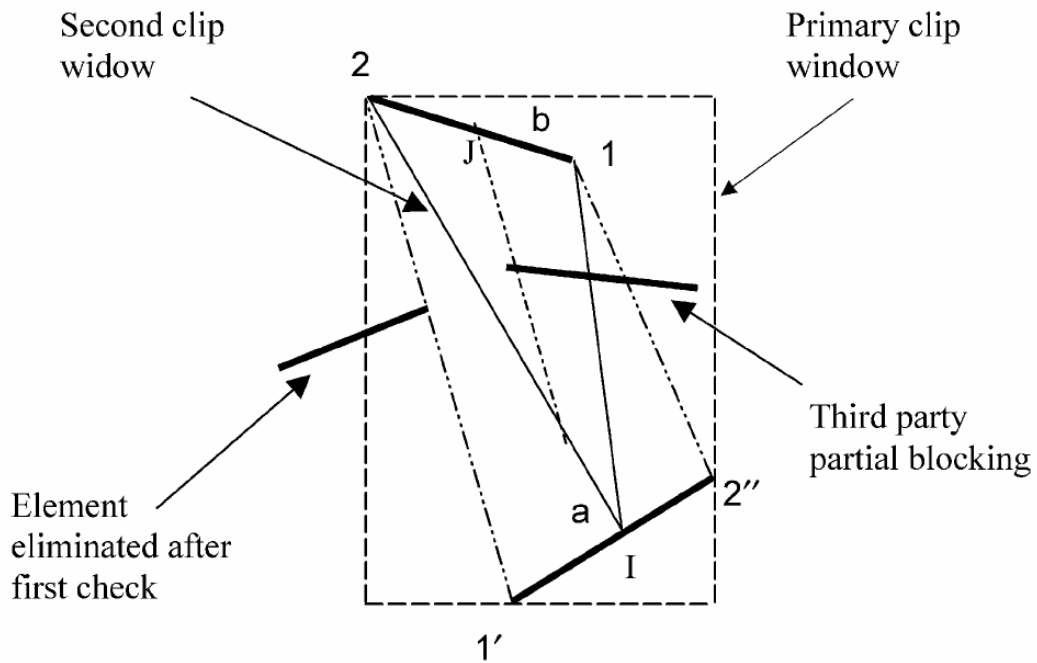
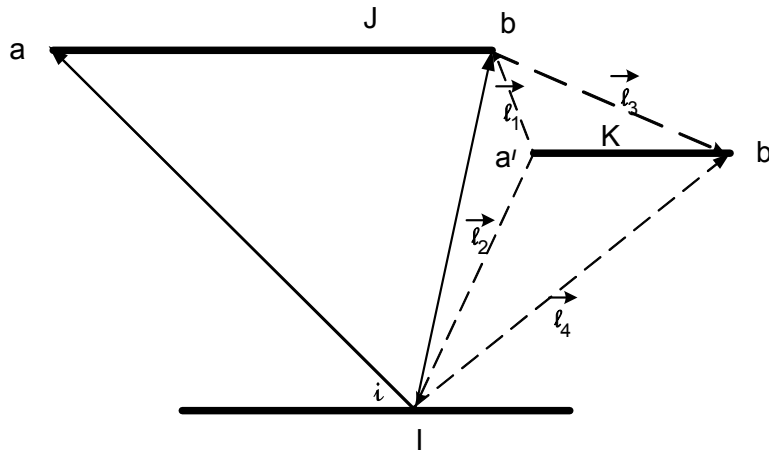


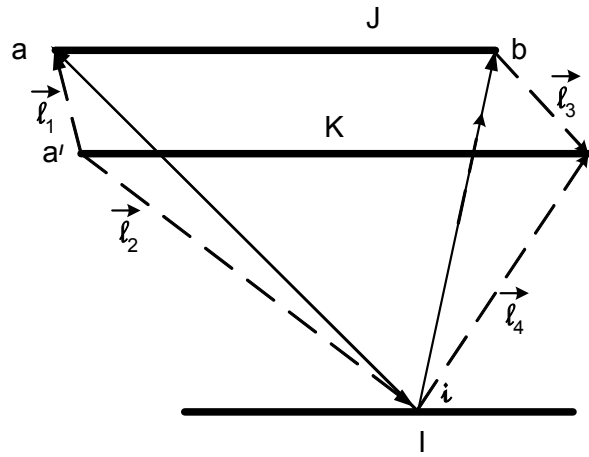
Figure 3.3: Primary and second clip windows for screening out third party shadowing elements for blocking the radiation exchange between elements I and J.

For those remaining in the list, test is conducted to determine the blockage. The procedure involves additional three steps, the basic idea of which is illustrated in Figure 3.3. Again before the test is started, another list of third party elements is created and initialized for each pair of mutually seen surface elements, determined as described in the previous paragraph. The algorithm here consists of the coarse screening and the detailed checking. First, a primary window of rectangular shape is set up using the maximum and minimum coordinates of the pair of mutually seen elements, i.e. elements I and J (see Figure 3.3). For this purpose, the standard clip algorithm routinely used in computer

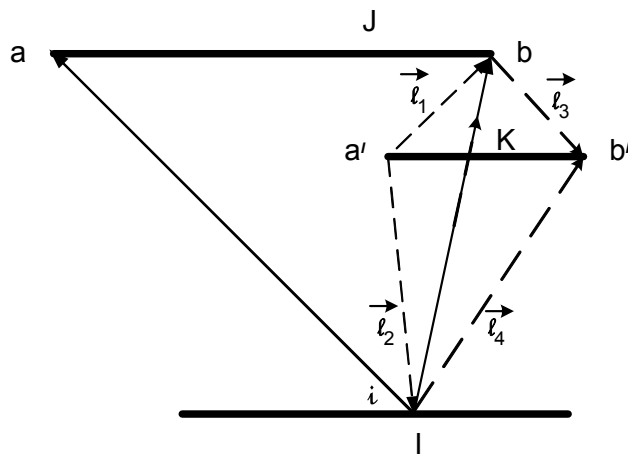
graphics for clipping objects, proved to be extremely effective, is thus directly applied (Zhang 2001). The elements lying outside the window are deleted from the list of blocking elements. This check will throw out a majority of unblocking third party shadowing elements from the list of blocking elements. Those screened through this check are further clipped out and discarded from the list of blocking elements, if they lie outside the irregular window defined by $1'2'12$. The algorithms used to clip out the elements out of the irregular window, such as $1'2'12$, are more involved and computationally intensive. However, the basic procedure is the same as for clipping against a triangle (see below), which is performed during the integration. Thus, the elements are discarded from the list if they lie outside the window $1'2'12$. And those lying partially or completely inside the window are further checked for blocking while integration is performed.



(a)



(b)



(c)

Figure 3.4. Three geometric arrangements for third party obstruction of radiation exchange between point i and element J in relation with the testing triangle: (a) no obstruction, (b) total obstruction and (c) partial obstruction.

Numerical integration is performed to compute A_{ij} and B_{ij} for each pair of mutually seen elements I and J , while checking for blockage by each remaining element in the list of partial blocking elements attached to the pair. Some of these partially

blocking elements may or may not block every ray between the two elements. To determine if a third party element actually blocks a ray between elements I and J, the third party element is first checked against a triangle formed by an integration point on element I and element J. The detailed algorithm for clipping against the triangle is given in Figure 3.4, where three different scenarios are depicted. For the case 4a, the third party element K lies outside the triangle and thus integration along element J from point i is not affected. As a result, numerical integration is carried out for element J and point i without further checking. For case 4b, the third party completely blocks a ray from point i to any points on element J. Thus, the kernel function is set to zero and no integration is carried out for element J. For case 3.4c, which is most common, the third party element is partially blocking and therefore every ray from point i to any integration point on element J needs to be further checked (see next paragraph for detail). To determine to which case the third party element K belongs, the following rule based on the geometric considerations is applied. The nodes of the triangle formed from point i and element J are numbered anti-clockwise, which allows to determine the surface normal, \mathbf{n}_s , of the triangle as positive when pointing out of the paper. Two vectors are created by connecting one point of element K, say a' (see Figure 3.4c), to two end points of one side of the triangle, e.g. $\vec{\ell}_1$ and $\vec{\ell}_2$. The cross product of the two vectors, $\vec{\ell}_2 \times \vec{\ell}_1$, is then dot with the surface normal \mathbf{n}_s of the triangle. If the dot product is positive, then the element K is inside the triangle and belongs to the category of Figure 3.4c. If both $\mathbf{n}_s \cdot \vec{\ell}_2 \times \vec{\ell}_1$

and $\mathbf{n}_s \cdot \vec{\ell}_4 \times \vec{\ell}_3$ are positive and $\vec{\ell}_i (i=1..4)$ is formed from the same side of the triangle, then the third party element K belongs to the category of Figure 3.4a. If both $\mathbf{n}_s \cdot \vec{\ell}_2 \times \vec{\ell}_1$ and $\mathbf{n}_s \cdot \vec{\ell}_4 \times \vec{\ell}_3$ are positive and $\vec{\ell}_i (i=1..4)$ is formed from two different sides of the triangle, then the element K belongs to the category of Figure 3.4b, which totally blocks the point to element J.

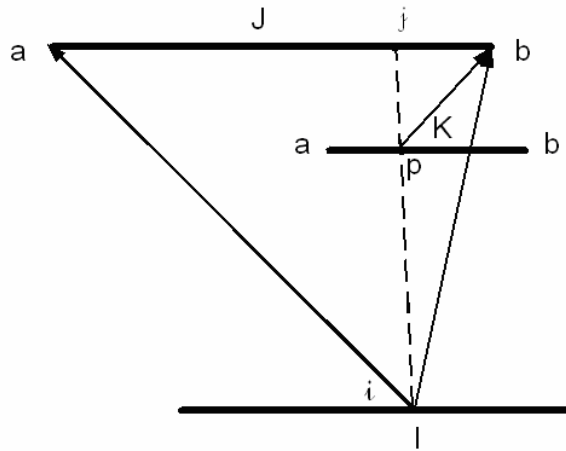


Figure 3.5: Detailed testing of blockage of radiation between points i and j by a third party element K.

For the case illustrated in Figure 3.4c, an adaptive integration algorithm is applied, while the ray connecting point i to an integration point on element J is checked for blockage as illustrated in Figure 3.5. In this case, the interception point P is calculated by simultaneously solving the two linear equations describing lines a'b' and ij. The blockage occurs if P lies on line a'b' or element K; otherwise line ij is not blocked. In applying the adaptive integration, two successive numerical integrations, with twice as

many integration points in the current step as those in the preceding one, are employed. The error between the two successive integrations is checked and the calculation is considered converged, when it is smaller than a preset value. Our experience indicates that a preset value of 0.001 as a relative error with respect to the diagonal term yields a reasonably fast convergence with sufficient accuracy.

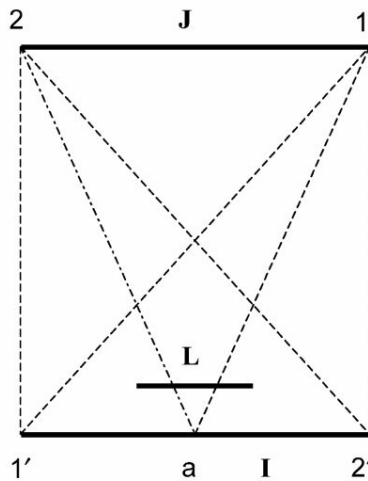


Figure 3.6. Comparison of strategies for detecting third party shadowing by the traditional and Galerkin boundary element methods. The traditional method uses the triangle formed by 1'12, where the Galerkin used triangle 1'12 and other triangles such as a12.

At this point, it may be constructive to revisit the treatment of the third party blockage when the traditional boundary element method is applied. The drawback associated with the traditional method is the possible miss in detecting the third party shadowing in some special cases. This is illustrated in Figure 3.6. Because the numerical

integration is carried out between the nodal points (1' or 2') and element J, and point a is not participated in integration (see Eq. (3.7)), the shadowing effect of element L, a third party element that actually blocks partially the view between elements I and J, is not accounted for, thereby resulting in numerical errors. The Galerkin boundary element method, however, requires the double integration of elements I and J, which in turn requires the use of internal points on either elements, and thus will be able to detect the existence of element L.

3.5. RESULTS AND DISCUSSION

The above Galerkin boundary element computational methodology, enhanced with the advanced computer graphics algorithm for sorting and searching permits the prediction of surface heat flux and temperature distributions between gray, diffuse surfaces. Computed results were obtained for a wide range of conditions. A selection of the results is presented below to illustrate the usefulness and effectiveness of the algorithm.

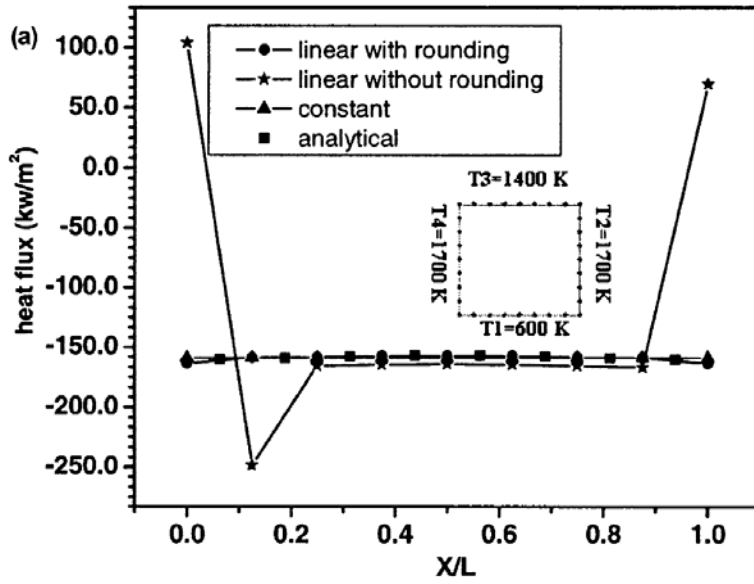
Figure 3.7 compares the heat flux distributions along the surface of a simple 2-D cavity, which are calculated using the analytical method and the Galerkin boundary element scheme using 32 constant elements or 32 linear elements. The linear boundary element mesh is also shown and the constant elements are defined such that the quantities such as heat flux and emissive powers are evaluated at the center of the element. The numerical calculations used 5 integration points, which seem to be a reasonable choice,

and result in the worst error of less than 0.001% in identity, which means all radiation leaving point \mathbf{r} must be intercepted by the enclosure surfaces,

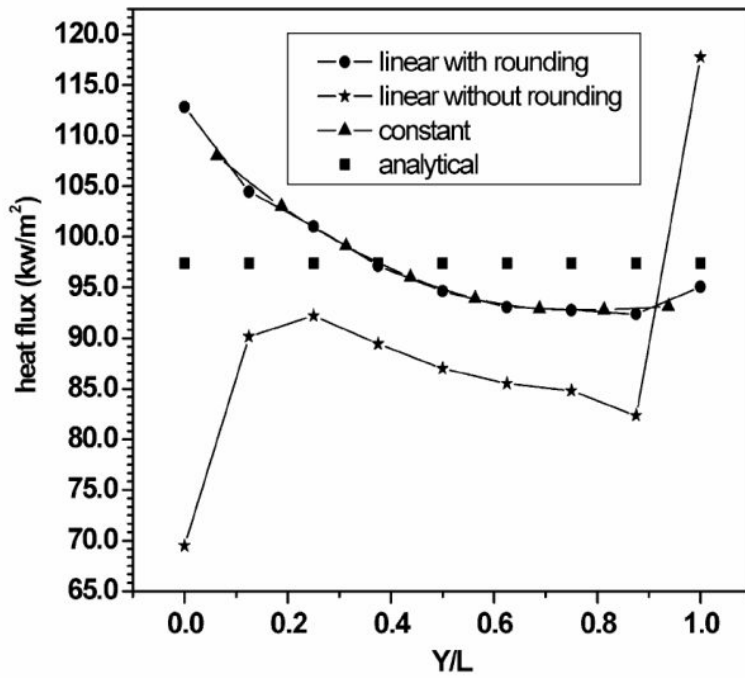
$$\oint K(\mathbf{r}, \mathbf{r}') d\Gamma(\mathbf{r}') = 1 \quad (3.14)$$

For this simple problem, one integration point gives an error about 3~5%. Larger errors occur near the corner. Inspection of these results shows that the numerical results using both types of elements are in good agreement with the analytical solutions. We note here also that the analytical solutions used the view factor and assumed a constant heat flux along one side. As such, the analytical solutions should be viewed as an approximation or a reference with which numerical solutions are compared. The further check on the overall heat balance gives a relative error of 0.02% for constant element, here the error being measured as the difference of the analytical solution and the average of the numerical heat fluxes along one wall, divided by the analytical value. The negative sign for the heat flux indicates that the heat flows into the surface or out of the square enclosure. These results are consistent with the physical processes. For instance, the fluxes are higher near edges of the bottom wall and lower at the center, which is attributed to the fact that the edges are influenced more by the side walls at higher temperatures. This is seen in the computed results by both linear and constant elements. The results from the linear elements, however, show discrepancies at the corner where

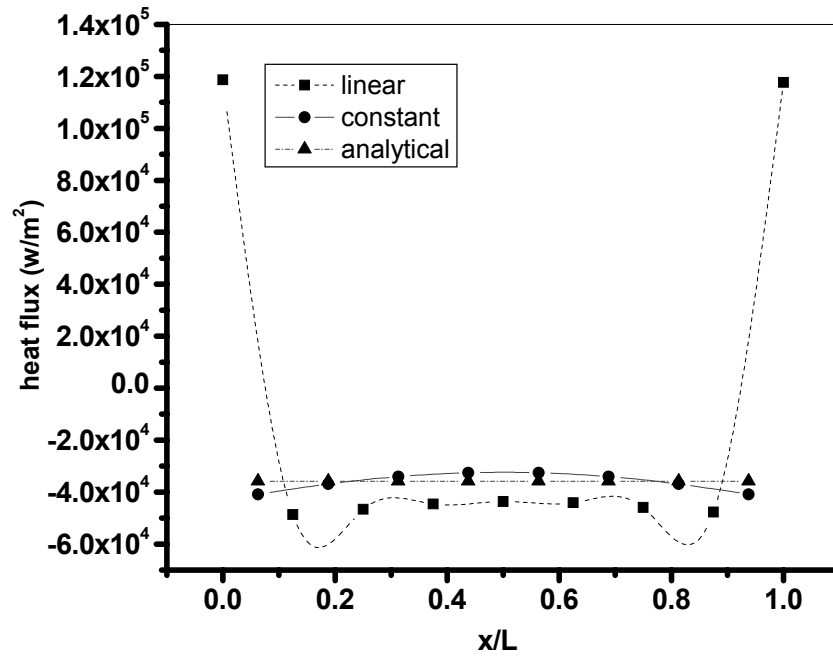
the heat flux is physically discontinuous because of an abrupt change in curvature from one side to the adjacent one. The accuracy of the linear element approximation, seen poorly at corners, can be improved, and in fact the discrepancy can be completely removed, by use of various established methods for corner treatment, such as discontinuous elements, double corner treatment and double flux treatment (Li and Song, 1999).



(a)



(b)



(c)

Figure 3.7: Boundary element mesh and comparison of numerical and analytical solutions of thermal radiation exchange in a simple 2-D geometry: (a) heat flux along bottom wall, (b) along side wall and (c) along bottom wall. Parameters used for calculations: $\varepsilon=0.5$ for all the walls, $L=3\text{m}$, and other conditions and boundary discretization are shown in the insert of figure 3.7(a).

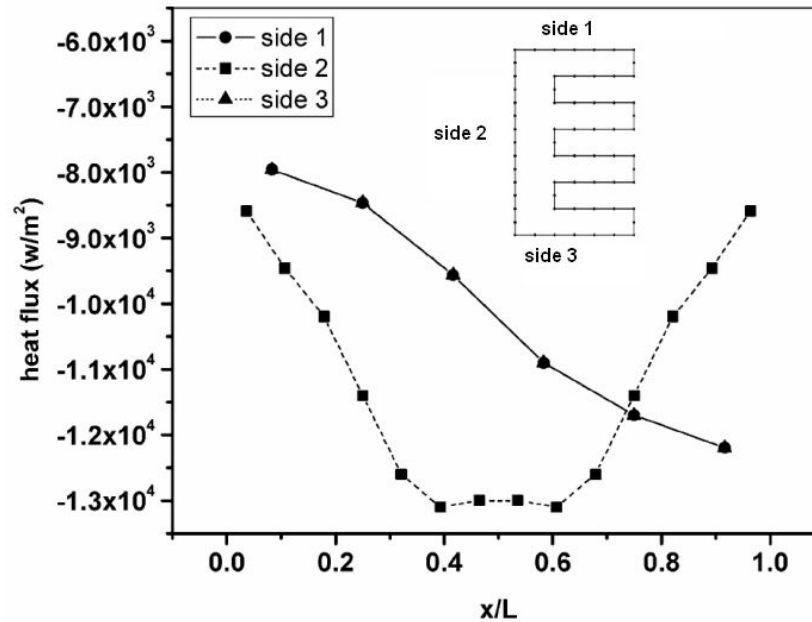


Figure 3.8. Heat flux distributions for a 2-D cavity with three protrusions that result in partial or total blocking of radiation between some surfaces of the enclosure. Parameters used for calculations: $\varepsilon = 0.5$ for all walls, $T=400$ K at, left side and bottom walls, and $T=900$ K at the rest.

The computer code was also applied to calculate the surface radiation exchange involving complex internal blockages. One of these calculations for a 2-D geometry with various blockage areas is shown in Figure 3.7, along with the boundary element meshes used for calculations. The calculations used 64 constant boundary elements and adaptive integration algorithms were invoked to treat the kernel function for the elements that are partially shadowed by the third party elements. The normalization factor is also checked for this computation and the error for is less than 0.5%. The calculated results are

consistent with thermal radiation heat transfer principles and the temperature distribution along the left side wall shows a perfect symmetric profile (Modest, 1993, Siegel and Howell, 1992).

CHAPTER 4

THREE-DIMENSIONAL SIMULATION OF SURFACE RADIATION

EXCHANGE BETWEEN GREY SURFACES

4.1 INTRODUCTION

In Chapter 3, a Galerkin boundary element method for solving surface radiation exchange between grey surfaces is discussed. This chapter presents a parallel Galerkin boundary element method for the computation of thermal radiation interchanges between surface elements in general, complex 3-D geometries and its coupling with the Galerkin finite element method for the multi-mode heat transfer calculations. The Galerkin boundary integral is derived from the direct boundary formulation of problems, and such a derivation is based on the need to ensure a full detection of geometric blockages or shadowing effects caused by configuration arrangements rather than as an alternative formulation for surface radiation problems. The computational algorithm is enhanced with a creation of appropriate data structure and with the recent development and implementation of some ideas used in hidden line removal algorithms for 3-D computer graphics applications. The parallel scheme, implemented in the UNIX/PVM environment and its performance for surface radiation calculations are discussed. To the best of our knowledge, there appears to have been very few, if any, computational procedures that

fully explore the computer-graphics based search and adaptive integration scheme for the evaluation of kernel functions with 3rd party element blockages, enhanced with parallel computing algorithm, for 3-D thermal radiation calculations. The coupling of the Galerkin boundary element calculations for surface radiation interchanges with the Galerkin finite element method for the bulk convective and conduction transfer is also given. Computational examples for complex 3-D geometries are presented.

The equations used in Chapter 3 can be extended to three-dimensional problems in this chapter. In order to save some space, the equations (3.1-3.9) in Chapter 3 will not be repeated in this chapter; instead the algorithm is presented directly.

4.2 SHADOWING ALGORITHM

Perhaps, the most important computational aspect of surface radiation exchanges is the design and implementation of a shadowing algorithm that allows an efficient and effective detection of the geometric blockage by the third parties of the thermal rays or electromagnetic waves traveling from point i on element I to point j on element J , as shown in Figure 2.1. This is also the most difficult, time consuming, and error-prone part of a computational scheme for thermal radiation exchange calculations, without which the computations are basically trivial using essentially any integration algorithms available. This can be particularly true for surface radiation exchange calculations in

complex 3-D geometries. An accurate estimation of the kernel function $K(\mathbf{r}, \mathbf{r}')$ requires determining the portion of radiation rays emitted from a surface element that is able to reach its destination point at the other surface element. Three types of blockages may be differentiated and are represented by the kernel function factor χ . The factor χ is unit if there exists no blockage between two mutually involved elements I and J. The kernel function is zero if the light ray from surface element I cannot reach any point in surface element J, or the ray is totally blocked by a third party element due to geometric configuration. In the last cases, the foreign element just blocks a portion of radiation rays between elements I and J, and the integration of the kernel function is then determined by the portion unblocked. This third case is often referred to as the partial blocking by the third party elements.

The algorithm of integrating the kernel function entails a sorting/clipping/searching procedure, which has been applied effectively in part of 3-D computer graphics for detecting and removing hidden lines or hidden surfaces for thermal and fluid flow data visualization, and an adaptive integration scheme to minimize the numerical errors. The algorithm involves four major procedures: sorting by sign, primary clipping, secondary clipping and adaptive integration with final checking. It is noted here that while the kernel evaluation can be done by integration with final checking alone for every pair of elements, this brutal force approach can be prohibitively expensive,

especially for large-scale calculations involving complex 3-D geometries. Our idea presented here is to eliminate all those elements that are not needed and to perform only on those elements that are absolutely necessary for the time intensive integration. This concept is realized by the sorting, clipping or searching and adaptive integration algorithm, along with the data structure based on the creation and updating of the element lists to optimize the computing performance, which are discussed below.

SORTING BY SIGN

Prior to the four-step procedure, a list of elements actively engaged in thermal radiation exchange with element I from which radiation emits is created and initialized. This list, labeled as the main list, may be taken as the entire set of surface elements if there exists no prior information on inter-element relations, which would be the case with $I=1$. The list initiated may be shorter starting with $I \geq 2$, because information obtained from the previous testing can be used to preclude some elements from the list to speed up the computations. For example, if elements $I=1$ and $I=2$ are not seen each other, then element 1 would not be included in the list for element $I=2$ when the list is created for $I=2$. Once it is created, the list is updated as the searching/sorting procedure proceeds. As the first step, elements are sorted by testing if two elements can see each other at all. To do that, we consider the signs of the dot product of the surface normals of the two

elements (e.g. elements I and J) with the vector connecting the two elements (i.e. \mathbf{R}_{ij} in Figure 2.1). This is equivalent to testing the sign of $\mathbf{n} \cdot (\mathbf{r} - \mathbf{r}') \mathbf{n}' \cdot (\mathbf{r} - \mathbf{r}')$. If the sign is positive, the thermal rays may reach each other between the two elements or the two elements can see each other. If $\mathbf{n} \cdot (\mathbf{r} - \mathbf{r}') \mathbf{n}' \cdot (\mathbf{r} - \mathbf{r}')$ is zero or negative, the thermal rays emitted from either element cannot reach the other element or the two elements can not see each other. Based on this sign test convention, elements I and J can't see each other (see Figure 4.1).

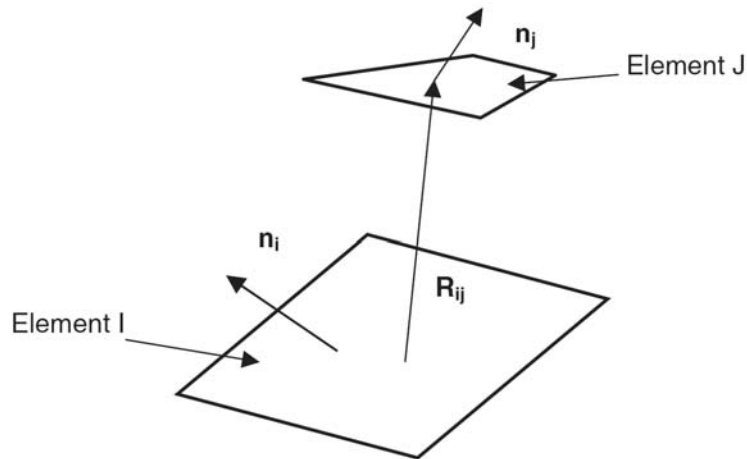


Figure 4.1 unseen surfaces

After this test, the elements that are unseen by element I are discarded from the main list. The kernel function related to them is set to zero and no further considerations are given for them in the procedures ensuing.

PRIMARY CLIPPING

The elements remaining in the main list are considered mutually seen and primary clipping is performed to determine the foreign elements for the potential third party blockage of surface radiation exchanges between an element pair of element I and one other element (say element J) selected from the main list. The basic idea of the primary clipping is illustrated in Figure 4.2. Again before the test is started, another list of third party elements, or the blocking list, is created and initialized for each pair of mutually seen surface elements in the list. This third party or blocking list is a subset of the main list excluding, but attached to, the pair of mutually seen elements, i.e. elements I and J. To begin, a primary window of brick shape is set up using the maximum and minimum coordinates of the element pair. The elements in the blocking list are checked against the primary window. For this purpose, the standard 3-D clip algorithm routinely used in computer graphics for clipping objects, proved to be extremely effective, is thus directly applied (Zhang et al., 2001). The elements lying outside the window can not possibly block the thermal rays traveling between elements I and J, and thus are deleted from the blocking list. This check will throw out a majority of unblocking third party shadowing elements from the blocking list. For example, as shown in Figure 4.2, this procedure will eliminate element L from further consideration but still keeps element K, which is considered a potential candidate for a third-part blockage. Depending on the relative geometric positions of mutual elements I and J, a good portion of elements can be

eliminated, thereby reducing the computational burden for the most tedious ray-tracing checking and adaptive integration.

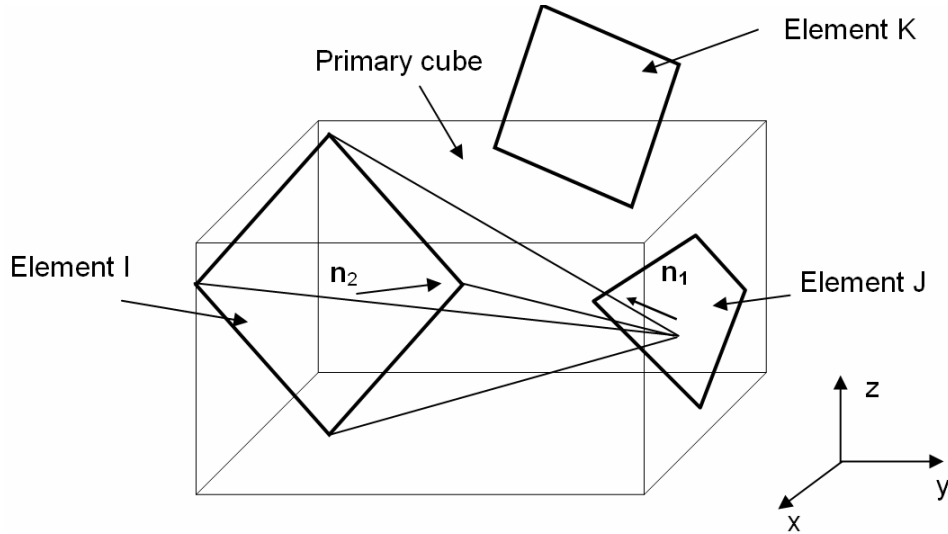


Figure 4.2 3rd blocking out of primary clipping window

SECONDARY CLIPPING

The next step involves the secondary clipping, which eliminates the elements not blocking any ray from element I to element J from the active list. This is done as follows.

A pyramid is formed by selecting a corner point, say point i , of element I and connect it to all the corners of element J. A third party element remaining or active element in the blocking list is now checked against the pyramid. The detailed algorithm for clipping against the pyramid is given in Figure 4.3, where three different scenarios are depicted.

For case 4.3(a), the third party element K lies outside the pyramid. For case 4.3(b), the third party totally blocks a ray from point i to any points on element J. For case 4.3(c),

which is the most common scenario, the third party element is partially blocking and therefore every ray from point i to any integration point on element J needs to be further checked, that is, the final checking is required during detailed integration.

To determine which of the three cases the third party element K belongs to, the following rule based on the geometric considerations is applied. A pyramid is formed by four lines, which all originate from point i , and each connect to a different vertex of element J . Each of these four lines may pass through the plane defined by element K . One of these lines, marked by $i-j$ is illustrated in Figure 4.3(c). By the similarity rules of plane triangles Δipq and Δicr , we have the following relation,

$$\mathbf{m} = (\mathbf{r}_c - \mathbf{r}_i), \quad \mathbf{r}_p = \mathbf{r}_i + \mathbf{m}t, \quad t = (\mathbf{r}_j - \mathbf{r}_i) \cdot \mathbf{n}_J / (\mathbf{r}_c - \mathbf{r}_i) \cdot \mathbf{n}_J \quad (4.1)$$

where p is the interception point of line ij with element J and \mathbf{n}_J is the outnormal of element J . Note that $pq = |(\mathbf{r}_j - \mathbf{r}_i) \cdot \mathbf{n}_J|$, which is the distance between point i and plane J . Thus, if $0 < t < 1$ or $t < 0$, then element K lies outside the pyramid, that is, either above element J or below point i . The element is then eliminated and a new check for a different element is started. The 3rd party element or element K blocks the ray from point i to element J if the following two conditions hold for any one of the four lines connecting point i to the four corners of element J ,

$$t > 1 \quad \text{and} \quad p \text{ is inside element } J.$$

To test if p is inside element J , the algorithm as illustrated in Figure 4.4 is

employed. The nodes (1,2,3,4) of element J is set up anti-clockwise, and two vectors are created by connecting the interception point p to two nodes of one side of element J, e.g., p_1 and p_2 . The cross product of the two vectors, $p_1 \times p_2$, is then dotted with the surface normal \mathbf{n}_J of element J.

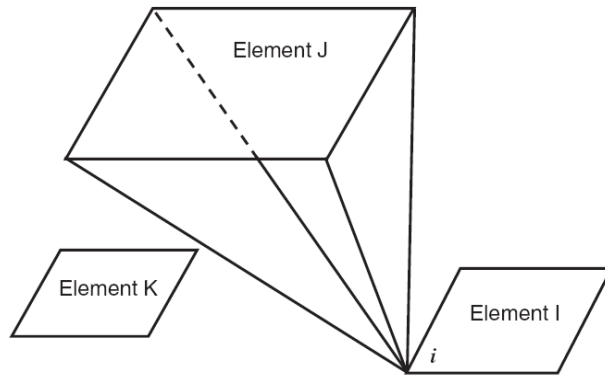
The above procedure, however, cannot surely determine cases illustrated in Figures (4.3b) and (4.3d), which show that element J may either totally or partially blocks, even if all interception points lie outside element K. Thus for all those elements whose intersection points are all outside but $0 < t < 1$, additional checking is required. This check involves calculating the intersection point k with element K by line ij . Point k can be calculated by simply exchange the corresponding points of element J with element K, or

$$\mathbf{m} = (\mathbf{r}_j - \mathbf{r}_i), \quad \mathbf{r}_k = \mathbf{r}_i + \mathbf{m}t_1, \quad t_1 = (\mathbf{r}_c - \mathbf{r}_i) \cdot \mathbf{n}_K / (\mathbf{r}_j - \mathbf{r}_i) \cdot \mathbf{n}_K \quad (4.2)$$

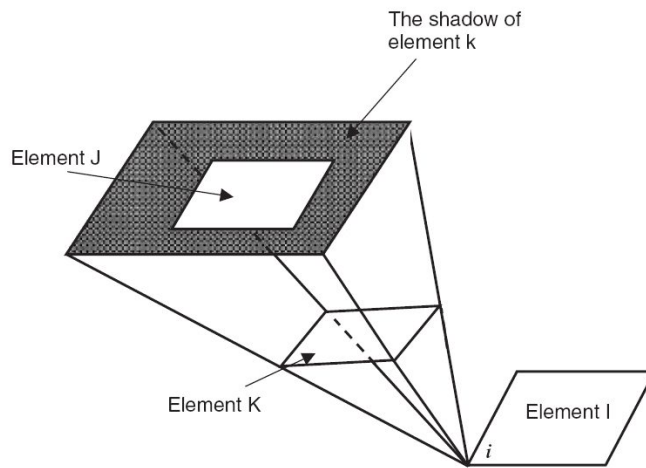
Thus, element K or blocks between the view from point i to element J, if $0 < t < 1$ and k is inside element K. Of course, the same procedure sketched in Figure 4.4 can be used to determine if k is inside element K.

It is noted that the purpose of this secondary check is to establish the active list of partial blocking elements and can be expensive since all the corners of the elements must be checked. Hence if either p or k is considered blocking during checking then element K remains in the active list for final integration and a new check is started again for another element in the rest of elements still waiting to be checked. After this secondary checking

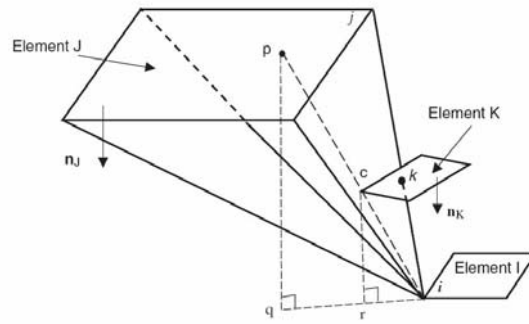
procedure, the active list contains only those elements that will most likely block the view between elements I and J. Whether or not they indeed block will be checked during final integration, which is to be described below.



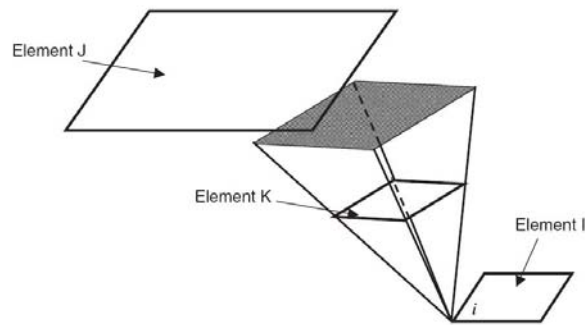
(a)



(b)



(c)



(d)

Figure 4.3. Four different scenarios of third party element blockage of thermal rays emitted from point i to element J : (a) no third part blocking; (b) total third part blocking; (c) and (d) partial third part blocking.

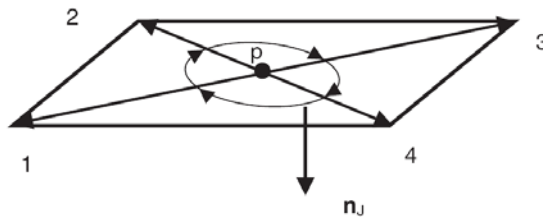
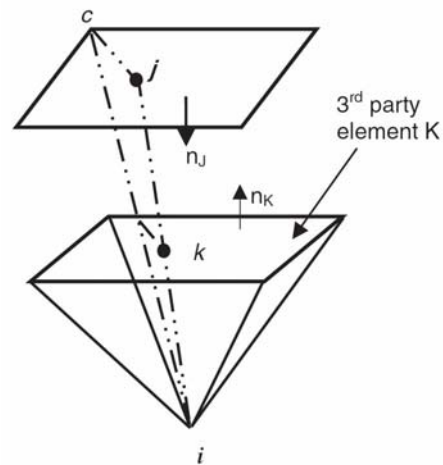


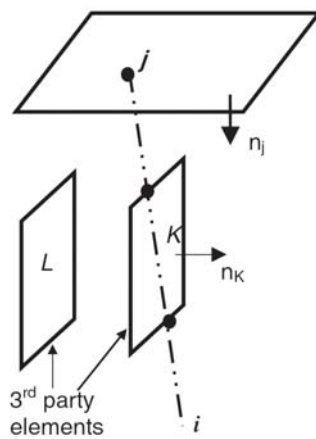
Figure 4.4. Check if P is in the plane

ADAPTIVE INTEGRATION WITH FINAL CHECK

After the secondary clipping of partial blocking elements as described above, the actual integration over elements I and J is now performed, along with the detailed final check of the third party element blockage of the thermal ray originating from an integration point on element I to another on element J (see Figure 4.5). In this study, the Gaussian integration quadrature is used. Other integration rules can also be applied. If the blocking list is empty or no active element is in the list, the integration is carried out without further checking. Otherwise, final checking of blockage is performed for those elements active in the blocking list, when integration is taken over element J. In this case, each line (or light ray emitting from integration point i on element I and ending at integration point j element J) is checked against all partially blocking elements active in the blocking list determined from the secondary clipping. If the ray connecting two integration points of respective elements I and J is blocked by the third-part element K, the value of integration is set to zero. If not this integration is calculated. The idea of determining various scenarios of the third party blocking during final numerical integration is illustrated in Figure 4.5(a). Here a line is constructed between points i and j , and the interception point k of the line with the third party element K is calculated by substituting relevant parameters into Eqs. (4.2). The interception point k is then tested using the same procedure as illustrated in Figure 4.4 to see if it lies inside element K.



(a)



(b)

Figure 4.5 Procedures used to determine the blockage of the thermal ray emitted from i to j by element K : (a) element K is not parallel $\mathbf{m} \cdot \mathbf{n}_k \neq 0$ to the thermal ray ij and k is the interception point between the thermal ray and element K ; and (b) third party elements are parallel $\mathbf{m} \cdot \mathbf{n}_k = 0$ to the thermal ray ij , and element K blocks thermal ray ij , but element L does not.

When the line ij is parallel (i. e., $\mathbf{m} \cdot \mathbf{n}_k = 0$) to the 3rd party element (see Figure 4.5(b)), Eq. (4.2) is no longer applicable. In this case, care is taken to ensure that the line passes through the element and the interception points between the plane edges and the line are calculated. If one of these interception points is between points i and j , then the 3rd party element blocks. If none of these points lie on the line between points i and j , then the 3rd party element does not block.

In order to obtain an accurate value of integration, an adaptive integration is applied. Two successive numerical integrations, with twice as many integration points in the current step as those in the preceding one, are employed in the present study. Other ways of refinement are also possible; for instance, two successive orders of numerical integration may be used instead. The error between the two successive integrations is checked and the calculation is considered converged, if the error is smaller than a preset value. Our experience indicates that a preset value of 0.001 as a relative error with respect to the diagonal term yields a reasonably fast convergence with a sufficient accuracy.

The Galerkin formulation requires surface integration over both elements I and J . This mandates that the above search and integration algorithm is carried out for integration of element J with every integration point i on element I and then integration of element I with every integration point j on element J .

The above procedure continues until the initial list associated with element I is exhausted. Then a new surface element is selected and a list of candidate elements is created. The three-step searching and integration computational process is followed. This is repeated until every surface element is calculated. The outline of the shadowing detection and adaptive integration algorithm is illustrated in Figure 4.6.

It is important to note that there are similarities between the secondary clipping and final check during integration for blockage during adaptive integration, though the latter is more involved. Thus some procedures described in the secondary clipping are applicable the final check. Additional checks as shown in Figure 4.5 are also employed in this final check stage to ensure all blockages are detected accurately. Since both procedures can be very time consuming, the secondary clipping helps to save time if the integration points per element exceed the number of corners of the element. For relatively simple geometries and relatively few elements, few integration points are needed and thus the secondary clipping may not necessarily speed up the calculations significantly.

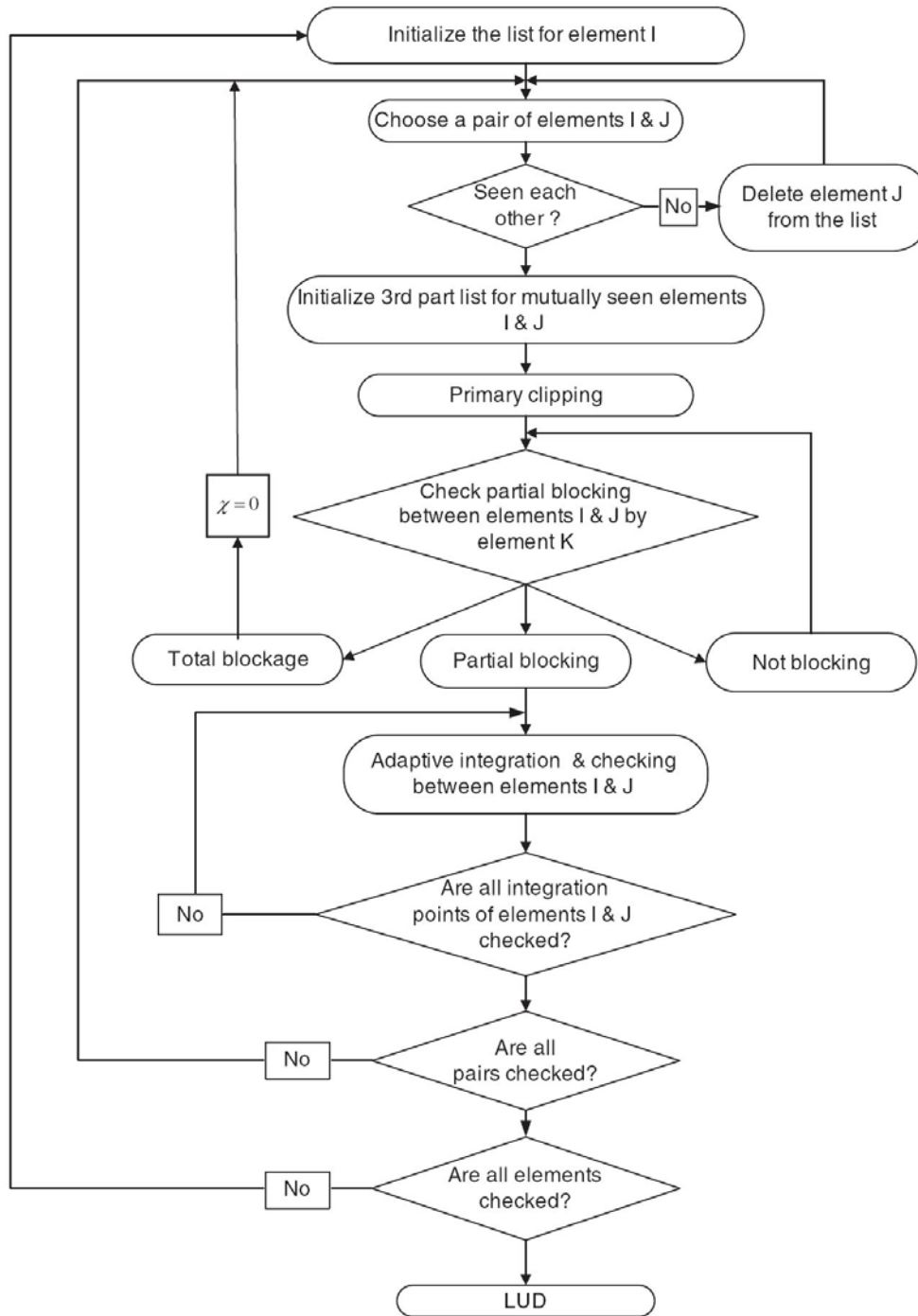


Figure 4.6 Flow chart for the searching and adaptive integration algorithm used for surface radiation calculations.

For complex geometries, partial blocking occurs very frequently and often the number of integration points needed to accurately integrate the kernel functions is significantly larger than the number of corners. For these cases, the secondary clipping provides a useful means to shorten the list to be checked during integration and thus allows savings in CPU times.

4.3 PARALLEL COMPUTING ALGORITHM AND ITS IMPLEMENTATION

The calculation of the double integral in surface radiation problem is overwhelmingly time consuming, especially for complex geometric configurations with various third party element blockages. In order to increase computational speed, a parallel computation algorithm may be used to take advantage of the modern parallel computer architectures. Indeed, careful examination of the above computational procedures indicates that the Galerkin boundary integral formulation represents perhaps an idealized scenario for parallel computing. This is because the integral between two elements is decided only by the geometric configurations associated with them. Thus the integral can be carried out independently of the similar calculations for other pairs of elements. This feature is particularly suitable for a parallel computation algorithm with the data structure based on the various lists described above, because sending and receiving information between slave processes are not required, which is a bottleneck of many parallel computation

applications.

Here we discuss some of the very basic ideas implemented in the parallel computing strategy for surface radiation exchange applications.

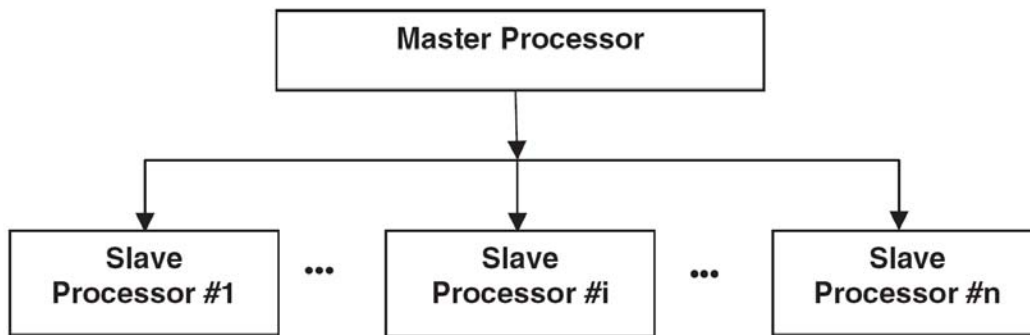


Figure 4.7 Schematic of master–slave communication in parallel processing.

Figure 4.7 shows the parallel computing algorithm incorporated into the Galerkin boundary element formulation, which is designed by following the master-slave concept common in parallel computing software development. The master processor broadcasts all data, which are required in calculating view factor between two elements, to every slave processor, and receive the results that are calculated by every slave processor by performing the actual computations for searching and integration. For a given problem, the boundary discretization yields the total number of element. Based on the number of processors available, the total number of elements is divided into subgroup of elements, as evenly as possible, so that each slave processor is loaded with the same number of element pairs for calculations. This will minimize the waiting time for any slave processors. The master then collects the results from each of the slave processors and

assembles them into global matrices **A** and **B**.

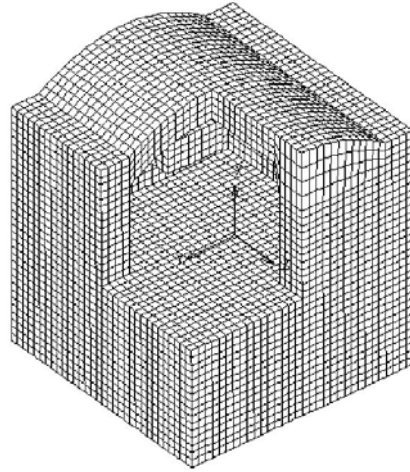


Figure 4.8 Illustration of geometry of furnace

After the data from the last slave processor are assembled, the master processor then performs the matrix inversion, say via LU decomposition, to obtain the solution to the unknowns. This is the other time consuming part of surface radiation, if the number of elements in mesh is large. This part may also be parallelized as well. Our experience shows, however, that if the number of elements is not very big, a parallel LU computation is even slower than a serial code, due to the large overhead associated with data communication between processors. The matrix inversion by itself has been an important subject of intensive research in the parallel computing community. It is thus not elaborated here. We have both in-house and commercial parallel matrix solvers that can be used for this purpose.

4.4 COUPLED WITH FE FOR MIXED MODE HEAT TRANSFER PROBLEMS

In most engineering applications, surface radiation often is not the only heat transfer mechanism, and other phenomena also coexist, such as heat conduction, fluid mechanics, melting, phase changes, etc. Thus it is required to couple the Galerkin boundary element method, with the finite element method to solve the problems involving mixed heat transfer mechanisms. We discuss the coupling procedure in the context of an example of a 3-D thermal and fluid flow system, in which the surface radiation, heat conduction and Marangoni flow are all present. Figure 4.8 shows the finite element meshes used to model the furnace. The system consists of a chamber with a cylindrical roof and a block protruded from one side into the inside of the cavity. The roof is fixed at a higher temperature and by radiation the liquid pool below is heated up. The outside of the chamber is at the room temperature and the system loses heat to the environment through radiation and conduction through the wall, which follows the Stefan-Boltzmann law. Because of the free surface of the metal is exposed to the radiation and temperature on the surface of the liquid is not uniform, the Marangoni convection and buoyancy flow arise due to the surface tension and gravity effects. The melt flow and heat transfer are governed by the Navier-Stokes equations and the energy balance equations within the solid wall, the melt and circumstance. The governing equations for the fluid flow and

heat transfer phenomena are given as follows,

$$\nabla \cdot \mathbf{u} = 0 \quad \in \Omega_1 \quad (4.3)$$

$$\rho \frac{\partial \mathbf{u}}{\partial t} + \rho \mathbf{u} \cdot \nabla \mathbf{u} = -\nabla p + \nabla \cdot \mu (\nabla \mathbf{u} + (\nabla \mathbf{u})^T) - \rho \beta \mathbf{g} (T - T_{ref}) \quad \in \Omega_1 \quad (4.4)$$

$$\rho C_p \frac{\partial T}{\partial t} + \rho C_p \mathbf{u} \cdot \nabla T = \nabla \cdot k \nabla T \quad \in \Omega_1 \quad (4.5)$$

where u is the velocity, ρ the density, T the temperature, μ the viscosity, β the thermal expansion coefficient, g the gravity, C_p the specific heat and k the thermal conductivity. The above equations, along with Eq. (3.9) describing the surface radiation exchanges in the enclosure formed by the liquid surface and the surfaces of the furnace which faces the liquid. The boundary conditions for the problem are:

$$kn \cdot \nabla T = -\delta \sigma (T^4 - T_\infty^4) \quad \in \partial \Omega_1 \quad (4.6)$$

$$\mathbf{t} \cdot \boldsymbol{\tau} \cdot \mathbf{n} = \frac{d\gamma}{dT} \mathbf{t} \cdot \nabla T \quad \in \partial \Omega_2 \quad (4.7)$$

$$\mathbf{u} \cdot \mathbf{n} = 0 \quad \in \partial \Omega_2 \quad (4.8)$$

$$T = T_H \quad \in \partial \Omega_3 \quad (4.9)$$

Where γ is surface extension, $\partial \Omega_1$ the outer surface of furnace, $\partial \Omega_2$ the top of liquid surface and $\partial \Omega_3$ the top inner surface. Note that Eq. (4.7) represents a shear stress balance along the interface, which causes a fluid motion when the surface temperature is not uniform. This type of flow is often referred to as Marangoni flow or surface tension driven flow. The finite element discretization for the solution of convection and

conduction heat transfer leads to the following matrix equations [Song and Li, 1998],

$$\begin{bmatrix} \mathbf{A}(\mathbf{U}) + \mathbf{K} + \frac{1}{\varepsilon} \mathbf{E} \mathbf{M}_p^{-1} \mathbf{E}^T & \mathbf{B}_T \\ \mathbf{D}_T(\mathbf{U}) + \mathbf{L}_T & \mathbf{0} \end{bmatrix} \begin{bmatrix} \mathbf{U} \\ \mathbf{T} \end{bmatrix} = \begin{bmatrix} \mathbf{F} \\ \mathbf{G}_T \end{bmatrix} \quad (4.10)$$

where ε is the penalty number. This matrix equation is then solved together with Eq. (3.9) to obtain information on fluid flow and temperature distribution in the system. The elements of the matrices are calculated using the following expressions,

$$\begin{aligned} \mathbf{M}_p &= \int_{\Omega} \psi \psi^T dV ; \mathbf{N}_T = \int_{\Omega} \text{Pr} \theta \theta^T dV \\ \mathbf{E}_i &= \int_{\Omega} \hat{i} \cdot \nabla \phi \psi^T dV ; \mathbf{D}_T(\mathbf{U}) = \int_{\Omega} \text{Pr} \theta \mathbf{u} \cdot \nabla \theta^T dV \\ \mathbf{L}_T &= \int_{\Omega} \nabla \theta \cdot \nabla \theta^T dV ; \mathbf{A}(\mathbf{U}) = \int_{\Omega} \phi \mathbf{u} \cdot \nabla \theta^T dV \\ \mathbf{G}_T &= -\int_{\partial\Omega} q_T \theta dS ; \mathbf{B}_T = \int_{\Omega} Gr_T (\mathbf{g} \phi \theta^T) dV \\ \mathbf{K}_{ij} &= \left(\int_{\Omega} \nabla \phi \cdot \nabla \phi^T dV \right) \delta_{ij} + \int_{\Omega} (\hat{i} \cdot \nabla \phi) (\hat{j} \cdot \nabla \phi^T) dV \end{aligned}$$

In this multi-mode heat transfer problem, the surface radiation occurs between the liquid surface and the surfaces of the furnace surrounding it. The heat transfer in the solid wall of the surface is governed by heat conduction and heat loss to the outside environment is by radiation to free space. In the liquid, non-uniform surface tension induces a Marangoni flow, which transports the thermal energy by convection in the liquid pool. The convection is combined with surface radiation and conduction to govern the overall heat balance in the liquid. The coupling of surface radiation calculations (Eq.

(3.9)) with the finite element calculations is represented by term \mathbf{G}_T . Here \mathbf{q}_T for the liquid is calculated by Eq. (3.9). In the calculations presented below, an iteration method is applied to couple the surface radiation and finite element calculations, although direct coupling is also possible. For the problem under consideration, additional speed can be gained by calculating $\mathbf{A}^{-1}\mathbf{B}$ once using the LU decomposition method and storing it in memory or on disk, due to fact that the surface properties are constant.

4.5 RESULTS AND DISCUSSION

The Galerkin boundary element methodology, coupled with the efficient searching and sorting and adaptive integration scheme, and enhanced by a master-slave parallel computational algorithm, has been applied to solve various surface radiation exchange problems encountered in thermal engineering system designs. All the computations were done on a Compaq GS80 UNIX platform, which has 8 alpha microprocessors with 8 GB Ram, capable of high performance parallel computing. A selection of the computed results is given below.

CASE 1. A CHECK WITH SIMPLE 3-D CONFIGURATION

To test the algorithm described above, calculations are first checked for a simple geometry, where the analytical solutions are readily available. The results are given in Figures 4.9, along the boundary element meshes used for calculations. To obtain the

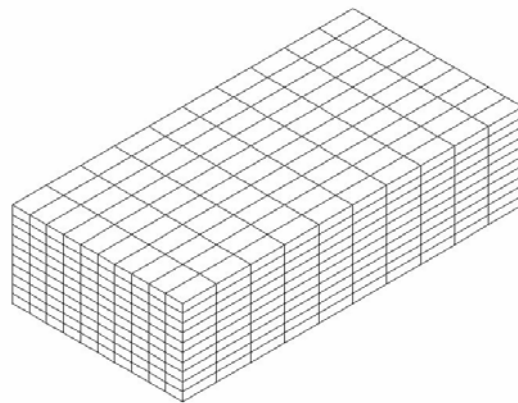
analytical solutions, a constant heat flux is prescribed along a side or a face and consequently, the analytical solution offers only a reference checkpoint. The comparisons are also further confirmed by checking the relative error on the overall heat balance for both cases as well as the identity condition,

$$\int_{\partial\Omega} K(\mathbf{r}, \mathbf{r}') d\Gamma(\mathbf{r}') = 1 \quad (4.11)$$

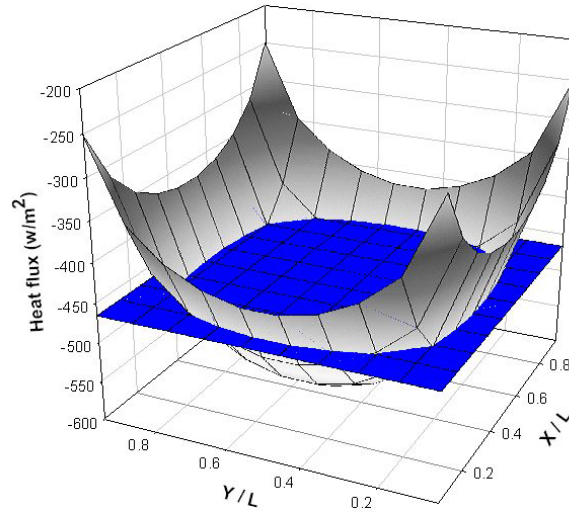
Figure 4.9 compares the heat flux distributions along the surface of a simple 3-D cavity, which is calculated using the analytical method and the Galerkin boundary element scheme. The calculations used 600 quadrilateral constant elements. Clearly, the analytical and numerical solutions are in reasonably good agreement. The numerical calculations used 5×5 integration points, which seem to be a reasonable choice, and result in the worst error of less than 0.001% in the identity condition [Minkowycz *et al.* 1999]. For this simple problem, one integration point gives an error about 3~5%. In light of the fact that the analytical solutions used the view factor and assumed a constant heat flux along one side, the analytical and numerical solutions are in reasonably good agreement. The further check on the overall heat balance, which perhaps is a more reasonable reference point, gives a relative error of 0.03%, here the error being measured as the difference of the analytical solution and the average of the numerical heat fluxes along one wall, divided by the analytical value. The negative sign for the heat flux indicates that the heat flows into the surface or out of the cavity. These results are

consistent with the physical processes in that the fluxes are higher near edges of the bottom wall and lower at the center, which is attributed to the fact that the edges are influenced more by the side walls at higher temperatures.

One of the important advantages of the Galerkin boundary element formulation is that higher order elements such as linear or quadratic elements may be selected for computations to improve the accuracy, when geometric configurations are not complex. This overcomes the limitation of the commonly used view factor formulation, which is essentially the same as the use of constant elements in the Galerkin formulation. In applying the higher order elements, caution has to be exercised ensure accuracy by account for the discontinuity of heat fluxes around a 3-D edge where an abrupt change in curvature occurs from one face to the adjacent one. It is noted that while higher order elements are possible, they are rarely used for cases where geometric configuration involves complex 3rd party blockages.



(a)



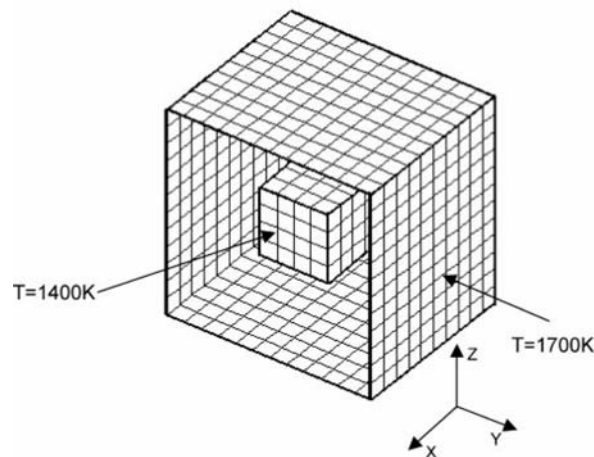
(b)

Figure 4.9 (a): Boundary element meshes. (b): calculated heat flux distribution on the top wall for a 3-D enclosure (dimensions: 2m x 1m x 0.5m). Parameters used for calculations: $\epsilon = 0.5$ and $T = 700$ K for top wall; $\epsilon = 0.5$ and $T = 300$ K for all side walls, and $\epsilon = 0.1$ and $T = 400$ K for bottom wall. The analytically calculated heat flux for the bottom wall is -466.4129 w/m^2 .

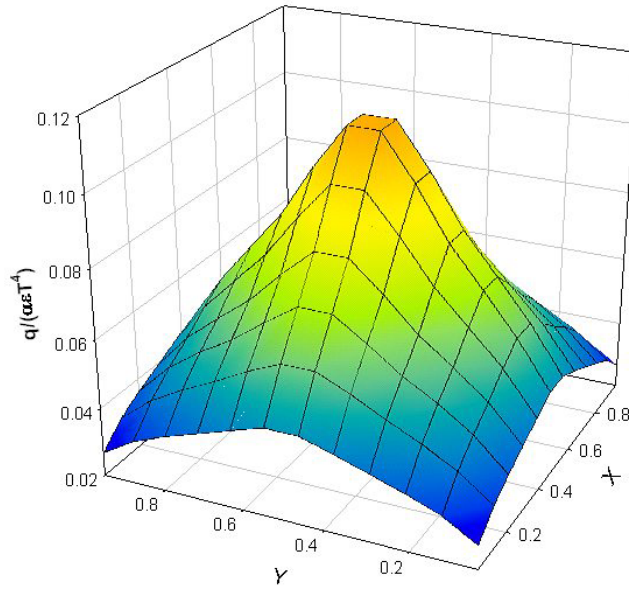
4.6 CALCULATION IN COMPLEX 3-D GEOMETRY

The computation of surface radiation exchanges in a somewhat complex 3-D enclosure, where an obstructing block is placed, is now considered. The mesh distribution used for the calculations is given in Fig. 4.10 where 1032 quadrilateral elements are used. The boundary condition is kept relatively simple such that the obstructing block is fixed at a temperature of 1400 K and the surrounding surface at 1700K. The surface emissivity of

both internal block and the enclosure is set at 0.8. It is noted that because of the symmetry associated with the geometry and boundary conditions, a quarter model may also be used to perform the calculations. Here the whole model is used for the purpose of testing the effectiveness of the methodology. The computed result of heat flux on one of the surfaces is given in Fig. 10. It is seen that the calculated heat flux shows a perfect four-fold symmetry, as expected. The heat flux is high at the center and rapidly decreases towards the 4 edges. This heat flux distribution is consistent with the heat transfer principle in that the center region of the surface is affected much more by the internal block which is at a lower temperature and the exchange of the heat flow between the surface and the block decreases as the distance between the surface and the block increases, as revealed by the kernel function.



(a)

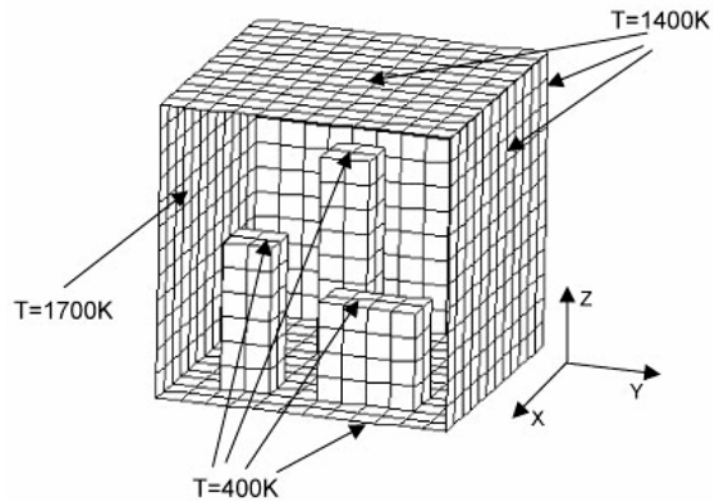


(b)

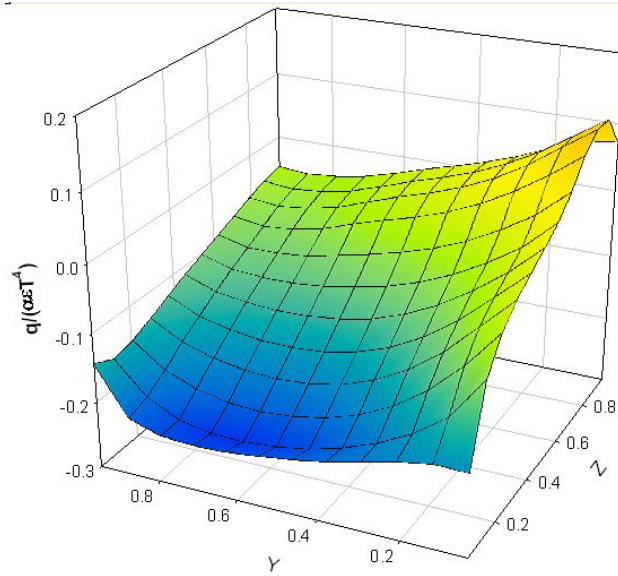
Figure 4.10 Surface radiation in an enclosure with one internal obstruction. Conditions used for calculations: the temperature of outer enclosure is at 1700 K, the inner block is at 1400 K, the emissivity of all surfaces is 0.8; the outer enclosure is $1.2 \times 1.2 \times 1.2 \text{ m}^3$, the temperature used to normalize the heat flux is 1400 K, and the inner block is $0.4 \times 0.4 \times 0.4 \text{ m}^3$ located at the centre of the enclosure. The front surface is removed for the purpose of illustration.

The next example considers the surface radiation exchange in a rather complex 3-D closure with several internal blocks of various heights. The boundary element meshes and boundary conditions used for computations are given in Figure 4.11. Note that the surface temperatures of the side surfaces of the internal obstructions are varied from 400 to 1700 K. Also, to show the inside of the enclosure, the front side, which is also

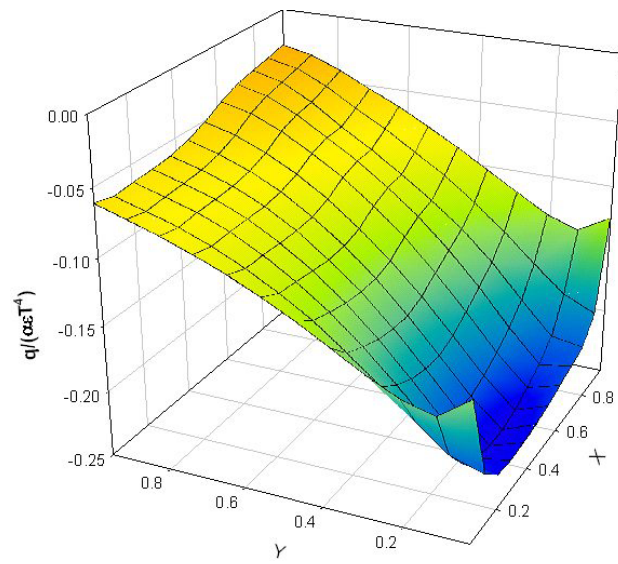
discretized using quadrilateral elements and set at 1700 K, is removed. The computed results are selectively plotted in Figs. 4.11a and 4.11b. To check the calculations, the identity condition is also calculated and the error is less than 5%. Detailed analysis shows that a major portion of the error comes from the integration between two surface elements that are very close together. The error can be reduced with further refinement of mesh sizes. It is worthy noting that in some calculations reported in the view factor calculations, a error of as high as 70% in identity condition was reported, when much less complex blockages are placed [Dupret *et al.*, 1990].



(a)



(b)



(c)

Figure 4.11. Surface radiation calculations in a complex 3-D geometry: (a) meshes and thermal conditions used for calculations; (b) heat flux on the left lateral surface of the enclosure; and (c) heat flux on the top surface of the enclosure. The dimension of the enclosure is $1.2 \times 1.2 \times 1.2 \text{ m}^3$ and the temperature used to normalize the heat flux is

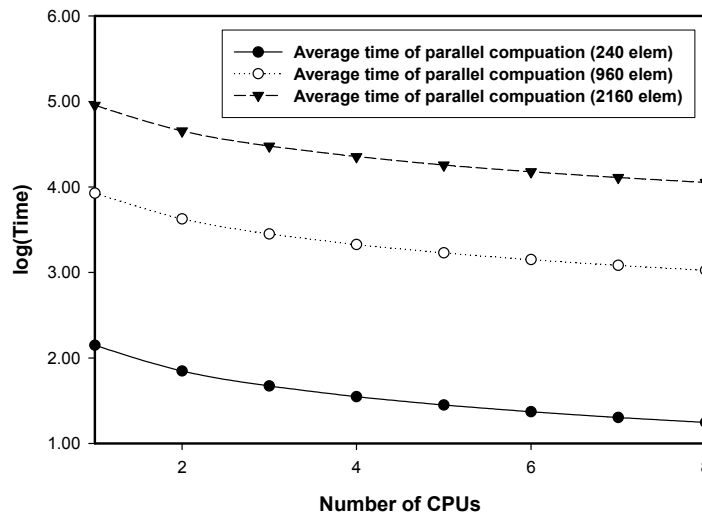
1400 K. Emissivity of all surfaces is 0.5 and side surface temperatures of the internal obstructions vary from 400 to 1700 K. The front surface is removed for the purpose of illustration.

PARALLEL COMPUTATION RESULTS

To test the parallel computing performance, the problem given in Figure 4.10 is considered. Figure 4.12(a) shows the average CPU times against the number of microprocessors used, this figure shows the effectiveness of parallel computation since the average CPU times is almost equal to T_1/n , where T_1 denotes the time being used in calculation by a single processor, and the n denotes the number of microprocessors in calculations. In other words, the more microprocessors are used, the less time is required in calculations.

The tests of this and other problems show that the sorting and clipping/searching requires an overwhelmingly major portion of CPU time. The testing result of this problem is shown in Figure 4.12(b). Clearly, any further algorithm development should be in the direction of improving efficiency of 3rd party element blockages. Examination of Figure 4.12 also indicates that the increase in the CPU time follows the relation, $T_2/T_1 \approx (n_2/n_1)^3$, where T_2 and T_1 denote the CPU times corresponding to the two different numbers of meshes, n_2 and n_1 , for the same geometric configuration. Therefore, as the

mesh doubles in size, the CPU time increases by a factor of 8.



(a)

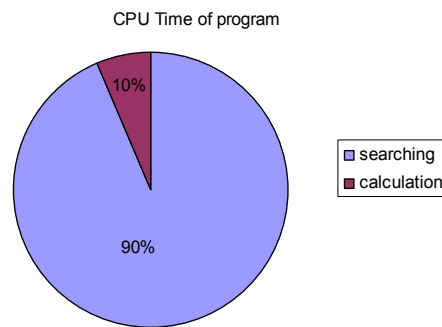


Figure 4.12. Performance of parallel computations for the 3-D surface radiation exchange problems: (a) CPU time (log time in s) vs the number of processors used with different numbers of elements; and (b) expense budget of CPU times for searching and numerical integration. The CPU times exclude those used for matrix inversion by the LU decomposition. The geometry and thermal conditions used for the computations are given in Figure 4.10(a).

MIXED HEAT TRANSFER CALCULATIONS

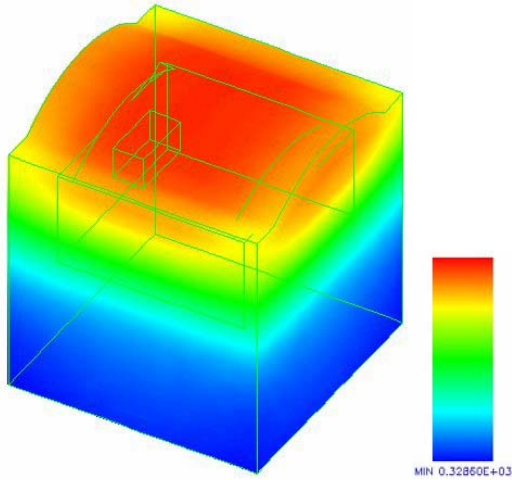
As the last example, calculations involving combined heat transfer modes are presented. The radiation algorithm described above has been successfully integrated with our in-house finite element code, which is capable of performing steady state and transient fluid flow and heat transfer calculations for both 2-D, 3-D and axisymmetry geometries. The computed results for an industrial processing system are shown in Figure 4.9, where the coupling of conduction, convection and radiation is considered. The calculations used 25,984 brick finite element elements, which are determined to be the “optimal” mesh for the simulation after grid independence check [Cui *et al.*, 2002], as shown in Fig. 4.8. There a total of 25,984 boundary elements for surface radiation calculations. Other parameters used for the calculations are given in the figure caption. The solution is obtained using the successive substitution method. Because of E_b is proportional to the fourth power of local surface temperature, a relaxation parameter of 0.1 was used to obtained converged results. For this problem, the criterion for nonlinear convergence is set such that the relative error is less than 1.0×10^{-4} .

The calculated results are plotted in Figs. 4.13a-4.13d, where the overall temperature distribution, the particle tracing and the velocity fields in a few cutting planes are given. The metal surface is heated up by the radiation from the cylindrical roof at a higher temperature. As a result, the temperature at the middle of the surface is lower

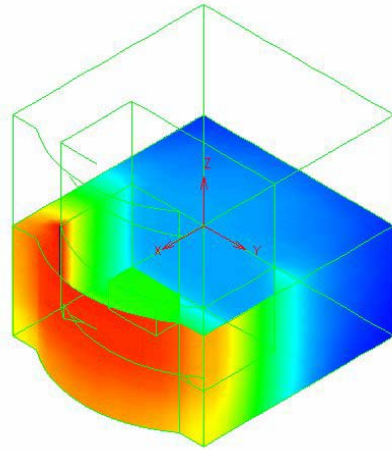
than that at the sides of the surface. This temperature field creates a surface force field such that a higher pulling force exists at the middle of the surface, which pulls the fluid particles on the surface from the side towards the center. Because of the mass conservation, a recirculating flow pattern develops, which is clearly revealed in the cutting plane representations.

In general, coupling of boundary element formulation and finite element formulation for engineering applications can be achieved either directly or iteratively. Our numerical experience indicates that the coupling may be as tedious as it gets or as easy as one would like, depending on the strategies to be implemented [Song and Li, 2001]. The direct coupling involves incorporating the boundary element matrix $\mathbf{A}^{-1}\mathbf{B}$ into the finite element global matrix by treating the entire boundary integral as one macro finite element. The implementation of this direct procedure can be very cumbersome as it requires to perturb the finite element global matrix structure [Suping and Li, 1999]. For linear problems with a moderate boundary size, this approach is favored in that the increase in the bandwidth of the global matrix is relative small and the results can be obtained directly without iteration. On the other hand, for highly nonlinear problems with a large boundary size, the direct coupling greatly increase the finite element global matrix bandwidth and the iterative solution is more effective and also easy to implement. The iteration would involve the solution of the heat fluxes from the boundary element

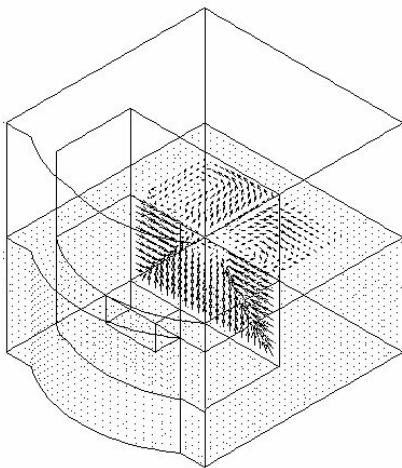
solution assuming the temperature is known along the boundary and the calculated heat fluxes are fed back into the finite element program to obtain the updated temperature fields for the next iteration. For cases falling in between, experience is key to obtain faster solutions.



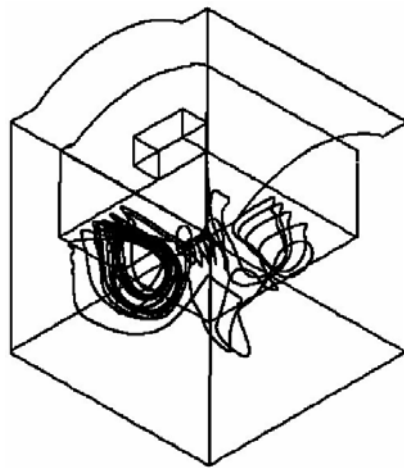
(a)



(b)



(c)



(d)

Figure 4.13. Calculated results of mixed mode heat transfer in an industrial furnace using the coupled Galerkin boundary/finite element method: (a) temperature distribution in the furnace; (b) body-cut view of temperature distribution; (c) body-cut view of velocity distribution in the liquid pool—maximum velocity is 1.9 mm/s; and (d) particle trajectory plot. Parameters for calculations: liquid pool is $0.15 \times 0.3 \times 0.3 \text{ m}^3$ and filled with Ga melt. The top surface temperature is 340 K and the environment is at 295 K. The emissivity of all surface is 0.5 and the thermal conductivity and specific heat of the furnace walls are 10 W/m K and 130 kJ/kg K, respectively. The gravity is in the opposite x-direction (see Figure 4.9).

4.6. CONCLUDING REMARKS

This chapter has presented a parallel Galerkin boundary element method for the solution of surface radiation exchange problems and its coupling with the finite element method for mixed mode heat transfer computations in general 3-D geometries. The computational algorithm is enhanced with the implementation of ideas used in hidden line removal algorithms for 3-D computer graphics applications and with data structures involving creating and updating various element lists optimized for performance. The shadowing detection scheme design entails a four-step procedure involving sorting by sign, primary clipping, secondary clipping and adaptive integration with final check, which has

substantially curtailed the time required for the evaluation of kernel functions in complex 3-D geometries. The computational efficiency is further improved by implementing a parallel scheme based on the master-slave concept. Examples from both simple and complex 3-D geometric configurations have been presented. Numerical experiments show that a majority of computational time is spent on the detection of foreign element blockages and parallel computing is ideally suited for surface radiation calculations. The decrease of the CPU time approaches asymptotically to the inverse rule, that is, inversely proportional to the number of microprocessors used. For large scale computations involving complex 3-D geometries, an iterative procedure is preferred for the coupling of Galerkin boundary and finite elements for mixed mode heat transfer calculations.

CHAPTER 5

ONE-DIMENSIONAL RADIATIVE HEAT TRANSFER IN PARTICIPATING MEDIA

5.1 INTRODUCTION

Internal thermal radiation describes the energy transport in an intervening medium that directly affects the radiation transfer via mechanisms of absorption, emission and scattering. Some of the engineering thermal systems in which thermal radiation plays a crucial role include the growth of optical single crystals from high temperature applications in industry. Owing to the importance of internal radiation transfer in thermal engineering applications, many numerical techniques have been developed to predict the phenomena and to assist in thermal designs involving radiative heat transfer. In this chapter, a new numerical technique is introduced to solving radiative heat transfer in participating media problems.

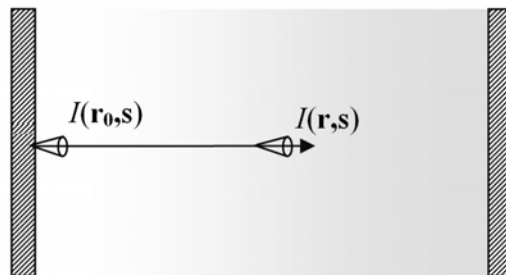


Figure 5.1 Schematic illustration of one-dimensional radiative heat transfer problems

Discontinuous Galerkin finite element (DFE hereafter) methods, also called discontinuous Galerkin methods, have undergone rapid development recently and become increasingly popular in the numerical computational community. A comprehensive review of the history, development and current trends of discontinuous finite elements has been presented by Cockburn, et al. (2000). The DFE methods have some very attractive properties that make them good alternatives to the existing methods for diffusion-type problems and particularly powerful for problems of pure convection or hyperbolic problems such as those encountered in describing the thermal radiation intensity distributions in absorbing and scattering media. These properties include the high order local approximation, ease of parallelization and incorporating adaptivity strategies, elementwise conservation and geometric flexibility of conventional finite elements.

This chapter presents a discontinuous Galerkin finite element method for the solution of the internal radiation heat transfer problems in one-dimensional geometries, and its integration with the continuous (or conventional) Galerkin finite element method for mixed heat transfer problems involving conduction and radiation. It is noted that discontinuous finite element methods have been used for the solution of the Boltzmann integral-differential equations to study the neutron transport phenomena in nuclear engineering design systems [Asadzadeh, 1998]. To our best knowledge, there appears to

have very limited information on the use of the DFE method for the solution of internal radiative heat transfer problems, and its coupling with the conventional finite element method for those involving mixed heat transfer modes. More importantly, its numerical performance for radiative heat transfer in participating media and for mixed heat transfer calculations is largely unknown.

In what follows, the basic ideas for discontinuous finite element method are discussed for a simple linear hyperbolic (or pure convection) problem. The application of this method to internal radiation heat transfer is then given, along with the examples for a pure internal radiation problem and for a mixed heat transfer problem involving both heat conduction and internal radiation. The solutions are compared with analytical solutions whenever available. The convergence rate and adaptive algorithm are also discussed.

5.2 DISCONTINUOUS FINITE ELEMENT FORMULATION

The discontinuous Galerkin finite element formulation of a boundary value problem follows a very similar procedure to that used for the conventional Galerkin finite element treatment. It starts with the Weighted Residuals integration, followed by the use of the Galerkin interpolation for the weighted functions. The essential difference between the conventional and the discontinuous finite element formulations lies in the treatment of the inter-element boundary conditions. In the former, the inter-element variables such as

fluxes and field variables are strongly enforced. This enforcement requires the use of interpolations functions from the complete finite element space, although non-confirming elements that passing patch tests are also possible for certain applications. In the latter, however, the field variables and their fluxes are only weakly imposed or a jump in these quantities is assumed to across the inter-element boundaries. As a result, the interpolation functions need to be selected from the finite element broken space [Oden *et al.* 1998]. It has been demonstrated that the discontinuous finite element formulation is particularly powerful for the convection-dominated problems where the solutions develop sharp fronts and also for the hyperbolic type of problems [Cockburn *et al.*, 2000].

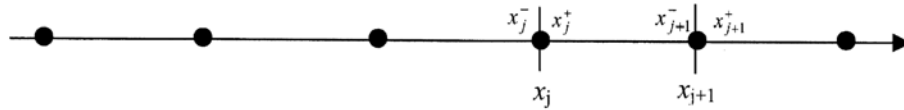


Figure 5.2. Discretization of 1-D domain with jump conditions across the inter-element boundaries

In this chapter, a discontinuous finite element formulation for a 1-D radiative transfer problem is developed. To start, the domain is discretized into a collection of finite elements (see Figure 5.2), as done for the conventional finite element applications. Unlike for the other applications where the solid angle integration is treated using the discrete ordinates, here the solid angle treatment is also performed with the framework of

the discontinuous finite elements so that the conservation laws are observed. Let us take the element defined by $\Delta x_j [x_j, x_{j+1}]$, Eq. (2.7) in Chapter 2 is integrated with respect to a weighting function $v(\Omega, x)$,

$$\int_{\Delta\Omega_l} \int_{\Delta x_j} v \frac{\partial I}{\partial s} dx d\Omega = \int_{\Delta x_j} \int_{\Delta\Omega_l} v (-\beta(\mathbf{r})I(\mathbf{r}, \mathbf{s}) + S(\mathbf{r}, \mathbf{s})) d\Omega dx \quad (5.1)$$

where $\mathbf{r} = x\hat{i}$ and $S(\mathbf{r}, \mathbf{s})$ is the source function defined as

$$S(\mathbf{r}, \mathbf{s}) = \kappa_b(\mathbf{r})I_b(\mathbf{r}) + \frac{\sigma(\mathbf{r})}{4\pi} \int_{4\pi} I(\mathbf{r}, \mathbf{s}') \Phi(\mathbf{s}, \mathbf{s}') d\Omega' \quad (5.2)$$

Eq. (5.1) is now integrated by parts with the result,

$$\int_{\Delta\Omega_l} \left(\int_{\Delta x_j} -I \frac{\partial v}{\partial s} dx + vI \mathbf{n} \cdot \mathbf{s}|_{j+1} + vI \mathbf{n} \cdot \mathbf{s}|_j \right) d\Omega = \int_{\Delta x_j} \int_{\Delta\Omega_l} v (-\beta(\mathbf{r})I(\mathbf{r}, \mathbf{s}) + S(\mathbf{r}, \mathbf{s})) d\Omega dx \quad (5.3)$$

where \mathbf{n} is the outnormal and the use has been made of Green's formula,

$$\mathbf{s} \cdot \int_A \phi \mathbf{n} dA - \mathbf{s} \cdot \int_{\Delta V} \nabla \phi dV = \mathbf{s} \cdot \int_{\Delta V} \phi \nabla I dV \quad (5.4)$$

to convert the domain integral into the boundary integral. Note that \mathbf{s} is the unit vector of the direction of radiation intensity $I(\mathbf{r}, \mathbf{s})$ and is independent of the volume. In the conventional finite element formulation, the terms on the boundary disappear when they combine with neighboring elements. In the discontinuous formulation, however, these

terms do not go away when elements are assembled. Instead, the following limiting values are used (see Figure 5.2),

$$I_j^+ = \lim_{x^+ \rightarrow x_j} I(x) \quad \text{and} \quad I_j^- = \lim_{x^- \rightarrow x_j} I(x)$$

If the elements are now assembled, the boundary terms will experience jumps across the element boundaries and these jumps are often denoted by,

$$[I]_j = I_j^+ - I_j^-$$

These jumps may also be modeled by the generic numerical fluxes that are single valued at the boundaries and are a function of field values across the inter-element boundaries. For the problems under consideration, the simplest and effective choice is to use the upwinding value, which in the discontinuous finite element literature is some times referred to as inflow boundary value,

$$[I]_j = \begin{cases} I_j^- & \text{if } \mathbf{n} \cdot \mathbf{s} < 0 \\ I_j^+ & \text{if } \mathbf{n} \cdot \mathbf{s} > 0 \end{cases} \quad (5.5)$$

We may now use appropriate interpolation functions, which are chosen from the finite element broken space that requires no continuity across the inter-element boundaries. A natural choice for the internal radiation applications is to take the delta function for the solid angle and a polynomial function for spatial variation,

$v(\Omega, x) = d(\Omega_l)\phi$. Substituting this testing function into the integral expression, one has the following expression,

$$\int_{\Delta x_j} I(\mathbf{r}, \mathbf{s}_l) \mathbf{s}_l \cdot \nabla \phi dx + [I_j] \mathbf{n} \cdot \mathbf{s}_l + [I_{j+1}] \mathbf{n} \cdot \mathbf{s}_l = \int_{\Delta x_j} \phi(-\beta(\mathbf{r})I(\mathbf{r}, \mathbf{s}_l) + S(\mathbf{r}, \mathbf{s}_l)) dx \quad (5.6)$$

Following the standard procedures for element calculations, we obtain the matrix equation for each element,

$$[K]\{I\} = \{f\} \quad (5.7)$$

where the matrices are calculated by the following expressions,

$$k_{ij} = \int_{\Delta z_m} \phi_i \frac{\partial \phi_j}{\partial z} e_z \cdot s_l dz + \beta \int_{\Delta z_m} \phi_i \phi_j dz + \delta_{ij} \max(0, e_z \cdot s_l) - \delta_{ij} \max(0, -e_z \cdot s_l) \quad (5.8)$$

$$f_i = \kappa \int_{\Delta z_m} \phi_i S(z) dz + n_z \cdot s_l I_{1,l}^- + \max(0, e_z \cdot s_l) I_{m,l}^- - \max(0, -e_z \cdot s_l) I_{m,l}^+ \quad (5.9)$$

Note that for simplicity we assume the medium is not scattering and for a scattering medium, additional source term $S(\mathbf{r}, \mathbf{s}_l)$ needs to be considered, which is straightforward.

The calculation starts with a selected direction and those associated with a boundary element, where the boundary condition is imposed as follows,

$$I^-(\mathbf{r}, \mathbf{s}_l) = \varepsilon(\mathbf{r}) I_b(\mathbf{r}) + \frac{1 - \varepsilon(\mathbf{r})}{\pi} \sum_{j=0, \mathbf{s}_j' \cdot \mathbf{n} < 0}^{N_\theta} I^+(\mathbf{r}, \mathbf{s}_j') |\mathbf{s}_j' \cdot \mathbf{n}| \Delta \Omega_j' \quad (5.10)$$

It continues element by element until the entire domain and all directions are covered. Because of the boundary conditions, iterative procedures are required. The successive substitution method seems to work well for this problem.

Before the numerical results are presented, a few points may deserve a discussion. First, if the jump condition is set to zero in Eq. (5.3), which means that the inter-element continuity is enforced, we have the conventional finite element formulation. Second, if the zeroth order polynomial is chosen as the spatial interpolation function, then we have the common finite difference (or volume) formulation [Chai and Partankar, 2000]. Thus, in this sense, the finite volume method is a subclass of the discontinuous finite element method, and uses the lowest order approximation to the field variables.

5.3. COUPLING OF CONVENTIONAL AND DISCONTINUOUS FINITE ELEMENTS

The conventional finite element formulations have been well established for the solution of a wide range of heat transfer problems such as heat conduction and convection. Thus, it is natural to test the idea of coupling the conventional and discontinuous finite element formulations for the mixed heat transfer calculations that involve internal radiation and conduction/convection. To illustrate the idea of this coupled approach, we again consider a 1-D mixed heat transfer problem that involves both conduction and internal radiation in

a gray medium. The differential heat balance equation governing the conduction and radiation may be readily written out,

$$\rho c_p \frac{\partial T}{\partial t} = \nabla \cdot (k \nabla T - q_r) + q''' \quad (5.11)$$

with the term $\nabla \cdot \mathbf{q}_r$ calculated using the radiative transfer equation as described above.

The coupling entails the use of the conventional method for heat conduction and the discontinuous method for the internal radiation calculations. Since the radiation heat flux contribution appears as a divergence term in the source part of the heat balance equation, it opens up two possibilities of coupling the discontinuous and conventional finite elements for the mixed heat transfer calculations. Depending on which approach is taken, the radiative heat flux on the boundary may or may not be needed explicitly. The two coupling approaches are described below.

In the first approach, the heat balance equation is formulated following the same procedure as used in conventional finite element method. This will lead to a global matrix equation with the nodal temperatures as the unknowns. To incorporate the internal radiation effect, $\nabla \cdot \mathbf{q}_r$ is calculated over a finite element where the internal radiation takes place and then coupled to the global matrix equation as a source term. This represents a simple and direct approach. In this way, the boundary condition on $\mathbf{n} \cdot \mathbf{q}_c$ is required, which of course must satisfy the total heat flux balance along the boundary [Lan et al., 2003].

In the second approach, which is often taken by many researchers using the finite volume formulations for temperature calculations, the term $\nabla \cdot \mathbf{q}_r$ is integrated out and $\mathbf{n} \cdot \mathbf{q}_r$ at the element boundaries are used. If this approach is taken for the conventional and discontinuous finite element coupling, then one would have the following expression embedded in the conventional finite element formulation for the heat balance equation,

$$\int_{\Omega_i} \nabla \cdot \mathbf{q}_r \phi dV = \oint_{\partial\Omega_i} \mathbf{q}_r \cdot \mathbf{n} \phi dS - \int_{\Omega_i} \nabla \phi \cdot \mathbf{q}_r dV \quad (5.12)$$

Thus, this approach requires the information on \mathbf{q}_r in the interior of a element and along the domain boundaries. By this approach, a specification of total heat flux ($\mathbf{n} \cdot \mathbf{q}_r$ and $\mathbf{n} \cdot \mathbf{q}_c$) at the boundary term is required, which is more convenient for different phases [Chan et al., 1983]. It is remarked here that $\nabla \cdot \mathbf{q}_r$ is not calculated using a numerical differentiation of \mathbf{q}_r and thus there is no loss in numerical accuracy if $\nabla \cdot \mathbf{q}_r$ is used. It is noted also that if the shape function ϕ chosen as a delta function, the volume term on the right hand side vanishes and the formulation reduces to the popular finite volume formulation.

By either of the approaches, the combined heat conduction and radiation calculations require iterative procedures. In a typical iteration process, the temperature distribution is calculated using the conventional finite elements while the internal radiation intensities are by the discontinuous finite elements. The iteration starts with the

calculation of temperature without radiative heat transfer. The solution of the intensity distribution and hence the divergence of heat fluxes are then calculated using the temperature information. The radiation heat flux divergence is then treated as a heating source and the temperature distribution is updated. This process repeats itself until a convergence on temperature is obtained.

As a last note, we stress that the discontinuous finite element method may be directly used to solve the heat conduction problem in place of the conventional finite element method. This can be done by first splitting the second order heat conduction equation into two first order differential equations with T and \mathbf{q} as independent variables and then following the above DFE procedure to solve T and \mathbf{q} simultaneously. In doing so, however, appropriate numerical fluxes must be designed; otherwise the discretized equation will not satisfy the consistency condition, that is, the discretized equation will not converge to the differential equation as the mesh size reduces to zero. Numerical studies further show that while this splitting procedure is possible and indeed gives satisfactory results when correct numerical fluxes are used, it is ineffective in comparison with the conventional finite element method for the heat conduction or elliptical problems, because it requires solving more unknowns (T and \mathbf{q}) [Hughes *et al.*, 2000]. Thus for the mixed heat transfer calculations, a coupled approach involving the conventional and discontinuous finite elements appears to be a better choice than the

use of either of the two methods alone.

5.4. RESULTS AND DISCUSSION

In this section, the discontinuous finite element algorithm and the coupled conventional and discontinuous algorithm discussed above are applied to solve internal radiation problems and mixed heat transfer problems. Here, only one-D problems are considered and whenever possible the numerical results will be compared with the available analytical solutions. Also, the convergence rate of the discontinuous finite element method and the implementation of the local mesh adaptivity for the numerical solution of radiative transfer problems are discussed. The gray participating media are used for all the cases presented below.

Internal Radiation Problem

The problem is schematically illustrated in Figure 5.3, where the thermal radiation takes place in a gray slab filled with an absorbing and scattering medium. Figure 5.4 shows the distribution of radiation intensity along its traveling path from the bottom to the top, obtained from analytical solutions [Modest, 1993; Siegel and Howell, 1992], by the discontinuous Galerkin finite element method described above, and by the popular two-flux model [Koenigsdorff *et al.*, 1991]. The analytical solutions for the problem are relatively straightforward and for convenience of comparison they are reproduced here

[Modest, 1993],

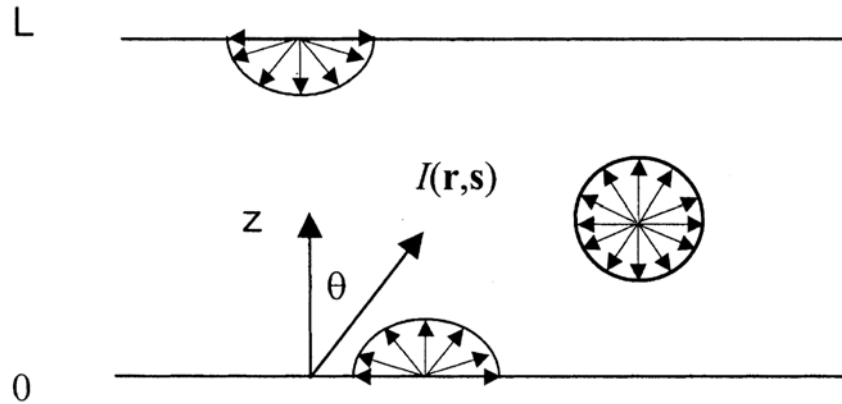


Figure 5.3 Thermal radiation in a slab filled with an absorbing and scattering medium.

$$\begin{aligned}
 I^+(\tau, \mu) &= I_1(\mu)e^{-\tau/\mu} + \int_0^\tau S(\tau', \mu)e^{-(\tau-\tau')/\mu} \frac{d\tau'}{d\mu}, & 0 < \mu < 1 \\
 I^-(\tau, \mu) &= I_2(\mu)e^{(\tau_L-\tau)/\mu} + \int_\tau^{\tau_L} S(\tau', \mu)e^{(\tau'-\tau)/\mu} \frac{d\tau'}{d\mu}, & -1 < \mu < 0
 \end{aligned}
 \tag{5.13}$$

where I^+ and I^- refer to the intensity associated with $u > 0$ and $u < 0$, respectively. τ is the optical thickness, $\tau_L = \beta L$ and $u = \cos \theta$.

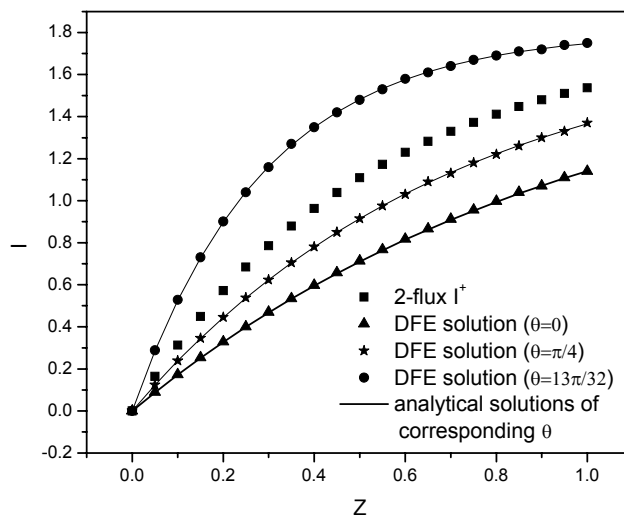
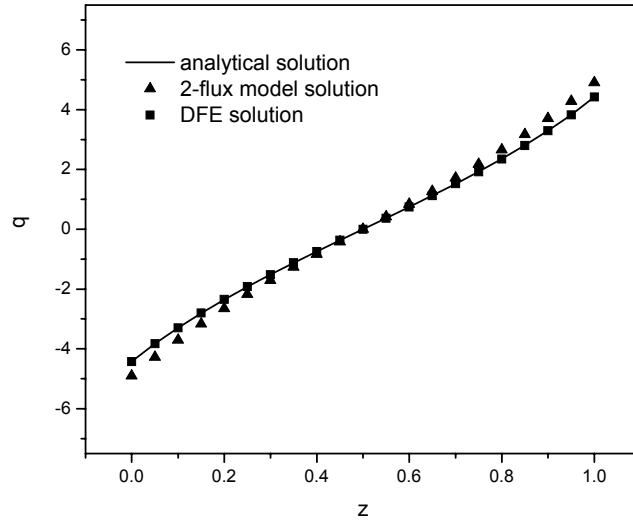
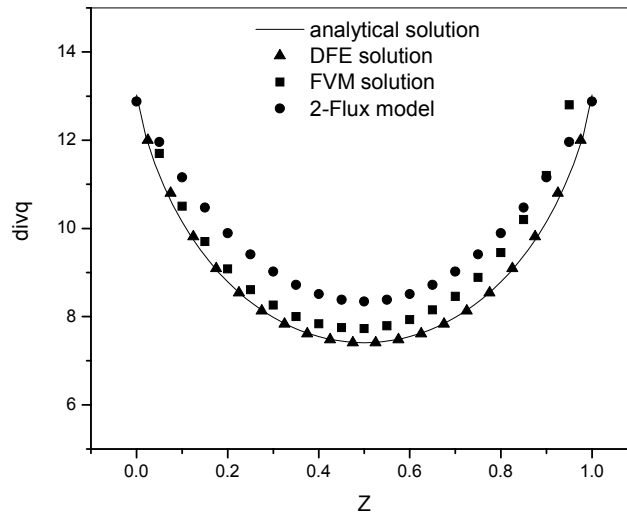


Figure 5.4. Radiation intensity distributions calculated by analytical solutions, two flux model, and the discontinuous finite element method with linear and constant elements. Parameters used for calculations: two 1-D plates, $T_2=T_1=0$ K, the emissivity of the plates=1.0, $\kappa=1.0$, $\sigma=0$. The temperature of media is 100 K.

In most of the internal radiation calculations reported so far, the results of the heat flux were considered only, because of its interest to heat balance. Our calculations indicated that the intensity offers a better comparison in terms of numerical accuracy, because the intensity is the directly calculated result. For the results shown in Figure 5.4, the numerical solution used 20 linear elements and scattering coefficient is set to zero for simplicity. Clearly, excellent agreement exists between the numerical and analytical solutions, suggesting that the discontinuous finite element method is useful for this type of problems. It is noted, however, that the two-flux model gives an averaged value in the half sphere, and thus it lies in between the intensities at different directions. The computed results for the distribution of heat fluxes and heat flux divergence obtained from the two-flux model and DFE are also plotted in Figure 5.5, along with the analytical solutions, which were calculated using Eqs. (2.19), and (5.13). Examination of these results illustrates that the DFE results with linear elements match well with the analytical solutions and are more accurate than either the two-flux model [Koenigsdorff *et al.*, 1991] or those by constant elements denoted by FVM.



(a)



(b)

Figure 5.5. (a) Computed results for the distributions of heat fluxes and (b) divergence of radiative heat fluxes ($\text{div}q$). The parameters used for calculations are the same as in

Figure 5.4.

Convergence Rate and Consistency

Consistency and convergence rate are two important issues for a numerical algorithm. The former ensures that a discretized equation converges to the governing differential equation as the mesh size reduces to zero, while the later is concerned about the rate at which this convergence takes place and is also useful for the design of mesh adaptive algorithms. For the error analyses, the L_2 -norm is often used to measure the error, e.g., the difference between the exact solution u and DFE solution u_h . With this measure, the analysis of the discontinuous finite element formulation shows that the convergence of numerical solution to the exact solution is expressed by [Johnson, 1987],

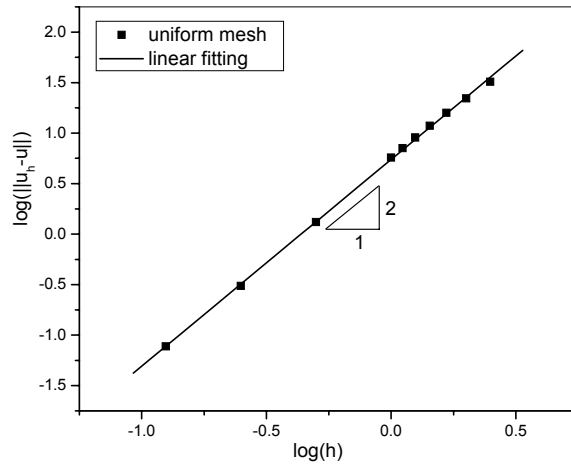
$$\|u_h - u\|_0 \leq Ch^n \|u\|_{n+1} \quad (5.14)$$

where h is the size of the maximum element, and for a 1-D problem, h is the length of largest element. In literature, Eq. (5.14) is also referred to as the *a priori* error estimate. In Eq. (5.14), n is the order of convergence rate, which takes a value of one for a non-uniform mesh and 2 for a nearly uniform mesh [Lin, 2000]. $\|\cdot\|_m$ denotes the m^{th} order norms [Oden and Carey, 1983],

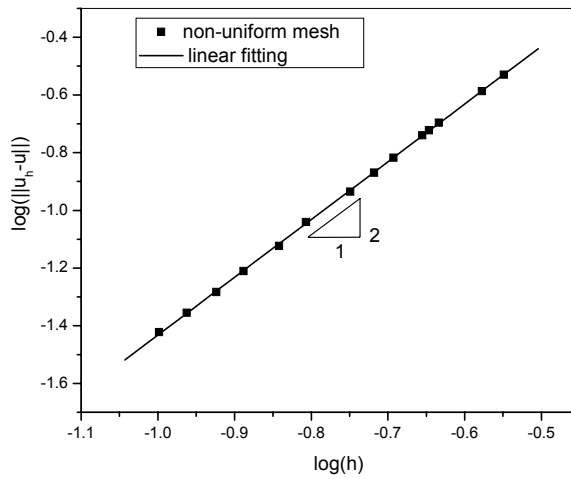
$$\|u_h - u\|_m = \left[\int_{\Omega} \left((u_h - u)^2 + (u'_h - u')^2 + \dots + (u^{(m)}_h - u^{(m)})^2 \right) dx \right]^{1/2} \quad (5.15)$$

where the subscript (m) denotes the mth order derivative and m=0 is referred to as the L₂-norm. By this definition, Eq. (5.13) requires that the third order derivative of the exact solution must be continuous when n=2. Also, from Eq. (5.13), it is clear that the consistency condition is satisfied, because the numerical solution u_h approaches to the exact solution as h goes to zero.

Numerical experiments are carried to validate the relation expressed by Eq. (5.13) by varying the mesh sizes. Both uniform and non-uniform mesh distributions are considered. The results are plotted in Figures 5.6, which show that for the problem under consideration, the convergence rate (n) is always equal to 2, whether the mesh distribution is uniform or not. At first, our results seem to be inconsistent with the conclusion given by Eq. (5.14) for non-uniform meshes. However, detailed analyses further showed that for elements with 90° inner angles such as rectangles, a superconvergence rate (n=2) is possible even for a non-uniformly distributed mesh [Lasaint and Raviart, 1974], which is supported by our numerical results here.



(a)



(b)

Figure 5.6. Convergence rate of the discontinuous method, measured by L_2 -error norm vs. the mesh size with (a) uniform mesh distribution (b) non-uniform mesh distribution. Parameters used for calculations: $T_2=T_1=0$ K, the emissivity of both plates is 1.0. $\kappa=1.0$, $\sigma=0$. The temperature of media is 100 K in case (a), but $T=100*(z-0.5)^{1/2}$ in case (b).

Mesh Adaptive Algorithm

Perhaps, one of the most attractive features of the DFE method is that the calculations are element-wise and thus a local mesh adaptive algorithm can be designed to enhance the numerical performance. A general approach to mesh refinement requires the use of the *a posteriori* error estimate as well. Various techniques for the *a posteriori* error analyses have been discussed in a recent monograph [Ainsworth and Orden, 2000]. Three different mesh adaptive strategies, e.g., r-adaptivity, h-adaptivity and p-adaptivity, are often used in numerical analyses. These strategies may be applied separately or in a combined fashion. To demonstrate the ease of incorporating adaptivity in the DFE formulation, a local *h*-adaptive algorithm is considered here.

If our objective is to make the relative L_2 -norm percentage error η less than a targeted value $\bar{\eta}$, or $\eta < \bar{\eta}$, then it is desirable to distribute the error among all elements. The total error permissible for the numerical analysis is $\bar{\eta}\|u\|_0$. In the case where an analytical solution is not possible, it may be approximated by $\bar{\eta}\|u\|_0 \approx \bar{\eta}(\|\hat{u}\|_0^2 + \|e\|_0^2)^{1/2}$, where \hat{u} is the best estimate or smoothed value and $\|e\|_0^2$ is the *a posteriori* error [Zienkiewicz and Taylor, 1989]. The global error $\|e\|_0^2$ is related to error for each element by the following expression according to the definition of the L_2 -norm,

$$\|e\|_0^2 = \sum_{i=1}^N \|e_i\|_0^2 \quad (5.16)$$

where i refers to individual elements and N is the total number of elements. In order to evenly distributed error, it is required for each element to satisfy the following error criterion,

$$\|e_i\|_0 \leq \bar{\eta} \left(\frac{\|\hat{u}\|_0^2 + \|e\|_0^2}{N} \right)^{1/2} \quad (5.17)$$

To design the next mesh refinement to satisfy the above criterion, the *a priori* error estimate (Eq. (5.14)) may be used, i.e., $\|e_i\|_0 \propto h_i^2$ for the 1-D case under consideration. Taking this into consideration, we have the required new mesh size determined by

$$h_{new}^2 \approx h^2 \|e_i\|_0 \bar{\eta}^{-1} \left(\frac{\|\hat{u}\|_0^2 + \|e\|_0^2}{N} \right)^{-1/2} \quad (5.18)$$

To test the idea, the temperature distribution is specified for the 1-D slab,

$$T(z) = 100(z - 0.5)^{1/2} \quad (5.19)$$

The numerical results were obtained using the DFE formulation with the h -adaptive refinement described above. Here a more convenient quantity to use for mesh adaptivity would be the irradiation $GP = \int_{4\pi} I(r, s) d\Omega$. The numerical results and analytical solutions are given in Figure 5.7, for which the error criterion is set to 1.0×10^{-6} . The

process started with 4 linear elements, which gave significant numerical errors. The local h -adaptive refinement is then made on the elements that have larger errors than the desired and the new errors are calculated for a new mesh distribution. This mesh refinement process continues until 22 linear elements are used. By then, the global error is approximately evenly distributed and the error criterion is met, as shown in Figure 5.7. It is noteworthy that the final 22 linear elements are not evenly distributed and the element sizes are adaptively adjusted so that the errors are evenly distributed.

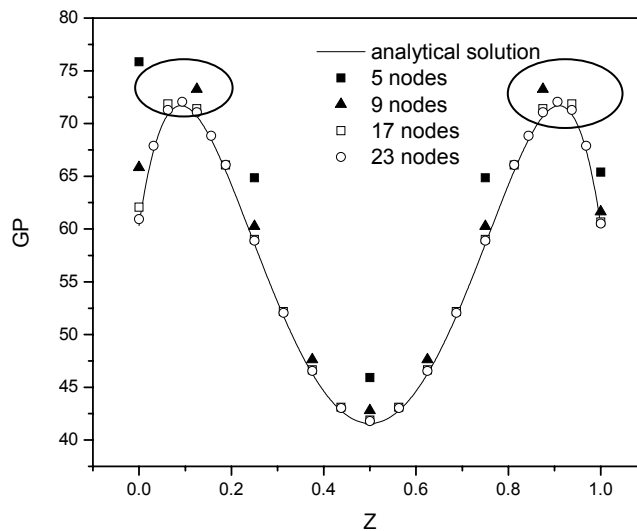
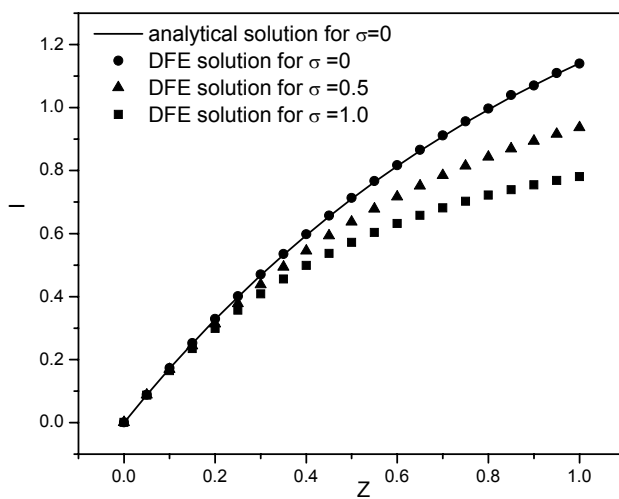


Figure 5.7. Mesh convergence for the local h -adaptive mesh refinement for radiative heat transfer calculations. Parameters used for calculations are as same as Figure 5.6(b).

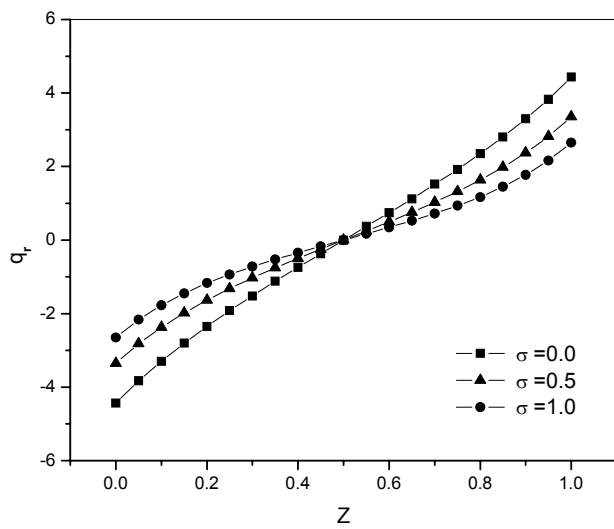
Effects Of Scattering

One of the important phenomena in radiative transfer processes is the scattering

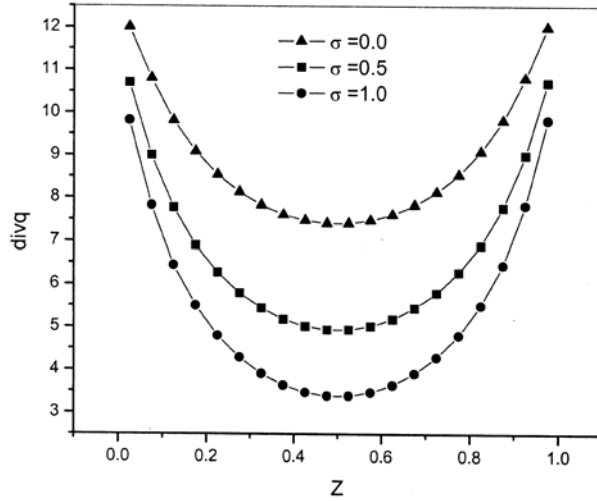
effect, which changes the local energy balance. If the participating media is scattering, the source term of the radiative transfer equation is altered such that the radiation intensity in one direction at a certain point is affected by the intensities in all directions at the point. The scattering effect can be rather easily handled by the DFE method as a source term $S(r,s)$ and normally requires an iterative procedure. Some calculated results obtained using the DFE formulation for a 1-D radiation slab filled with isotropic scattering media are shown in Figure 5.8. Inspection of these results shows that for a medium with a larger scattering coefficient, the scattering effect on the radiation intensity increases as the intensity is further away from the boundary at which it originates and the largest effect occurs when the intensity reaches the other boundary. In fact, for the intensity at $\theta=0$, the value of the intensity is reduced by 40% when it reaches at the upper boundary with the scattering coefficient $\sigma=1$. The effect at the lower boundary at which $I(\theta=0)$ originates, however, is rather small. As a result of scattering, the heat flux (absolute value) is smaller; however, the distribution is symmetric, as expected. Figure 5.8(d) compares the results of the boundary fluxes calculated using the DFE method and the analytical solution [Modest, 1993] for different scattering coefficients. Clearly, good agreement is obtained.



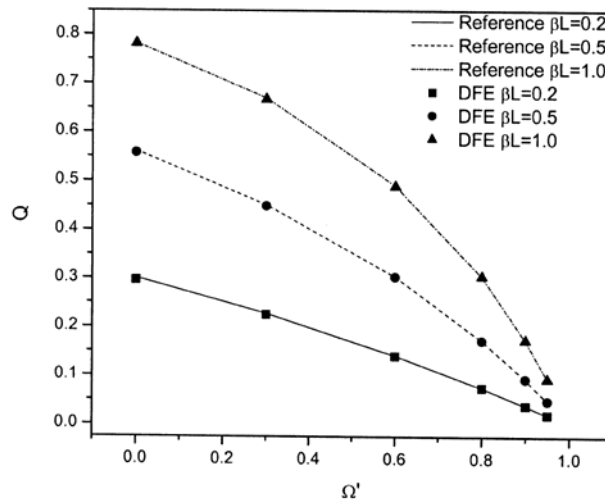
(a)



(b)



(c)



(d)

Figure 5.8. Effect of scattering on the radiative heat transfer in participating media between two infinite long plates: (a) intensity distribution, (b) heat flux distribution, (c) divergence of heat flux distribution and (d) boundary heat flux distribution. Parameters used for calculations are same as Figure 5.4, but the σ varies with different cases. In (d), The results of DFE are compared with the reported results in [Siegel, 1992], where

$Q = q_r / (\sigma T_g^4 - \sigma T_s^4)$ is the non-dimensionalized radiative heat flux and ω is the scattering albedo. The parameters are used in this case $T_g=100$ K, $T_1 = T_2 = T_s = 0$ K, the emissivity of both plates is 1.0.

Mixed Heat Transfer

Let us now consider a combined heat transfer problem that involves heat conduction and internal radiation. The problem is again 1-D, similar to that shown in Figure 5.3 but with the wall set at different temperatures so that heat conduction is required to predict the temperature distribution. Here the first approach is taken to couple the discontinuous and conventional finite element methods for the combined calculations and the divergence of the radiation heat fluxes is treated as volumetric source. Thus, the boundary condition for temperature analysis no longer involves the radiative heat flux, as it is reconciled from the internal heat transfer calculations. The calculated temperature distributions across the 1-D slab are depicted in Figure 5.9 as a function of radiation numbers. Shown also in the figure are the analytical solutions taken from [Modest, 1993]. Once again, for the entire range of the radiation parameter, the comparison between the analytical and numerical solutions is excellent; validating the combined discontinuous /conventional approach. It is noted that the coupled thermal system, however, represents a highly nonlinear system, and appropriate relaxation parameters are required to obtain converged results. Our

experience shows that selection of these parameters is often dependent on the radiation numbers. For the calculations shown in Figure 5.9, a relaxation value of 0.04 was used, when the radiation number is 0.001

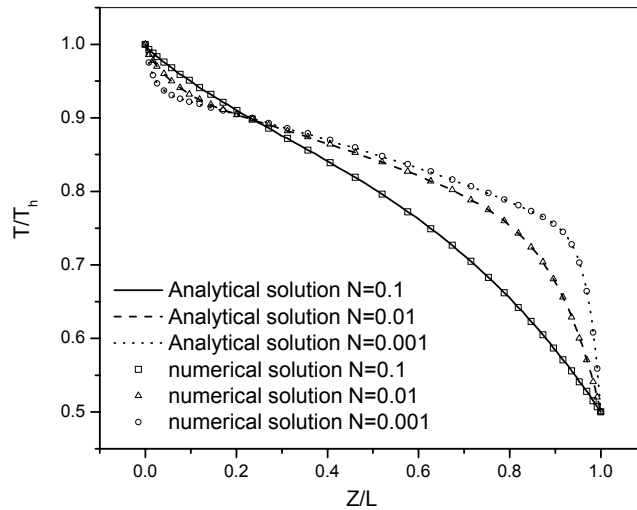


Figure 5.9. Dependence of temperature distribution across the slab on the radiation number N . Combined heat conduction and internal radiation are considered. The parameters used for calculations as the same as in Figure 5.4, except that $T(0)=1$, $T(L)=0.5$.

5.5. CONCLUDING REMARKS

This Chapter presents a discontinuous Galerkin finite element formulation for the numerical solution of internal thermal radiation problems. The essential idea of the discontinuous algorithm is that the field variables are allowed to be discontinuous across

the internal inter-element boundaries. This treatment is shown to be particularly useful for the integral-differential equations used to describe thermal radiation in absorbing/scattering media. Mathematical formulation using the discontinuous Galerkin method for internal radiation heat transfer calculations and its computer implementation were given. The convergence rate and local mesh adaptivity were also discussed. Two approaches for coupling the discontinuous with the conventional finite element method for mixed heat transfer calculations were presented. Numerical results are compared well with analytical solutions whenever available.

CHAPTER 6

A DISCONTINUOUS FINITE ELEMENT FORMULATION FOR MULTI-DIMENSIONAL RADIATIVE TRANSFER IN ABSORBING, EMITTING AND SCATTERING MEDIA

6.1 INTRODUCTION

In the previous chapter, we presented a discontinuous finite element formulation for one-dimensional problems of thermal radiation in absorbing and scattering media. The underlying idea of the formulation is that field variable values across an inter-element boundary are allowed to be discontinuous. There it was shown that the discontinuous finite element method combines the salient features of both finite element volume and finite elements and has several important advantages over the numerical methods currently in use today, including the finite volume and finite element methods, for the thermal radiation problems. It is a local method with a higher order accuracy and geometric flexibility. Also, the program can be fairly easily combined with either the existing finite element method or the finite volume method for the mixed heat transfer calculations, which was demonstrated using 1-D examples in Chapter 5. In addition, it is fairly straightforward and easy to implement within a parallel computing framework, because of its localized nature of formulation. This last feature can be very useful for the

computation of thermal radiation problems in multidimensional domains, as these types of computations can be very time consuming, especially when absorbing and scattering media are considered.

In this chapter, the discontinuous finite element method is extended to the solution of multi-dimensional thermal radiation problems that involve absorbing, emitting and scattering media. Both 2-D and 3-D computations are considered. As with other applications, 2-D and 3-D calculations for internal thermal radiation problems are much more involved than 1-D computations. The calculations use unstructured meshes, though structured meshes can also be used. Mathematical formulations and essential numerical details are given for 2-D and 3-D linear elements. The implementation of parallel algorithm and its computational performance are also discussed. Examples of various degrees of difficulty are given and are compared with available solutions reported in literature obtained using the other methods.

6.2 THE DISCONTINUOUS FINITE ELEMENT FORMULATION

In this chapter, the application of the discontinuous finite element method to the solution of radiative heat transfer problems in multiple-dimension is discussed. The radiative heat transfer problem in three-dimension can be shown in Fig. 6.1.

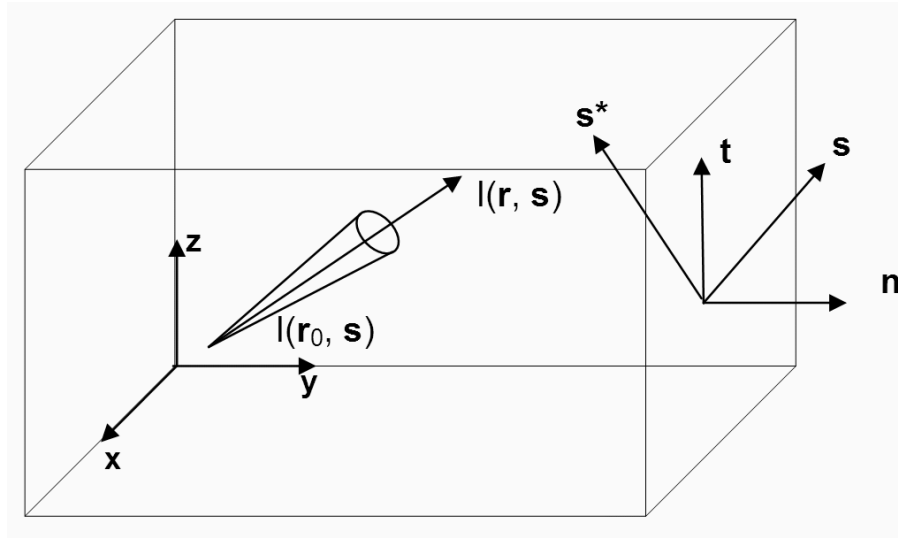
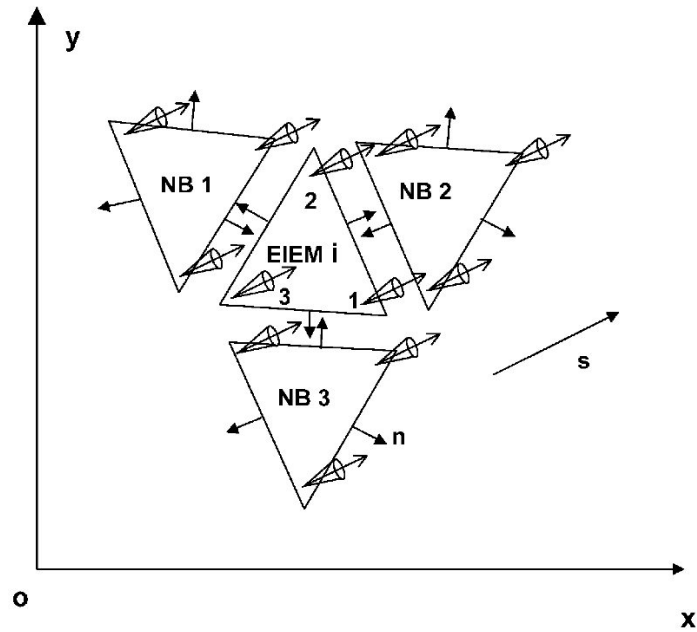
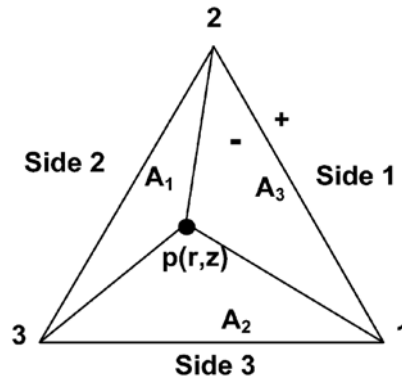


Figure 6.1 Schematic representation of radiative transfer in a participating medium and definition of the direction of radiation intensity and symmetry boundary condition.

As with other methods, the domain is first discretized into a collection of finite elements. In this study, unstructured meshes are used, with triangular elements for 2-D problems and tetrahedral, hexahedral *et al.* elements for 3-D problems. Let us consider the i th element in a 2-D mesh, as shown in Figure 6.2.



(a)



(b)

Figure 6.2. Illustration of discontinuous finite-element formulation for 2-D internal radiation transfer in absorbing and emitting media using unstructured triangular meshes: (a) element i , its boundary normals, and its neighboring elements; (b) local node number

and side number of a typical triangular element (or i th element).

First the formulations will be derived in two dimensional geometries, and will be extended to three dimensional geometries later. Integrate Eq. (2.7) in Chapter 2 over the element i in Figure 6.2(b) respect to a weighting function $v(\Omega, x)$,

$$\int_{\Delta A} \phi \int_{\Delta \Omega_i} \mathbf{s} \cdot \nabla I d\Omega dA = \int_{\Delta A} \phi \int_{\Delta \Omega_i} (-\beta(\mathbf{r})I(\mathbf{r}, \mathbf{s}) + S(\mathbf{r}, \mathbf{s})) d\Omega dA \quad (6.1)$$

where $\mathbf{r} = x\hat{i} + y\hat{j}$ and $S(\mathbf{r}, \mathbf{s})$ is the source function defined by

$$S(\mathbf{r}, \mathbf{s}) = \kappa(\mathbf{r})I_b(\mathbf{r}) + \frac{\sigma(\mathbf{r})}{4\pi} \int_{4\pi} I(\mathbf{r}, \mathbf{s}')\Phi(\mathbf{s}, \mathbf{s}')d\Omega' \quad (6.2)$$

Integrating by parts gives the following expression,

$$\int_{\Delta A_i} \int_{\Delta \Omega} \phi \mathbf{s} \cdot \nabla I dA d\Omega + \int_{\Delta \Omega} \int_{\Gamma^-} \phi [I] \mathbf{n} \cdot \mathbf{s} d\Omega d\Gamma = \int_{\Delta A} \phi \int_{\Delta \Omega_i} (-\beta(\mathbf{r})I(\mathbf{r}, \mathbf{s}) + S(\mathbf{r}, \mathbf{s})) d\Omega dA \quad (6.4)$$

where \mathbf{n} is the outnormal and use has been made of the divergence theorem,

$$\mathbf{s} \cdot \int_A \phi I \mathbf{n} dA - \mathbf{s} \cdot \int_{\Delta V} I \nabla \phi dV = \mathbf{s} \cdot \int_{\Delta V} \phi \nabla I dV \quad (6.5)$$

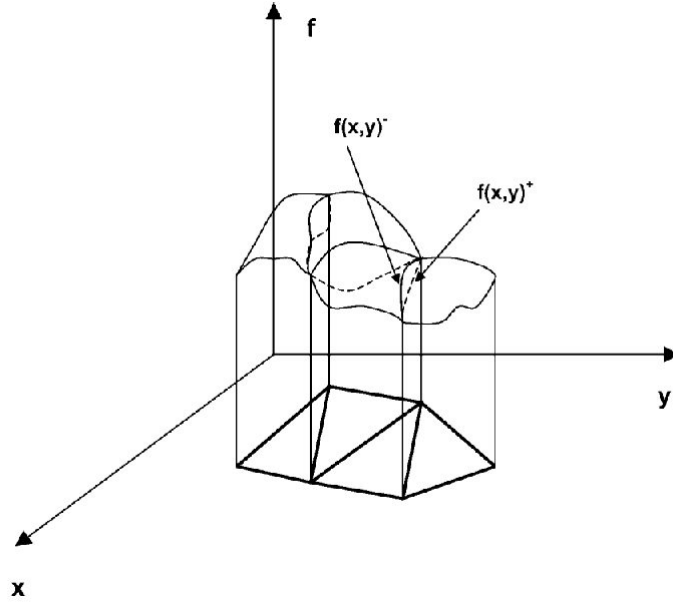


Figure 6.3: Schematic sketch of discontinuous finite-element broken space.

To convert the domain integral into the boundary integral. Note that \mathbf{s} is the unit vector of the direction of radiation intensity $I(\mathbf{r}, \mathbf{s})$ and is independent of the volume. In the conventional finite element formulation, the terms on the boundary disappear when they are combined with neighboring elements or $[I] = 0$. In the discontinuous formulation, however, these terms do not go away when elements are assembled. Instead, the following limiting values are used,

$$I_j^+ = \lim_{\mathbf{r}_j \rightarrow \Gamma^+} I(\mathbf{r}_j) \quad \text{and} \quad I_j^- = \lim_{\mathbf{r}_j \rightarrow \Gamma^-} I(\mathbf{r}_j)$$

If the elements are now assembled, the boundary terms will experience jumps across the element boundaries as shown in Figure 6.3 and these jumps are often denoted by,

$$[I]_j = I_j^+ - I_j^-$$

These jumps may also be modeled by the generic numerical fluxes that are single-valued at the boundaries and are a function of field values across the inter-element boundaries [Cui and Li, 2004a]. For the problems under consideration, the simplest and yet effective choice is the upwinding, which in the discontinuous finite element literature is some times referred to as the inflow boundary value,

$$[I]_j = \begin{cases} I_j^- & \text{if } \mathbf{n} \cdot \mathbf{s} < 0 \\ I_j^+ & \text{if } \mathbf{n} \cdot \mathbf{s} > 0 \end{cases} \quad (6.6)$$

We may now use the appropriate interpolation functions, which can be chosen from the finite element broken space that requires no continuity across the inter-element boundaries [Moder *et al.* 2000]. A natural choice of shape functions for the internal radiation applications is to take the delta function for the solid angle and a polynomial function for spatial variation, $v(\Omega, x) = \psi(\Omega, x)\phi(x)$. Here $\psi(\Omega, x)$ is the step function and $\phi(x)$ the shape function. Substituting this testing function into the integral expression and re-arranging, one has the following relation,

$$\begin{aligned} & \mathbf{s} \cdot \int_{\Delta\Omega_l} \int_{\Delta A_l} \phi \sum_{j=1}^{Nd} (I_j \nabla \phi_j) d\Omega dA + \int_{\Delta\Omega_l} \int_{\Gamma^-} \phi [I] (-\mathbf{n}_w \cdot \mathbf{s}) d\Omega d\Gamma \\ & = \int_{\Delta\Omega_l} \int_{\Delta A_l} -\beta(\mathbf{r}) \phi (I_1 \phi_1 + I_2 \phi_2 + I_3 \phi_3) dA + -\phi (S_1 \phi_1 + S_2 \phi_2 + S_3 \phi_3) dA d\Omega \end{aligned} \quad (6.7)$$

where N_d is the number of nodes per element.

Before the numerical implementation is considered, a few points are worthy noting. First, if the jump condition $[I]$ is set to zero in Eq. (6.4), which means that the inter-element continuity is enforced, then the conventional finite element formulation is recovered. Second, if the zeroth order polynomial is chosen as the spatial interpolation function, then we have the common finite volume formulation. Thus, in this sense, the finite volume method is a subclass of the discontinuous finite element method, and uses the lowest order approximation to the field variables.

6.3 NUMERICAL IMPLEMENTATION

In this section, we discuss below the numerical implementation of the general discontinuous finite element formulation described above for both 2-D and 3-D calculations and give the analytical expressions for the elemental calculations for 2-D linear triangular elements and 3-D linear tetrahedral elements. Although the derivations are presented for unstructured meshes, the numerical procedures are equally applicable to structured meshes.

2-D calculations

We consider again the i th element and its neighbors as shown in Figure 6.2(a). For the sake of discussion, the inter-element boundaries are plotted separately. The nodal

values of the variable are defined within the element. Since the discontinuity is allowed across the element boundaries, the common geometric node does not have the same field variable value. This is an essential difference between the conventional and the discontinuous finite element formulations.

For a 2-D linear triangular element, the shape functions may be written in terms of natural coordinates,

$$\begin{bmatrix} \phi_1 \\ \phi_2 \\ \phi_3 \end{bmatrix} = \begin{bmatrix} \lambda_1 \\ \lambda_2 \\ \lambda_3 \end{bmatrix} \quad (6.8)$$

Here λ_p ($p=1,2,3$) is defined by the area ratio,

$$\lambda_p = \frac{A_p}{A_e}$$

where A_e is the area of the element and A_p the sub-triangular area formed from two vertices and point p inside the element (see Figure 6.2(b)). With relevant global coordinates substituted in to λ_p , the shape functions take the following form,

$$\begin{bmatrix} \phi_1 \\ \phi_2 \\ \phi_3 \end{bmatrix} = \frac{1}{2A} \begin{bmatrix} x_2y_3 - x_3y_2 & y_{23} & x_{32} \\ x_3y_1 - x_1y_3 & y_{31} & x_{13} \\ x_1y_2 - x_2y_1 & y_{12} & x_{21} \end{bmatrix} \begin{bmatrix} 1 \\ x \\ y \end{bmatrix} \quad (6.9)$$

where $x_{ij} = x_i - x_j$ and $y_{ij} = y_i - y_j$ ($i, j = 1, 2, 3$).

The radiation intensity inside the element is interpolated using the above shape

functions,

$$I(x, y; s) = I_1\phi_1 + I_2\phi_2 + I_3\phi_3$$

Substituting the above equation to Eq (6.7), and noting that the intensity with control angles is constant, one has the following expression,

$$\begin{aligned} & \int_{\Delta\Omega_l} \mathbf{s} \cdot \int_{\Delta A_l} \begin{bmatrix} \phi_1 \\ \phi_2 \\ \phi_3 \end{bmatrix} [\nabla\phi_1, \nabla\phi_2, \nabla\phi_3] \begin{bmatrix} I_1 \\ I_2 \\ I_3 \end{bmatrix} d\Omega dA + \int_{\Delta\Omega_l} \int_{\Gamma^-} \begin{bmatrix} \phi_1 \\ \phi_2 \\ \phi_3 \end{bmatrix} [\phi_1 \quad \phi_2 \quad \phi_3] \begin{bmatrix} [I]_1 \\ [I]_2 \\ [I]_3 \end{bmatrix} (\mathbf{n}_w \cdot \mathbf{s}) d\Omega d\Gamma \\ & = \int_{\Delta\Omega_l} \int_{\Delta A_l} \{-\beta(\mathbf{r}) \begin{bmatrix} \phi_1 \\ \phi_2 \\ \phi_3 \end{bmatrix} [\phi_1 \quad \phi_2 \quad \phi_3] \begin{bmatrix} I_1 \\ I_2 \\ I_3 \end{bmatrix} + \begin{bmatrix} \phi_1 \\ \phi_2 \\ \phi_3 \end{bmatrix} S(\mathbf{r})\} d\Omega dA \end{aligned} \quad (6.10)$$

where \mathbf{n}_w is the outward normal of the i th element. For a 2-D triangular element, the above integration can be carried out analytically. Taking the derivative of the shape functions,

$$\begin{bmatrix} \nabla\phi_1 \\ \nabla\phi_2 \\ \nabla\phi_3 \end{bmatrix} = \frac{1}{J} \begin{bmatrix} y_{23} & x_{32} & 0 \\ y_{31} & x_{13} & 0 \\ y_{12} & x_{21} & 0 \end{bmatrix} \begin{bmatrix} \hat{i} \\ \hat{j} \\ \hat{k} \end{bmatrix} \quad (6.11)$$

and making a dot-product of it with the unit direction vector,

$\mathbf{s} = \sin\theta \cos\varphi \hat{i} + \sin\theta \sin\varphi \hat{j} + \cos\theta \hat{k}$, one has

$$\mathbf{s} \cdot \begin{bmatrix} \nabla \phi_1 \\ \nabla \phi_2 \\ \nabla \phi_3 \end{bmatrix} = \frac{1}{2A} \begin{bmatrix} y_{23} & x_{32} & 0 \\ y_{31} & x_{13} & 0 \\ y_{12} & x_{21} & 0 \end{bmatrix} \begin{bmatrix} \sin \theta \cos \varphi \\ \sin \theta \sin \varphi \\ \cos \theta \end{bmatrix} = \frac{1}{2A} \begin{bmatrix} y_{23} \sin \theta \cos \varphi + x_{23} \sin \theta \sin \varphi \\ y_{31} \sin \theta \cos \varphi + x_{13} \sin \theta \sin \varphi \\ y_{12} \sin \theta \cos \varphi + x_{21} \sin \theta \sin \varphi \end{bmatrix} \quad (6.12)$$

With the above two equations, the first integral in Eq. (6.7) can be expressed as

$$\begin{aligned} \int_{\Delta\Omega} \int_{\Delta A_l} \begin{bmatrix} \phi_1 \\ \phi_2 \\ \phi_3 \end{bmatrix} [s \cdot \nabla \phi_1, s \cdot \nabla \phi_2, s \cdot \nabla \phi_3] dA d\Omega &= \int_{\Delta A_l} \begin{bmatrix} \phi_1 \\ \phi_2 \\ \phi_3 \end{bmatrix} dA \int_{\Delta\Omega} \frac{1}{2A} \begin{bmatrix} y_{23} \sin \theta \cos \varphi + x_{23} \sin \theta \sin \varphi \\ y_{31} \sin \theta \cos \varphi + x_{13} \sin \theta \sin \varphi \\ y_{12} \sin \theta \cos \varphi + x_{21} \sin \theta \sin \varphi \end{bmatrix} d\Omega \\ &= \frac{1}{6} \int_{\Delta\Omega_l} \begin{bmatrix} y_{23} \sin \theta \cos \varphi + x_{23} \sin \theta \sin \varphi \\ y_{31} \sin \theta \cos \varphi + x_{13} \sin \theta \sin \varphi \\ y_{12} \sin \theta \cos \varphi + x_{21} \sin \theta \sin \varphi \end{bmatrix} d\Omega \end{aligned} \quad (6.13)$$

The second integral in Eq. (6.10) represents the jump condition (or numerical fluxes) across the boundary of the i th element and its neighbor (see Figure 6.2). For a linear triangular element, it is split into three terms, one for each side of the element,

$$\begin{aligned} \int_{\Delta\Omega} \int_{\Gamma^-} \begin{bmatrix} \phi_1 \\ \phi_2 \\ \phi_3 \end{bmatrix} [\phi_1, \phi_2, \phi_3] \begin{bmatrix} [I]_1 \\ [I]_2 \\ [I]_3 \end{bmatrix} (-\mathbf{n}_w \cdot \mathbf{s}) d\Gamma d\Omega &= \int_{\Gamma^-} \begin{bmatrix} \phi_1 \\ \phi_2 \\ \phi_3 \end{bmatrix} [\phi_1, \phi_2, \phi_3] \begin{bmatrix} [I]_1 \\ [I]_2 \\ [I]_3 \end{bmatrix} d\Gamma_1 \int_{\Delta\Omega} (-\mathbf{n}_{w1} \cdot \mathbf{s}) d\Omega \\ &+ \int_{\Gamma_2^-} \begin{bmatrix} \phi_1 \\ \phi_2 \\ \phi_3 \end{bmatrix} [\phi_1, \phi_2, \phi_3] \begin{bmatrix} [I]_1 \\ [I]_2 \\ [I]_3 \end{bmatrix} d\Gamma_2 \int_{\Delta\Omega} (-\mathbf{n}_{w2} \cdot \mathbf{s}) d\Omega \\ &+ \int_{\Gamma_3^-} \begin{bmatrix} \phi_1 \\ \phi_2 \\ \phi_3 \end{bmatrix} [\phi_1, \phi_2, \phi_3] \begin{bmatrix} [I]_1 \\ [I]_2 \\ [I]_3 \end{bmatrix} d\Gamma_3 \int_{\Delta\Omega} (-\mathbf{n}_{w3} \cdot \mathbf{s}) d\Omega \end{aligned} \quad (6.14)$$

The line integration associated with the element can be carried out analytically.

For side 1, $\phi_3 = 0$, and $\phi_1 + \phi_2 = 1$, we therefore have

$$\begin{aligned}
& \int_{\Gamma_1^-} \begin{bmatrix} \phi_1 \\ \phi_2 \\ \phi_3 \end{bmatrix} [\phi_1 \quad \phi_2 \quad \phi_3] d\Gamma_1 = \int_{\Gamma_1^-} \begin{bmatrix} \phi_1 \\ \phi_2 \\ 0 \end{bmatrix} [\phi_1 \quad \phi_2 \quad 0] d\Gamma_1 \\
& = \int_0^1 \begin{bmatrix} \phi_1 \phi_1 & \phi_1(1-\phi_1) & 0 \\ (1-\phi_1)\phi_1 & (1-\phi_1)(1-\phi_1) & 0 \\ 0 & 0 & 0 \end{bmatrix} L_1 d\phi_1 = \frac{L_1}{6} \begin{bmatrix} 2 & 1 & 0 \\ 1 & 2 & 0 \\ 0 & 0 & 0 \end{bmatrix}
\end{aligned} \tag{6.15}$$

where L_1 is the length of side 1. The term involving the solid angle integration can also be treated analytically,

$$\begin{aligned}
NDS_{i1} &= \int_{\Delta\Omega} (-\mathbf{n}_{w1} \cdot \mathbf{s}) d\Omega \\
&= [0.5(\theta_2 - \theta_1) - 0.25(\sin 2\theta_2 - \sin 2\theta_1)] [(\sin \varphi_1 - \sin \varphi_2)N_x - (\cos \varphi_1 - \cos \varphi_2)N_y] \\
&\quad - 0.25(\cos 2\theta_1 - \cos 2\theta_2)(\varphi_2 - \varphi_1)N_z
\end{aligned} \tag{6.16}$$

To simplify the notations, from here on $\int_{\Delta\Omega} (-\mathbf{n}_{wj} \cdot \mathbf{s}) d\Omega$ is denoted by NDS_{ij} , with i refers to the i th element and j the j th side of the element. In the discontinuous finite element treatment, the jump terms have to be selected depending on the sign of $-\mathbf{n}_{w1} \cdot \mathbf{s}$. This is different from the conventional finite element formulation in which the across-element continuity is enforced. One treatment that works effectively with linear elements is the upwinding scheme. By this scheme,

$$\begin{bmatrix} [I]_1 \\ [I]_2 \\ [I]_3 \end{bmatrix} NDS_{i1} = \max(0, NDS_{i1}) \begin{bmatrix} I_1 \\ I_2 \\ I_3 \end{bmatrix}_{Elemi} - \max(0, NDS_{i1}) \begin{bmatrix} I_1^- \\ I_2^- \\ I_3^- \end{bmatrix}_{NB1} \tag{6.17}$$

By the same token, the calculations for other two sides can also be performed

analytically. The results are summarized below for convenience,

$$\begin{aligned}
& \int_{\Gamma_j^-} \begin{bmatrix} \phi_1 \\ \phi_2 \\ \phi_3 \end{bmatrix} [\phi_1, \phi_2, \phi_3] \begin{bmatrix} [I]_1 \\ [I]_2 \\ [I]_3 \end{bmatrix} d\Gamma_1 \int_{\Delta\Omega} (-\mathbf{n}_{wj} \cdot \mathbf{s}) d\Omega \\
&= \frac{L_j}{6} \text{Cof}B_{(4-j,4-j)} \max(0, NDS_{ij}) \left\{ \begin{bmatrix} I_1 \\ I_2 \\ I_3 \end{bmatrix}_{Elem_i} - \begin{bmatrix} I_1^+ \\ I_2^+ \\ I_3^+ \end{bmatrix}_{NB_j} \right\} \quad (6.18)
\end{aligned}$$

where $\text{Cof}B_{k1}$ is the cofactor of matrix B, which is defined by

$$B = \begin{bmatrix} 2 & 1 & 1 \\ 1 & 2 & 1 \\ 1 & 1 & 2 \end{bmatrix}$$

The first term on the right hand side of Eq. (6.10) may be calculated analytically

when $\beta(\mathbf{r})$ is a constant with the result,

$$\begin{aligned}
& \beta(r,s) A \int_{\Delta\Omega} \int_{\Delta A_l} \begin{bmatrix} \phi_1 \\ \phi_2 \\ \phi_3 \end{bmatrix} [\phi_1, \phi_2, \phi_3] dA = \beta(r,s) A \int_{\Delta\Omega} \int_{\Delta A_l} \begin{bmatrix} \phi_1\phi_1 & \phi_1\phi_2 & \phi_1\phi_3 \\ \phi_2\phi_1 & \phi_2\phi_2 & \phi_2\phi_3 \\ \phi_3\phi_1 & \phi_3\phi_2 & \phi_3\phi_3 \end{bmatrix} dA \\
&= \beta(r,s) \frac{A}{12} \int_{\Delta\Omega} \begin{bmatrix} 2 & 1 & 1 \\ 1 & 2 & 1 \\ 1 & 1 & 2 \end{bmatrix} d\Omega \quad (6.19)
\end{aligned}$$

Assembling all these discretized terms together, the equation for the element can

be written in terms of the following matrix form,

$$[K]\{I\} = \{f\} \quad (6.20)$$

where the expressions for the matrix elements are summarized as follows,

$$k_{ij} = \int_{\Delta A} \phi_i \nabla \phi_j \cdot \int_{\Delta \Omega_l} \mathbf{s} d\Omega dA + \beta \int_{\Delta A} \phi_i \phi_j dA + \sum_{k=1}^{Nd} \max(0, - \int_{\Delta \Omega_l} \mathbf{s} \cdot \mathbf{n}_k d\Omega) \int_{\Gamma_k} \phi_i \phi_j d\Gamma \quad (6.21)$$

$$f_i = \int_{\Delta z_m} \phi_i S_i dA + \sum_{k=1}^{Nd} \max(0, - \int_{\Delta \Omega} \mathbf{s} \cdot \mathbf{n}_k d\Omega) \int_{\Gamma_k} \phi_i \phi_j I_{nb} d\Gamma \quad (6.22)$$

The calculations will start with those associated with a boundary element, where the boundary condition is imposed for a gray boundary as follows,

$$I^-(\mathbf{r}, \mathbf{s}_l) = \varepsilon(\mathbf{r}) I_b(\mathbf{r}) + \frac{1 - \varepsilon(\mathbf{r})}{2\pi} \sum_{j=0, \mathbf{s}_j' \cdot \mathbf{n} < 0}^{N_\theta} I^+(\mathbf{r}, \mathbf{s}_j') | \mathbf{s}_j' \cdot \mathbf{n} | \Delta \Omega'_j \quad (6.23)$$

and Eq (6.24) is for the symmetry boundary condition,

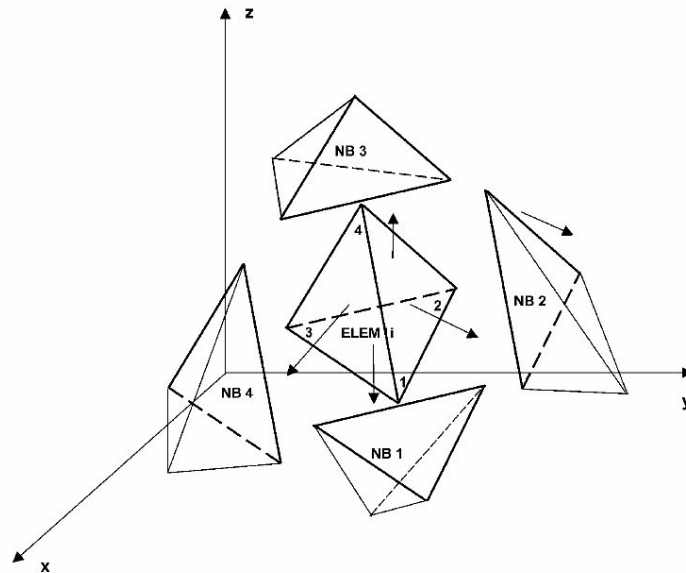
$$I^-(\mathbf{r}, \mathbf{s}_l) = I(\mathbf{r}, \mathbf{s}_l^*) \quad (6.24)$$

Here \mathbf{s}^* is the symmetric direction of \mathbf{s} respected to the boundary, and can be calculated by Eq (2.14) in Chapter 2. Note that Eq (6.21) can be obtained for each element and its neighbors and the calculations are then performed element by element. Thus, with Eq. (6.21), the calculation for the i th element starts with selecting a direction and continues element by element until the entire domain and all directions are covered. Because of the boundary conditions, iterative procedures are required. The successive

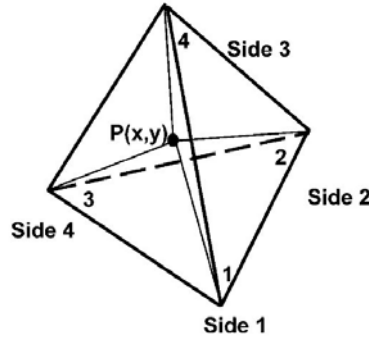
substitution method seems to work well for this type of problems. In the above, it is assumed that the medium is not scattering and thus the source term is set to zero. When the source term is known, it can be readily calculated using the Gaussian integration and included in the force vector $\{f\}$.

6.4 3-D CALCULATIONS

The above procedures are applicable to 3-D calculations. The element arrangement for 3-D calculations is shown in Figure 6.4. For a 3-D element, the area integral above is replaced by a volume integral and the boundary line integral above by a surface integral, respectively. For a linear tetrahedral element, the integrations can be carried out analytically.



(a)



(b)

Figure 6.4. Illustration of discontinuous finite-element formulation for 3-D internal radiation transfer in absorbing and emitting media using unstructured tetrahedral meshes: (a) element i , its surface normals, and its neighboring elements; (b) local node number and side number of a typical tetrahedral element (or i th element).

In an analogy to a 2-D triangular element, the shape function for a tetrahedral element has the following form when written in the global coordinate system,

$$\begin{bmatrix} \phi_1 \\ \phi_2 \\ \phi_3 \\ \phi_4 \end{bmatrix} = \frac{1}{6V} \begin{bmatrix} -V_{234} & X_1 & Y_1 & Z_1 \\ V_{341} & -X_2 & -Y_2 & -Z_2 \\ -V_{412} & X_3 & Y_3 & Z_3 \\ V_{123} & -X_4 & -Y_4 & -Z_4 \end{bmatrix} \begin{bmatrix} 1 \\ x \\ y \\ z \end{bmatrix} \quad (6.25)$$

where the definition of elements in Eq(6.25) is following,

$$V_{ijk} = \begin{vmatrix} x_i & x_j & x_k \\ y_i & y_j & y_k \\ z_i & z_j & z_k \end{vmatrix}, \quad X_1 = \begin{vmatrix} 1 & 1 & 1 \\ y_2 & y_3 & y_4 \\ z_2 & z_3 & z_4 \end{vmatrix}, \quad Y_1 = \begin{vmatrix} 1 & 1 & 1 \\ z_2 & z_3 & z_4 \\ x_2 & x_3 & x_4 \end{vmatrix}, \quad Z_1 = \begin{vmatrix} 1 & 1 & 1 \\ x_2 & x_3 & x_4 \\ y_2 & y_3 & y_4 \end{vmatrix}$$

rest of them can be defined by same way, except the sequence of i,j,k is defined anticlockwise.

The radiation intensity within a tetrahedron is interpolated by,

$$I(x,y,z;s) = \sum_{i=1}^4 \phi_i I_i = \phi_1 I_1 + \phi_2 I_2 + \phi_3 I_3 + \phi_4 I_4 \quad (6.26)$$

Substituting into the general formulation Eq. (6.4), we have

$$\begin{aligned} & \int_{\Delta\Omega_l} \mathbf{s} d\Omega \cdot \int_{\Delta V_l} \begin{bmatrix} \phi_1 \\ \phi_2 \\ \phi_3 \\ \phi_4 \end{bmatrix} [\nabla\phi_1 \quad \nabla\phi_2 \quad \nabla\phi_3 \quad \nabla\phi_4] \begin{bmatrix} I_1 \\ I_2 \\ I_3 \\ I_4 \end{bmatrix} dV \\ & + \sum_{i=1}^4 \int_{\Lambda\Omega} \begin{bmatrix} \phi_1 \\ \phi_2 \\ \phi_3 \\ \phi_4 \end{bmatrix} [\phi_1, \phi_2, \phi_3, \phi_4] \begin{bmatrix} [I]_1 \\ [I]_2 \\ [I]_3 \\ [I]_4 \end{bmatrix} (-\mathbf{n}_{wi} \cdot \mathbf{s}) d\Omega d\Gamma \\ & = \int_{\Delta\Omega} \int_{\Delta V_l} \{-\beta(\mathbf{r}) \begin{bmatrix} \phi_1 \\ \phi_2 \\ \phi_3 \\ \phi_4 \end{bmatrix} [\phi_1 \quad \phi_2 \quad \phi_3 \quad \phi_4] \begin{bmatrix} I_1 \\ I_2 \\ I_3 \\ I_4 \end{bmatrix} + \begin{bmatrix} \phi_1 \\ \phi_2 \\ \phi_3 \\ \phi_4 \end{bmatrix} S(\mathbf{r})\} d\Omega dV \end{aligned} \quad (6.27)$$

Once again, the derivative of the shape functions can be obtained analytically

with the following result,

$$\begin{bmatrix} \nabla\phi_1 \\ \nabla\phi_2 \\ \nabla\phi_3 \\ \nabla\phi_4 \end{bmatrix} = \frac{1}{J} \begin{bmatrix} X_1 & Y_1 & Z_1 \\ -X_2 & -Y_2 & -Z_2 \\ X_3 & Y_3 & Z_3 \\ -X_4 & -Y_4 & -Z_4 \end{bmatrix} \begin{bmatrix} \hat{i} \\ \hat{j} \\ \hat{k} \end{bmatrix} \quad (6.28)$$

where $J = \frac{1}{6V}$ is the Jacobin of tetrahedral element. This will allow us to analytically integrate the volume terms in Eq. (6.27). Following the same procedure as for the 2-D calculations, we have the following result for the 3-D tetrahedral elements,

$$\int_{\Delta\Omega_i} \int_{\Delta V_i} \begin{bmatrix} \phi_1 \\ \phi_2 \\ \phi_3 \\ \phi_4 \end{bmatrix} [s \cdot \nabla \phi_1, s \cdot \nabla \phi_2, s \cdot \nabla \phi_3, s \cdot \nabla \phi_4] dV d\Omega \quad (6.29)$$

$$= \frac{1}{6} \begin{bmatrix} DS \cdot \nabla \phi_1 & DS \cdot \nabla \phi_2 & DS \cdot \nabla \phi_3 & DS \cdot \nabla \phi_4 \\ DS \cdot \nabla \phi_1 & DS \cdot \nabla \phi_2 & DS \cdot \nabla \phi_3 & DS \cdot \nabla \phi_4 \\ DS \cdot \nabla \phi_1 & DS \cdot \nabla \phi_2 & DS \cdot \nabla \phi_3 & DS \cdot \nabla \phi_4 \\ DS \cdot \nabla \phi_1 & DS \cdot \nabla \phi_2 & DS \cdot \nabla \phi_3 & DS \cdot \nabla \phi_4 \end{bmatrix}$$

where

$$\begin{aligned} DS \cdot \nabla \phi_1 &= DS_x X1 + DS_y Y1 + DS_z Z1 \\ DS \cdot \nabla \phi_2 &= -DS_x X2 - DS_y Y2 - DS_z Z2 \\ DS \cdot \nabla \phi_3 &= DS_x X3 + DS_y Y3 + DS_z Z3 \\ DS \cdot \nabla \phi_4 &= -DS_x X4 - DS_y Y4 - DS_z Z4 \end{aligned} \quad (6.30)$$

The consideration for the solid angles and sign of $-\mathbf{n}_{wj} \cdot \mathbf{s}$ is also the same as for the 2-D case discussed above. The calculations give the final result as follows,

$$\int_{\Gamma_j^-} \begin{bmatrix} \phi_1 \\ \phi_2 \\ \phi_3 \\ \phi_4 \end{bmatrix} [\phi_1, \phi_2, \phi_3, \phi_4] \begin{bmatrix} [I]_1 \\ [I]_2 \\ [I]_3 \\ [I]_4 \end{bmatrix} d\Gamma \int_{\Delta\Omega} (-\mathbf{n}_{wj} \cdot \mathbf{s}) d\Omega$$

$$= \frac{A_j}{12} \text{Cof}C_{(s-j,5-j)} \max(0, NDS_{ij}) \left\{ \begin{array}{c} \left[\begin{array}{c} I_1 \\ I_2 \\ I_3 \\ I_4 \end{array} \right]_{Elem_i} - \left[\begin{array}{c} I_1^+ \\ I_2^+ \\ I_3^+ \\ I_4^+ \end{array} \right]_{NB_j} \end{array} \right\} \quad (6.31)$$

where $\text{Cof}C_{kl}$ is the cofactor of matrix C, which is defined by

$$C = \begin{bmatrix} 2 & 1 & 1 & 1 \\ 1 & 2 & 1 & 1 \\ 1 & 1 & 2 & 1 \\ 1 & 1 & 1 & 2 \end{bmatrix} \quad (6.32)$$

Again, the above equations for 3-D calculations can be summarized in the same matrix form as given by Eq. (6.20).

6.5 PARALLEL ALGORITHM

The iterative process associated with the DFE (discontinuous finite element) solution of radiation problems can be overwhelmingly time consuming, especially for the cases where the temperature of media is not constant. In order to increase the computational speed, a parallel algorithm may be used to take the advantage of the modern parallel computer architectures and the localized formulation presented above (see Eq. (6.2)). Parallel computing has been a subject in the radiative heat transfer community and has been successfully along with other numerical methods. Burns and Christon (1997) reported a domain-based parallelism with the Discrete Ordinates method

to solve radiative heat transfer problems. Cumber and Beer (1998) discussed the parallel strategy for radiative transfer using the finite volume method. Here, a parallelization of DFE computations is considered. Since the calculation of radiation intensity of internal radiation involves both space and direction, the parallel strategy for the DFE calculations can be implemented in two different ways. One is based on domain partition, and the other is based on control angle partition, as shown in Figure 6.5. By the first approach, the spatial domain is partitioned into several sub-domains, and each sub-domain is calculated by a different microprocessor at the same time. Once one round iteration is completed, the microprocessors communicate the results among themselves, update the information in memory and then start the next iteration. The shortcoming of this parallel scheme is that considerable time will be spent in sending and receiving the information between slave processors. The other parallel approach entails partitioning the solid angle to several sub-angles, and the intensity distribution over the entire domain is calculated by a different microprocessor for each sub-angle. By this approach, the slave processors do not have to communicate the information among themselves, after a convergence is achieved instead of every single iteration step. This seems to require less time on sending and receiving data, in comparison with the spatial domain partitioning as taken by the first approach [Kim and Lee, 1998; Wiscombe, 1980]. To demonstrate the parallel implementation of the DFE solution, this study adopts the second approach.

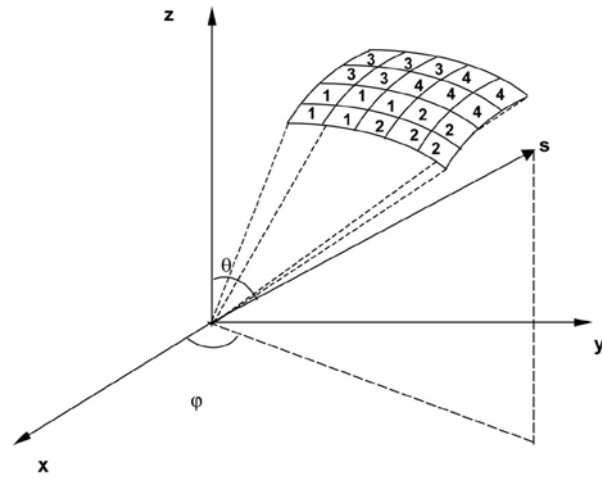
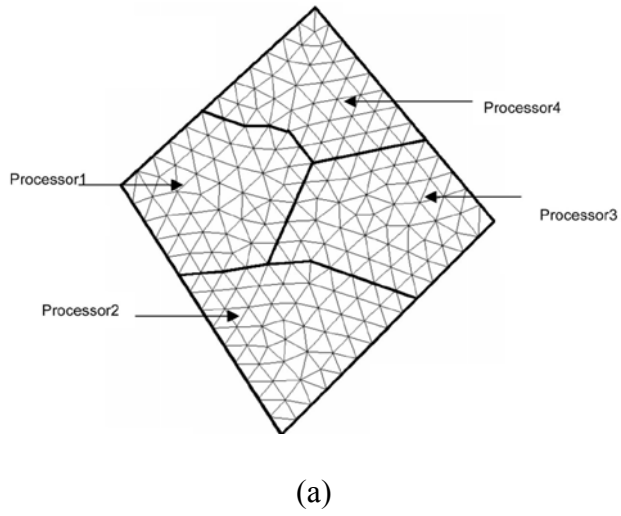


Figure 6.5 Two types of partitioning for parallel computation of internal radiation transfer problems: (a) domain decomposition; (b) solid-angle decomposition.

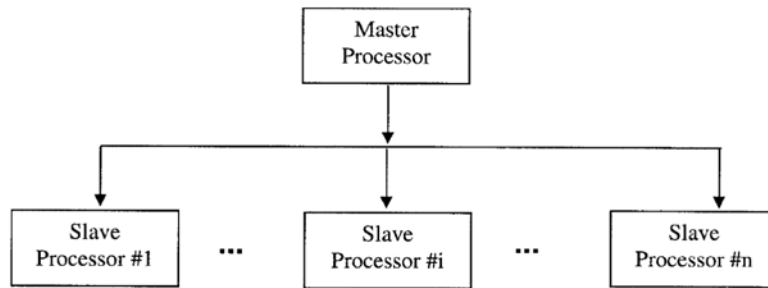


Figure 6.6 Master-slave concept used for parallel implementation of discontinuous finite element formulation for internal radiation transfer problems.

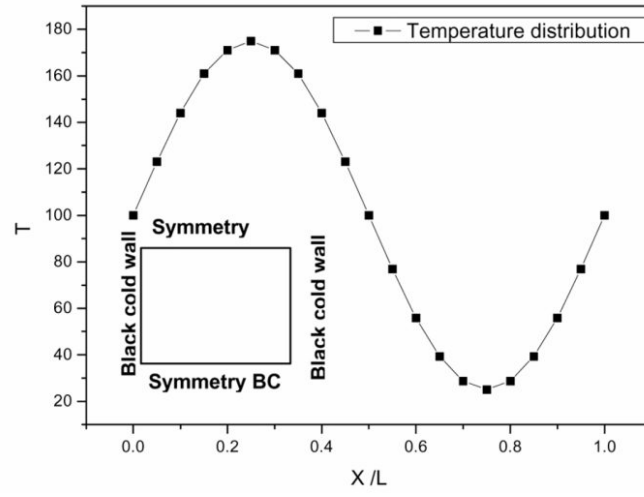
Figure 6.6 shows the parallel computing algorithm designed by following the master-slave concept common in parallel computing software development. The algorithm is based on the solid-angle partitioning strategy. Here the master processor broadcasts all data, which are required in calculating intensity of elements, to every slave processor, and receive the results calculated by every slave processor that perform the actual DFE computations in a given sub-solid-angle domain. For a given problem, the entire control angle space is divided into several subgroups based on the number of slave processors, as evenly as possible, so that each slave processor is loaded with approximately the same number of control angles for calculations. This will minimize the waiting time for any slave processors. The master processor distributes the loads among slave processors, collects the calculated data from them, calculates the heat fluxes using the data from slave processors and checks the final convergence. If the convergence is

not yet achieved, further iterations will be performed using the previous data that are redistributed by the master processor.

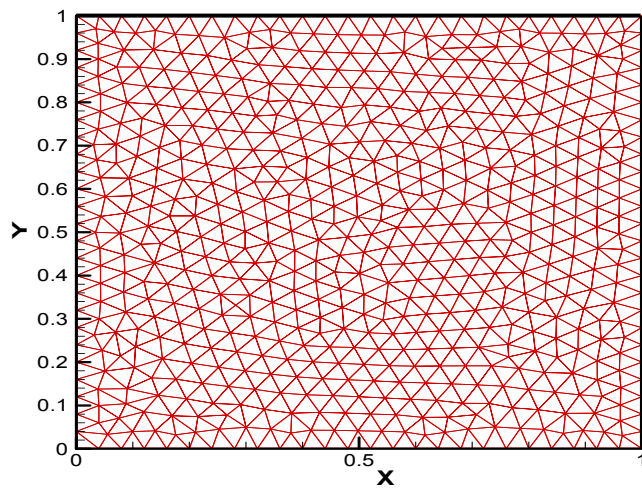
6.6 RESULTS AND DISCUSSION

In this section, the discontinuous finite element algorithm and its parallel implementation are applied to solve the problems of thermal radiation heat transfer in participating media. Both 2-D and 3-D problems are considered and whenever possible the numerical results are compared with the available analytical solutions. The calculations may use either structured or unstructured meshes, though the results using the latter are presented below. The convergence rate of the discontinuous finite element method and its parallel computational performance are also discussed. The gray participating media are used for all the cases considered here. Unless otherwise indicated, all the data are nondimensionalized.

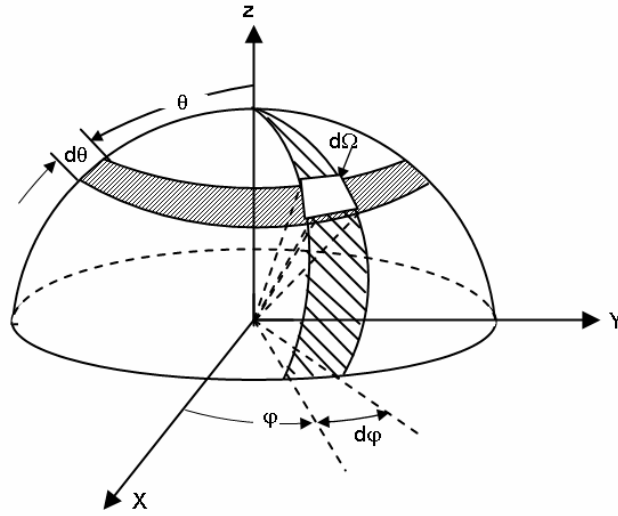
Case 1. Radiative transfer in non-scattering media



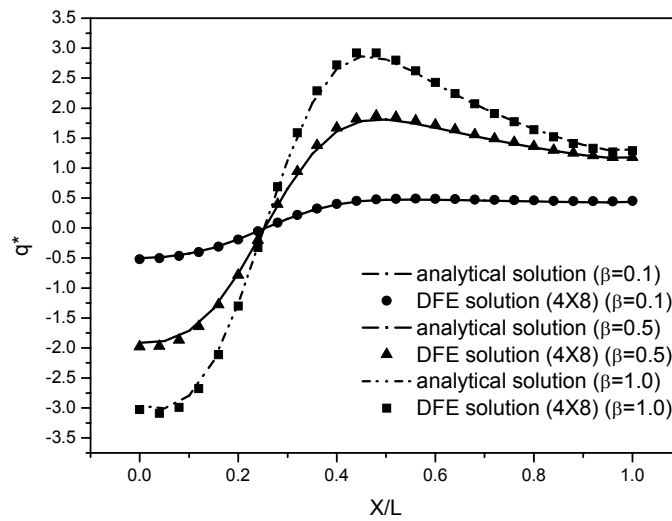
(a)



(b)



(c)



(d)

Figure 6.7. (a) Illustration of temperature distribution and boundary condition of two dimensional case. (b) Unstructured mesh for two dimensional case, which consists of 1,142 triangle elements. (c) Schematic illustration of angular space discretization. $0 \leq \theta \leq \pi$, $0 \leq \phi \leq 2\pi$, $\mathbf{s} = \sin\theta \cos\phi \hat{i} + \sin\theta \sin\phi \hat{j} + \cos\theta \hat{k}$. (d) The heat flux q_x

distribution respect to x/L obtained by DFE method is compared with analytical solution at various extinction coefficients $\beta=0.1$, $\beta=0.5$ and $\beta=1.0$.

Let us first consider a 2-D problem of internal radiative heat transfer, which is schematically illustrated in Figure 6.7(a). Here thermal radiation takes place in a square domain which is filled with an absorbing medium of $k=1.0$. The medium is non-scattering, $\sigma=0$. At $x=0$ and $x=1$ the boundaries are black cold wall, and symmetry boundary conditions are applied at $y=0$ and $y=1$. The temperature is assumed to vary from the left to the right and the variation is described by $T(x,y)=100(1+0.75\sin(2\pi x))$. Since the symmetry boundary condition is applied at the top and bottom walls, and the temperature varies only with the x coordinate, the analytical solution for the problem can be obtained by integrating the radiative transfer equation with the following result [Modest, 1993],

$$q(x) = \int_0^x I_b(x') E_2(x-x') dx' - \int_x^1 I_b(x') E_2(x'-x) dx' \quad (6.33)$$

where the $E_n(x)$ is the exponential integral function [Özisik, 1973],

$$E_n(x) = \int_0^1 \mu^{n-2} \exp\left(\frac{-x}{\mu}\right) d\mu \quad (6.34)$$

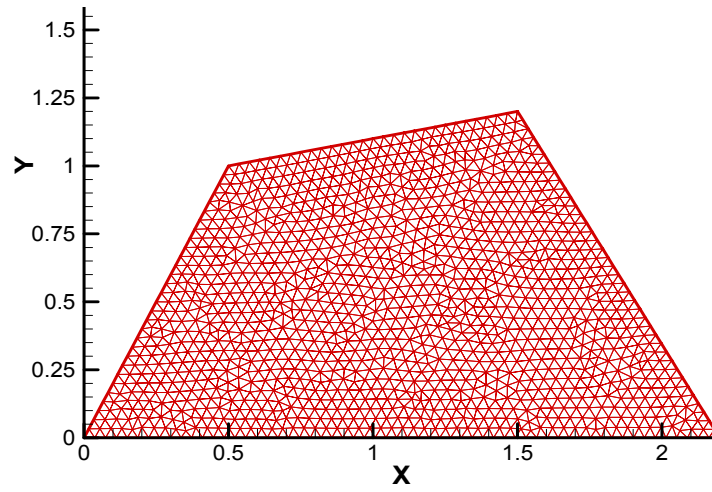
This case is solved in a 2-D unstructured triangular mesh consisting of 1,142

elements, as shown in Figure 6.7(a). The angular space is discretized into $\theta \times \phi = 2 \times 8$, that is, the angular space is divided into 2 in the azimuthal direction (θ) and 8 in the polar direction (ϕ), which is shown in Figure 6.7(c). The distribution of the nondimensionalized radiative heat flux $q_x^* = q/(\sigma T_x^4)$ at boundary $y=0.0$ is computed for various conditions and is plotted in Figure 6.7(d), along with the analytical solution and the solution obtained using the two-flux method. Apparently, excellent agreement is obtained between the analytical and the discontinuous finite element solutions for various different parameters.

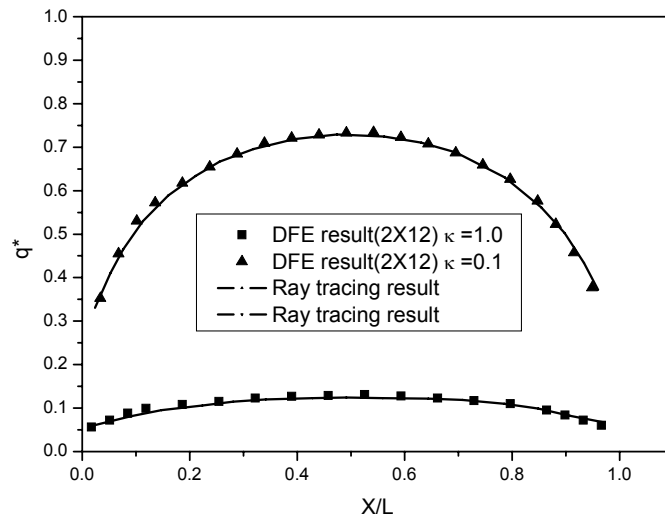
Case 2. Radiation in an irregular 2-D geometry

For this case, we consider a quadrilateral domain filled with an absorbing and emitting medium with $k=1.0$ at a constant temperature T_h . Again, the scattering effect is neglected. All boundaries are black and cold wall, the domain is defined by the vertices in anticlockwise order (0.0, 0.0), (2.2, 0.0), (1.5,1.2) and (0.5, 1.0). The calculations used an unstructured triangular mesh, as shown in Figure 6.8(a), which consists of 2473 triangular elements, and using 2×12 solid angles. The calculated heat flux along the wall $y=0.0$ is plotted in Figure 6.8(b), along with the solution obtained using the ray tracing method reported by Murthy and Mathur (1998b). From Figure 6.8(b), it is seen that the discontinuous finite element calculations are in excellent agreement with the results

obtained by the ray tracing method.



(a)



(b)

Figure 6.8. (a) Schematic illustration of unstructured mesh for 2-D irregular domain, which consists of 2473 triangle elements. (b) Comparison of heat flux on the boundary $y=0.0$ between DFE method and Ray tracing method at different absorption coefficients

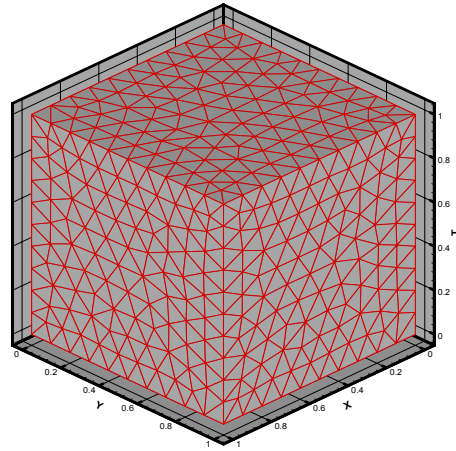
$k=0.1$ and $k=1.0$.

In this case, the physical boundary of control domain is not aligned perfectly with the global coordinate system, and hence the control angle overlap problem will occur, thereby causing error in radiation calculations if not treated [Cumber and Beeri, 1998]. This is because the integration $\int_{\Delta\Omega} (-\mathbf{n}_{w1} \cdot \mathbf{s}) d\Omega$ is not accurate when the perfect alignment between the physical and global coordinates is not the same. Chui and Raithby (1993) reported an approach to solve control angle overlap problem and Murthy and Mathur (1998b) extend the method the approach by dividing control angles to some smaller sub-control angles in their finite volume-based approaches. The basic idea is to divide the control angle into several sub-control angles, over each of which the integration is calculated and the results are then added together. This approach is also taken here and implemented in the DFE method presented, the only difference being that the nodes on the boundary are considered, instead of the boundary element as used in the finite volume method. This approach is sometimes referred to as pixlation, which gives a more accurate result for the integration $\int_{\Delta\Omega} (-\mathbf{n}_{w1} \cdot \mathbf{s}) d\Omega$.

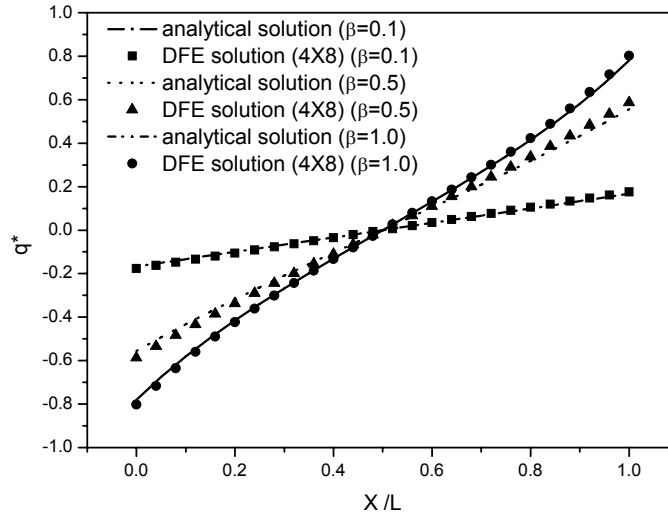
Case 3. Radiation in 3-D geometry

Here, a cube with a dimension of $1 \times 1 \times 1$ is chosen. It is discretized into 2,313 unstructured tetrahedral elements, as shown in figure 6.9(a). The control angles used in

this problem is 4×8 , and the temperature of medium is set at $T_h = \text{constant}$. In order to compare the accuracy of DFE method in 3-D calculation, the following boundary conditions are specified in this problem so that analytical solution can be obtained for comparison. In this problem, the top and bottom surfaces are set to black and cold wall, but all four lateral surfaces are applied with symmetry boundary condition. As we did in the two dimensional case, the analytical solution of this case is also derived by integrating RTE equation, and has the same expression as Eq. (6.30). From Figure 6.9b, it is clear that the DFE method gives good results compared with analytical solutions for a wide range of k values.



(a)



(b)

Figure 6.9. (a) Schematic illustration of unstructured mesh for the 3-D case, which consists of 2313 unstructured tetrahedral elements. The temperature of media T is constant and all walls are black and cold. (b) Comparison of heat flux q_z^* respect to x/L at middle line of top surface $y/L=0.5$, and $z/L=1.0$. The extinction coefficient varies from $\beta=0.1$ nd $\beta=1.0$.

Case 4. Scattering in 3-D geometry

If some particles exist in media, the scattering effect must be considered, because the particles scatter the radiation of a given direction into all other directions. Also, the radiation in other directions is scattered into the given direction in a scattering medium. Scattering effects are usually classified into isotropic scattering and anisotropic scattering.

The former scatters energy to all other directions with the same energy distribution, whereas anisotropic scattering scatters radiation energy to different directions with various energy distributions. The isotropic scattering function is simple and easy to calculate by Eq. (6.35),

$$\Phi(\mathbf{s}, \mathbf{s}') = 1 \quad (6.35)$$

Anisotropic scattering is more complex and certainly needs more calculation time since the scattering function is direction dependent, and every direction needs to be calculated. There are two different models being used for anisotropic scattering functions, this is, forward scattering and backward scattering. The forward scattering means more energy is scattered into the forward directions than the backward directions. The backward scattering means just opposite, that is, more energy is scattered into backward direction. The scattering functions, either forward or backward, may be described by the following generic expression,

$$\Phi(s, s') = \sum_{j=1}^{N_s} c_j P_j(\cos \varpi) \quad (6.36)$$

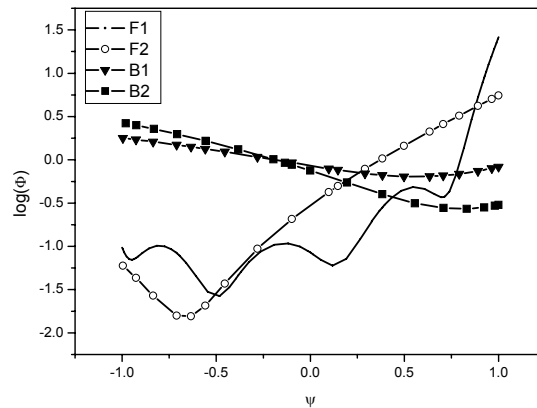
where ϖ is calculated by

$$\varpi = \cos \theta \cos \theta' + (1 - \cos^2 \theta)(1 - \cos^2 \theta')^{1/2} \cos(\phi' - \phi) \quad (6.37)$$

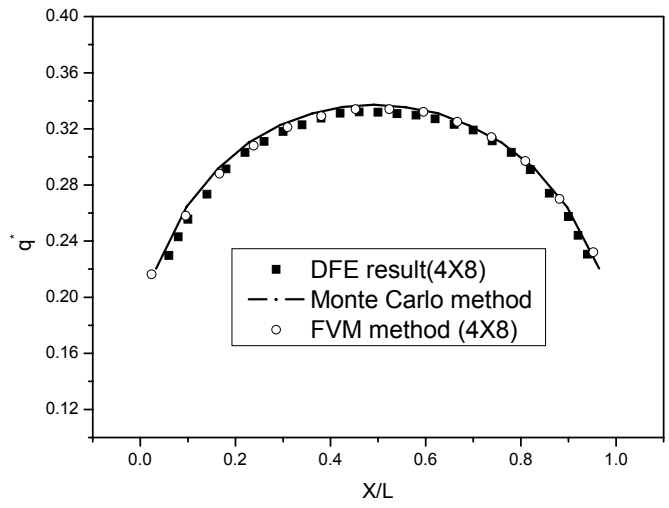
j	F1	F2	B1	B2
0	1	1	1	1
1	2.53602	2.00917	-0.5652	-1.2
2	3.56549	1.56339	0.29783	0.5
3	3.97976	0.67407	0.08571	
4	4.00292	0.22215	0.01003	
5	3.66401	0.04725	0.00063	
6	3.01601	0.00671		
7	2.23304	0.00068		
8	1.30251	0.00005		
9	0.53463			
10	0.20136			
11	0.0548			
12	0.01099			

Table 6.1 the expansion coefficients for the phase functions

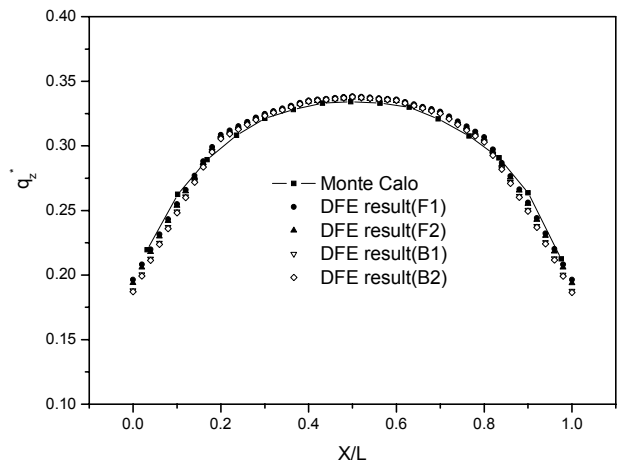
For the calculations given here, the values of coefficient C_j in Eq(6.37) are taken from Kim and Lee's work (1998), who gave the coefficients of polynomial for different models by slightly modifying Mie coefficients [Wiscombe, 1980]. The four different scattering functions are depicted in Figure 6.10(a).



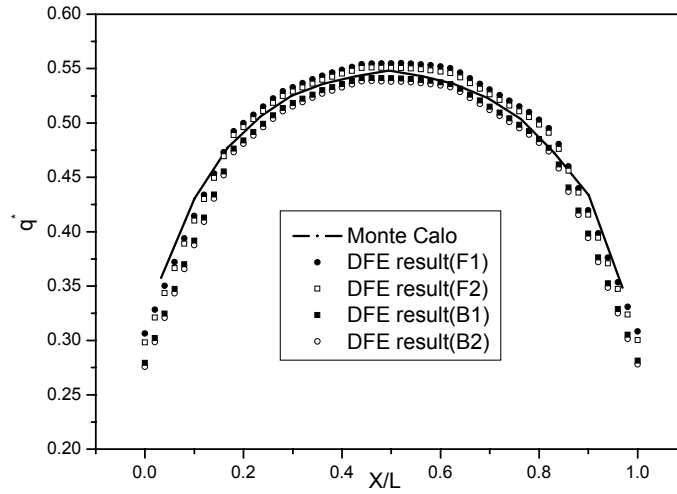
(a)



(b)



(c)



(d)

Figure 6.10 (a) Illustration of scattering functions of different models. (b) Comparison of heat flux q_z^* distribution on the top surface of cube $y/L=0.5$, and $z/L=1.0$ with isotropic scattering between DFE, FVM and Monte Carlo method. The scattering coefficient is 0.5. (c) Comparison of heat flux q_z^* distribution on the top surface of cube $y/L=0.5$, and $z/L=1.0$ with anisotropic scattering between DFE and Monte Carlo method. The different scattering functions are chosen and extinction coefficient is 1.0. (d) Comparison of heat flux q_z^* distribution on the top surface of cube $y/L=0.5$, and $z/L=1.0$ with anisotropic scattering between DFE and Monte Carlo method. The different scattering functions are chosen and extinction coefficient is 2.0.

Eqs. (6.36) and (6.37) describe the dependence of the scattering function on the

directions for anisotropic scattering phenomena. In calculations, the angular space is discretized into finite number of control angles. Often an averaged scattering function over a discretized control angle is used [Chui and Raithby, 1993]. While the scattering function at the axis direction of control angle may be used as average scattering function, a better approach is to average the scattering function over each control angle using the following expression [Chai and Partankar, 2000],

$$\Phi(\mathbf{s}, \mathbf{s}') = \frac{\int_{\Delta\Omega} \int_{\Delta\Omega'} \Phi(\mathbf{s}, \mathbf{s}') d\Omega d\Omega'}{\int_{\Delta\Omega} \int_{\Delta\Omega'} d\Omega d\Omega'} \quad (6.38)$$

The above procedure and scattering functions can be readily incorporated into the discontinuous finite element formulation. The calculated results for isotropic scattering are shown in Figures 6.10b to 6.10c and those for anisotropic scattering are given in Figures 6.10d. The same unstructured mesh as in Case 3 is used for these computations. The present calculations are also compared with those obtained using the Monte Carlo method and the finite volume method. The comparison between the DFE results and those reported is gratifying, suggesting that the DFE method is useful for the radiative heat transfer calculations.

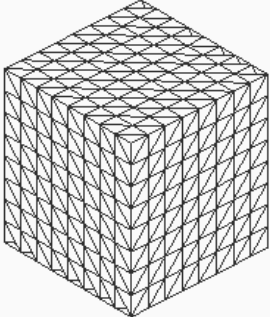
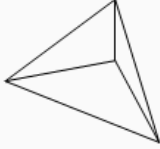
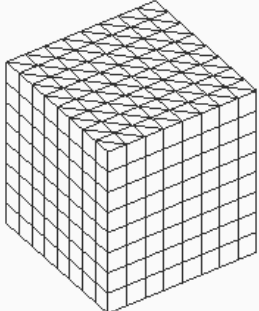
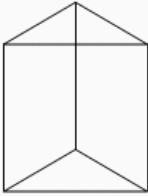
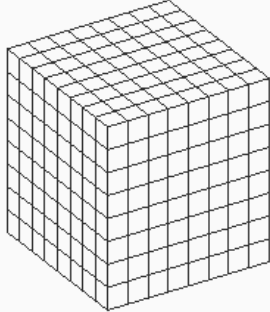
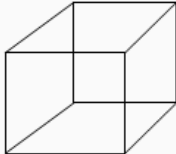
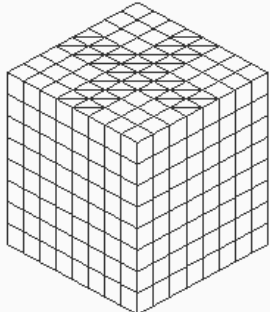
Case 4. Mixed mesh for 3-D geometry

In this case we consider a cube enclosure filled with a purely emitting and absorbing medium. The cube has a length $L=1$. The control angles used in this problem are 4×8 , that is, the angular space is divided into 4 in the azimuthal direction (θ) and 8 in the polar direction (φ). The temperature of medium is set at $T_{ref} = \text{constant}$, and all the boundaries of enclosure are black ($\varepsilon = 1$) and cold ($T_w = 0$). The cube is discretized into three different types of elements, as shown in Fig. 6.11(a) (the cube is discretized into 3072 tetrahedral elements, 1024 wedge elements and 512 hexahedral elements or 736 mixed elements including hexahedral and wedge elements).

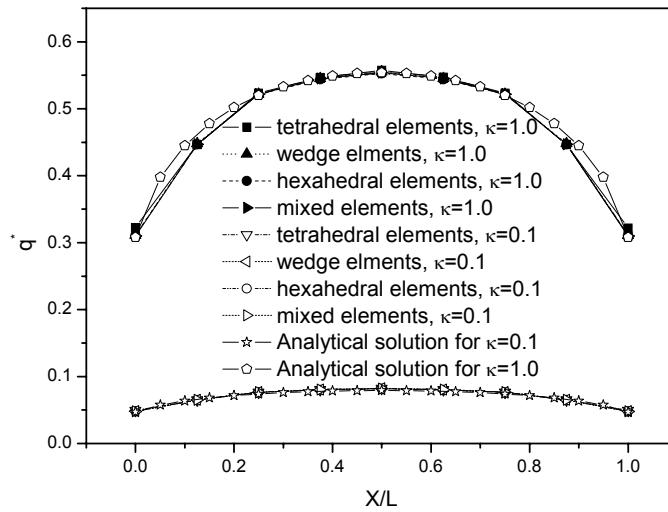
The radiative heat flux along the center line on the top surface ($y/L=0.5, z/L=1.0$) can be obtained by using three different types of elements respectively, as shown in Fig. 6.11(b). In Fig. 6.11(b), the radiative heat flux is calculated with $\kappa = 0.1$ and $\kappa = 1.0$, and the results of three different types of elements agree very well with analytical solutions.

In order to show the accuracy of the DFE method, we compared the results of DFE method and finite volume method, which is one of widely used method. For comparison, the same mesh with 512 hexahedral elements and same angular space discretization (4×8) are used. The radiative heat flux along the center line ($y=0.5, z=1.0$) is plotted in Fig. 6.11(c) $\kappa = 10.0$. Examination of the results shows that the DFE gives a better accuracy than the finite method when the same discretizations are used. This is also observed for other cases with different κ values.

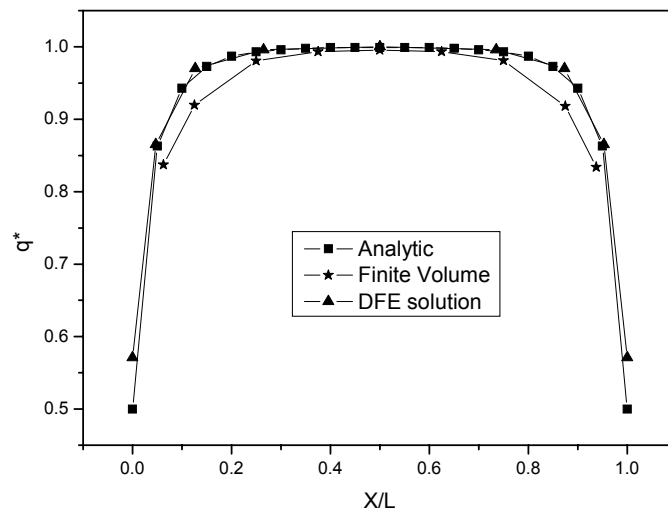
For convenience the radiative heat flux in this chapter is non-dimensionalized as $q^* = \frac{q_r}{\sigma T_{ref}^4}$. Numerical experiments show that more accurate results are obtained with a finer discretization, as expected. For the same number of elements, the DFE method in the present implementation requires roughly the same CPU time and the same number of iterations as the finite volume method. If numerical integration is used in the element calculations, the CPU time is expected to increase. However, our experiences further show that for the same accuracy, the DFE requires fewer elements, which would actually result in a shorter CPU time.

	 <p>tetrahedral element</p>
	 <p>wedge element</p>
	 <p>hexahedral element</p>
	<p>mixed mesh formed by Hexahedral and wedge elements</p>

(a)



(b)



(c)

Figure 6.11 3-D discretization and calculated radiative heat flux q^* along the middle line of top surface $y/L=0.5$, and $z/L=1.0$. (a) The cube is discretized with 3072 tetrahedral elements, or 1024 wedge elements, or 512 hexahedral elements or 736 elements of mixed

hexahedra and pentahedra. (b) Comparison of radiative heat fluxes calculated using different meshes shown in (a). The absorption coefficient varies from $\kappa = 0.1$ to $\kappa = 1.0$. (c) Comparison of the DFE and the Finite Volume methods for the solution of RTE for $\kappa = 10$.

Performance of parallel computation

From all three cases, the DFE shows it is powerful and easy to apply method. As mentioned earlier, for three-dimensional problem, the computation is very time consuming, and thus the parallel algorithm can be used to facilitate the computations. Below, we briefly discuss the performance of parallel algorithm implemented as discussed in the last section.

One three-dimensional case and one two-dimensional case are used to test the parallel algorithm. The three-dimensional problem is as same as described above, which is concerned with the radiative transfer in a $1 \times 1 \times 1$ cube discretized into 2,313 unstructured tetrahedral elements. The two-dimensional problem is as same as in Case 2 above, which is 1×1 square with black and cold walls. For both cases, the control angle is discretized into 2×24 and the medium is $\kappa = 1.0$. All the computations were done on a Compaq GS80 UNIX platform, which has 8 alpha microprocessors with 8 GB Ram, capable of high performance parallel computing. The CPU time for different number of

CPUs used in parallel computations is shown in Figure 6.12. Clearly, the more numbers of CPUs are used, the less time is required for computation. But if the time for every CPU is added together, the total time for computation is almost the same as for a single CPU, indicating that there is a very little overhead. These results show that the present parallel algorithm gives almost an idealized parallel performance one can ever hope for,

$$T_{parallel} = \frac{T_1}{N_{cpu}} \quad (6.39)$$

that is, the time by each CPU equals the time by using 1 CPU divided by N. This means that the intercommunication between the processors is minimized to a negligible level. In the cases studied here, the results agree very well with Eq. (6.41). This is attributed to the fact that on angular space partition the load of different CPU is distributed rather evenly. It is noted here that the above results are encouraging but some preliminary as only very few processors are used for the purpose of testing the parallel algorithm. A more detailed study using massive parallel processors is apparently needed to verify the above results. Nonetheless, the ease with which the parallel algorithm can be incorporated into the discontinuous finite element formulation is clearly demonstrated through these examples.

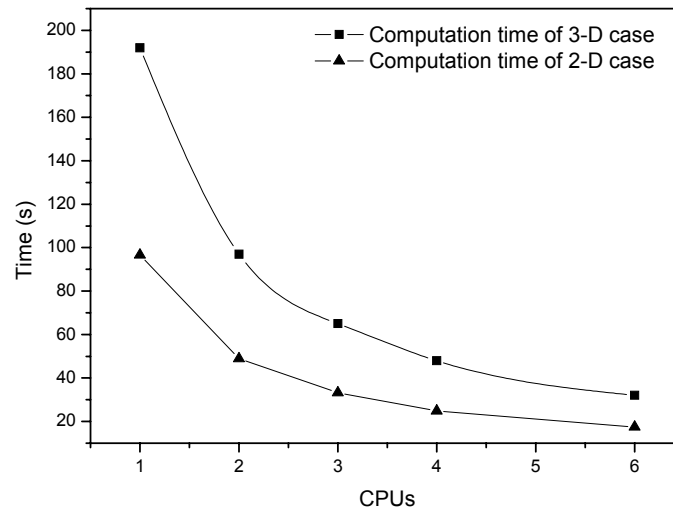


Figure 6.12 The CPU time respect to the number of CPUs in parallel computation.

CHAPTER 7

A DISCONTINUOUS FINITE ELEMENT FORMULATION FOR RADIATIVE TRANSFER IN AXISYMMETRIC FINITE CYLINDRICAL ENCLOSURES AND COUPLING WITH OTHER MODE HEAT TRANSFER

7.1 INTRODUCTION

In chapter 5 and Chapter 6, we discussed radiative heat transfer in 2-D and 3-D dimensional enclosure. But radiative heat transfer occurs in engineering thermal systems such as furnaces, combustion chambers, boilers, gas turbines and optical crystal growth furnaces, many of which can be considered as finite-length cylindrical enclosures. Under practical conditions, an axisymmetric approximation often may be made to predict the thermal performance of these cylindrical systems. An important implication of this approximation is that the axisymmetric and periodic conditions associated with these systems can be applied and thus fully three-dimensional calculations may be replaced by the corresponding two-dimensional calculations, thereby resulting in savings in both computational cost and storage requirement.

The main objective of this study is to present a discontinuous finite element computational methodology for solving the radiative transfer equation in axisymmetric, finite length cylindrical enclosures. This is intended to be complementary to the 1-D, 2-D

and 3-D DFE formulations discussed in previous chapters. An axisymmetric radiative transfer equation is essentially three-dimensional when written in cylindrical coordinates and hence can be solved directly using the 3-D formulation [Cui and li, 2004b]. However, as shown below, a DFE formulation, combined with the azimuthal mapping method [Chui and Raithby, 1992; Fernandes and Francis, 1982], can be applied to compute the radiative transfer in axisymmetric enclosures over a 2-D mesh only. The success of the mapping method has been demonstrated in the framework of the finite volume method [Chui and Raithby, 1992]. However, an integration of the mapping into the DFE formulation for axisymmetric radiative heat transfer does not appear to have yet been considered elsewhere. In what follows, mathematical formulations and numerical procedures are given. Both unstructured and structured meshes are used for computations to demonstrate the flexibility of the method. The coupling of the DFE method with the existing finite element method for the fluid flow and heat transfer calculations is also discussed. Case studies including absorbing, emitting and scattering media are presented and results are compared with those reported in the literature using other methods whenever available. An example is also included to illustrate the coupling of semi-transparent melt flows and radiative heat transfer in a cylinder under slow rotation, with flow driven by a combined action of surface tension and buoyancy forces.

7.2 INTERNAL RADIATION HEAT TRANSFER

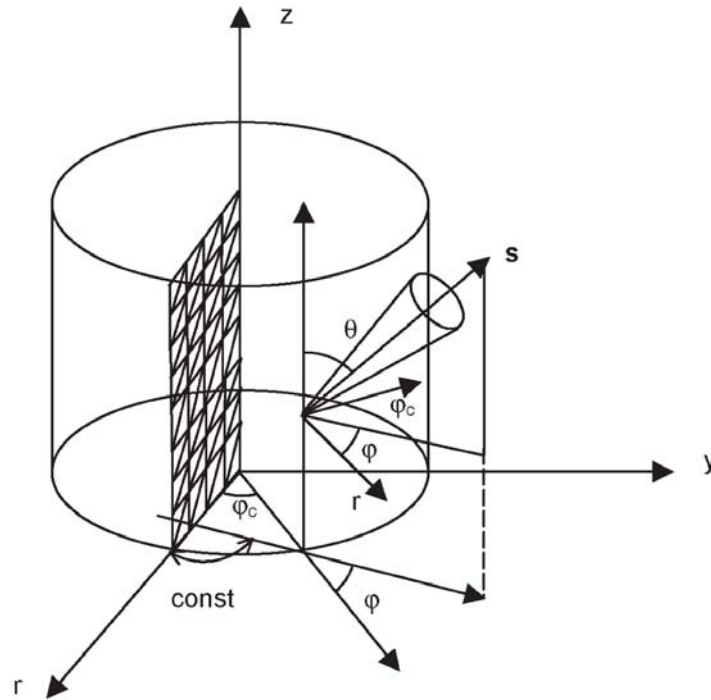


Figure 7.1. Radiative transfer in axisymmetric geometry and the cylindrical coordinate system used for numerical analysis.

For radiative transfer in axisymmetric cylindrical enclosures, the temperature and radiative properties vary only in the r and z directions, but not in the azimuthal direction φ_c . Here, φ_c is the azimuthal angle in the cylindrical coordinate system and independent of azimuthal direction angle φ . With the coordinate system shown in Figure 7.1, the radiative transfer equation can be written as

$$\begin{aligned}
\mathbf{s} \cdot \nabla I(\mathbf{r}, \mathbf{s}) &= \sin \theta \cos \varphi \frac{\partial I(r, z; \mathbf{s})}{\partial r} - \frac{\sin \theta \sin \varphi}{r} \frac{\partial I(r, z; \mathbf{s})}{\partial \varphi} + \cos \theta \frac{\partial I(r, z; \mathbf{s})}{\partial z} \\
&= -\beta(\mathbf{r})I(\mathbf{r}, \mathbf{s}) + \kappa(\mathbf{r})I_b(\mathbf{r}) + \frac{\sigma(\mathbf{r})}{4\pi} \int_{4\pi} I(\mathbf{r}, \mathbf{s}') \Phi(\mathbf{s}, \mathbf{s}') d\Omega'
\end{aligned} \tag{7.1}$$

where θ is the polar direction of radiation intensity. From the geometric relation shown in Figure 7.1, it is clear that $\varphi_c + \varphi = \text{constant}$ along \mathbf{s} . It is important to note here that for an axisymmetric problem, the radiation intensity also depends on the polar (i.e. φ) direction. However, as shown below, the axisymmetry and periodic conditions intrinsic within an axisymmetric problem may be used to map the quantities at any φ_c using the data at $\varphi_c=0$, thereby making the calculations possible over a 2-D mesh.

To solve the governing equation given by Eq. (7.1), boundary conditions are required. For an opaque diffuse surface the thermal balance gives the following equation:

$$I(\mathbf{r}, \mathbf{s}) = \varepsilon(\mathbf{r})I_b(\mathbf{r}) + \frac{1 - \varepsilon(\mathbf{r})}{\pi} \int_{\mathbf{s}' \cdot \mathbf{n}_w < 0} I(\mathbf{r}, \mathbf{s}') |\mathbf{s}' \cdot \mathbf{n}_w| d\Omega' \tag{7.2}$$

Symmetry boundary conditions are also used in the computations and are given below [Moder *et al.*, 2000]

$$\begin{cases} I(\mathbf{r}, \mathbf{s}) = I(\mathbf{r}, \mathbf{s}^*) \\ \mathbf{n} \cdot \mathbf{s} = -\mathbf{n} \cdot \mathbf{s}^* \\ \mathbf{s} \times \mathbf{s}^* \cdot \mathbf{n} = 0 \end{cases} \tag{7.3}$$

where the \mathbf{s}^* is the symmetric radiation direction of \mathbf{s} with respect to the tangent of the boundary, with both \mathbf{s} and \mathbf{s}^* lying on the plane of $\mathbf{t} - \mathbf{n}$ (see Figure 2.5).

For the axisymmetric problems under discussion, periodical boundary conditions also exist. Referring to Figure 7.1(c), point \mathbf{r} can be rotated from point \mathbf{r}' around point o , viz.,

$$\mathbf{r} = [\mathbf{R}]\mathbf{r}' \quad (7.4)$$

where $[\mathbf{R}]$ is the rotation matrix. The normals of two boundaries \mathbf{n} and \mathbf{n}' , and the directions \mathbf{s} and \mathbf{s}' at which the intensities emit from the boundaries also have the following relations [8],

$$\mathbf{n} = [\mathbf{R}]\mathbf{n}' \quad (7.5)$$

$$\mathbf{s} = [\mathbf{R}]\mathbf{s}' \quad (7.6)$$

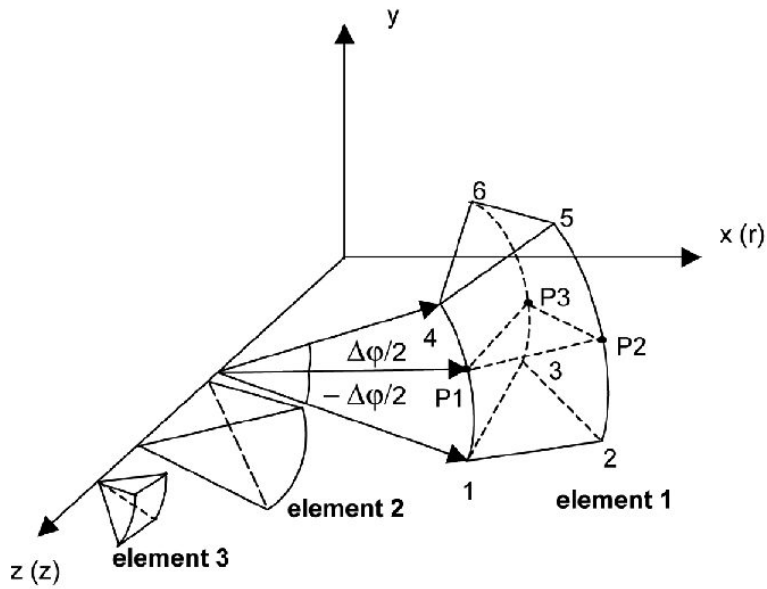
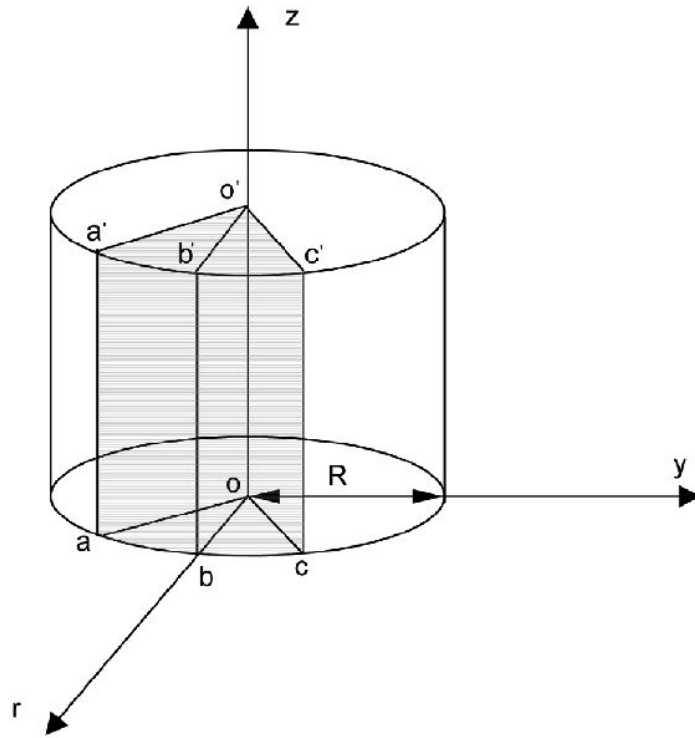
As a result, the intensities in the directions \mathbf{s} and \mathbf{s}' are equal,

$$I(\mathbf{s}) = I(\mathbf{s}') \quad (7.9)$$

7.3 THE DISCONTINUOUS FINITE ELEMENT FORMULATION

Here, we intend to develop a discontinuous finite element formulation for the axisymmetric problem on a two-dimensional mesh defined on the r - z plane, as shown in Figure 7.1. Strictly speaking, the solution of the problem defined by Eq. (7.1) requires the use of a three-dimensional domain, which for the present case is generated by rotating the two-dimensional mesh on the r - z plane with a prescribed angle $\pm \Delta\varphi/2$ along the azimuthal direction. In this sense, the 2-D mesh serves as the generating plane for the 3-D

mesh. Thus, a three-dimensional slice is formed by the two planes $aa'o'o$ and $cc'o'o$ passing through the axis of symmetry. A third plane, $boo'b'$, that is, the r - z plane, bisects the angle formed between the planes $abco$ and $a'b'c'o'$. The arrangement of these planes is given in Figure 7.2a. As a result of rotation, a 2-D mesh is mapped into a 3-D mesh consisting of 6-node pentahedra, 5-node polyhedra, and 4-node tetrahedra. The pentahedra are generated by rotating the corresponding triangular elements, lying outside the z -axis, of the two-dimensional mesh on the r - z plane. The triangular generating elements with one side lying along the $r=0$ axis give rise to 4-node tetrahedra. The elements with one node lying on the $r=0$ axis give 5-node polyhedra. The elements 1, 2 and 3, as shown in Figure 7.2b are the pentahedon, tetrahedron and polyhedron generated as described above.



(b)

Figure 7.2 Domain and element types used for axisymmetric radiative transfer calculations: (a) the 3-D domain generated by the rotation of the axisymmetry plane and

(b) three types of 3-D elements used for the discontinuous finite element formulation.

Because of the term $\partial I / \partial \varphi = -\partial I / \partial \varphi_c$, we consider the integration over a volume element (a pentahedron, a tetrahedron or a polyhedron), as shown in Figure 7.2b. Integrating Eq. (7.1) over the volume element and the solid angle $\Delta\Omega_l$ with respect to a weighting function $v(\mathbf{r}, \Omega)$, we have

$$\int_{V_e} v(\mathbf{r}, \Omega) \int_{\Delta\Omega_l} \mathbf{s} \cdot \nabla I d\Omega dV = \int_{V_e} v(\mathbf{r}, \Omega) \int_{\Delta\Omega_l} (-\beta(\mathbf{r})I(\mathbf{r}, \mathbf{s}) + S(\mathbf{r}, \mathbf{s})) d\Omega dV \quad (7.10)$$

where V_e is the volume of the element under consideration (i.e. the i th element), and $S(\mathbf{r}, \mathbf{s})$ is the source function defined as

$$S(\mathbf{r}, \mathbf{s}) = \kappa(\mathbf{r})I_b(\mathbf{r}) + \frac{\sigma(\mathbf{r})}{4\pi} \int_{4\pi} I(\mathbf{r}, \mathbf{s}')\Phi(\mathbf{s}, \mathbf{s}')d\Omega' \quad (7.11)$$

Applying integration by parts once to Eq. (7.10), we have,

$$\begin{aligned} & \int_{V_e} \int_{\Delta\Omega_l} -I\mathbf{s} \cdot \nabla v(\mathbf{r}, \Omega) d\Omega dV + \int_{\Delta\Omega_l} \int_{\Gamma} v(\mathbf{r}, \Omega) I^+ \mathbf{n} \cdot \mathbf{s} d\Gamma d\Omega \\ & = \int_{V_e} v(\mathbf{r}, \Omega) \int_{\Delta\Omega_l} (-\beta(\mathbf{r})I(\mathbf{r}, \mathbf{s}) + S(\mathbf{r}, \mathbf{s})) d\Omega dV \end{aligned} \quad (7.12)$$

where the superscript + means taking the value outside the element boundary. Applying integration-by-parts again to Eq. (7.12) yields the following expression:

$$\begin{aligned}
& \int_{V_e} \int_{\Delta\Omega_l} v(\mathbf{r}, \Omega) \mathbf{s} \cdot \nabla I d\Omega dV + \int_{\Gamma} \int_{\Delta\Omega_l} v(\mathbf{r}, \Omega) [I] \mathbf{n} \cdot \mathbf{s} d\Omega d\Gamma \\
& = \int_{V_e} v(\mathbf{r}, \Omega) \int_{\Delta\Omega_l} (-\beta(\mathbf{r}) I(\mathbf{r}, \mathbf{s}) + S(\mathbf{r}, \mathbf{s})) d\Omega dV
\end{aligned} \tag{7.13}$$

where \mathbf{n} is the outnormal of the element boundary and use has been made of the divergence theorem,

$$\mathbf{s} \cdot \int_{\Gamma} \phi I \mathbf{n} dA - \mathbf{s} \cdot \int_{V_e} I \nabla \phi dV = \mathbf{s} \cdot \int_{V_e} \phi \nabla I dV \tag{7.14}$$

to convert the domain integral into the boundary integral in both Eqs. (7.13) and (7.14). Here, in order to apply the divergence theorem, we have used the definition, $dV = rd\varphi_c dr dz$. Note that in the conventional finite element formulation, the terms on the element boundary disappear when they are combined with neighboring elements or $[I] = 0$. In the discontinuous formulation, however, these terms do not cancel when elements are assembled. Instead, the following limiting values are used:

$$I_j^+ = \lim_{\mathbf{r}_j \rightarrow \Gamma^+} I(\mathbf{r}_j) \quad \text{and} \quad I_j^- = \lim_{\mathbf{r}_j \rightarrow \Gamma^-} I(\mathbf{r}_j) \tag{7.15}$$

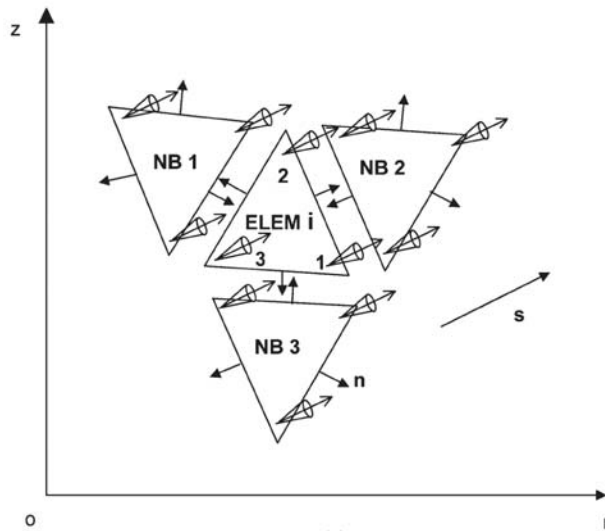
where the superscripts + and – denote the front side and back side of the normal vector, respectively. By this convention, the values denoted by superscript “-” are *inside* the element and those by “+” are *outside* the element (see Figure 7.3a). This definition is slightly different from the one-D case [Cui and Li, 2004a] but the essential idea is the same. The above treatment assumes that the two values I_j^+ and I_j^- across the element

boundaries are not the same, and these jumps are often denoted by,

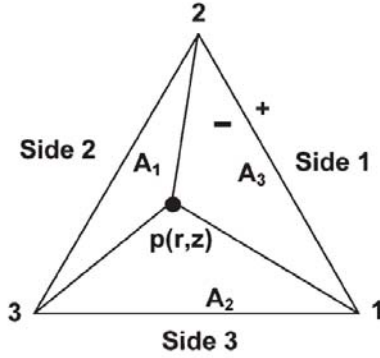
$$[I]_j = I_j^+ - I_j^- \quad (7.16)$$

These jumps may also be modeled by the generic numerical fluxes that are single-valued at the boundaries and are a function of field values across the inter-element boundaries [Cui and Li, 2004a, b]. For the problems under consideration, the simplest and effective treatment of the jump condition is by using the upwinding procedure, which in the discontinuous finite element literature is sometimes referred to as the inflow boundary value,

$$[I]_j = \begin{cases} [I]_j & \text{if } \mathbf{n} \cdot \mathbf{s} < 0 \\ 0 & \text{if } \mathbf{n} \cdot \mathbf{s} > 0 \end{cases} \quad (7.17)$$



(a)



(b)

Figure 7.3. (a) Schematic illustration of the mesh of DFE formulation for radiation in absorbing and emitting media. (b) Local node number and side number of a typical triangular element used for discontinuous finite element formulation of internal radiation transfer problems

Appropriate interpolation functions now may be chosen from the finite element broken space that does not demand continuity across the inter-element boundaries. A natural choice of shape functions for internal radiation applications is made by taking a step function for the solid angle and a polynomial function for the spatial variation, $v(\Omega, x) = \psi(\Delta\Omega_i)\phi(x)$. Here $\psi(\Delta\Omega_i)$ is the step function of the solid angle differential centered at Ω_i and $\phi(x)$ is the shape function of the spatial coordinates. Substituting this testing function into the integral expression and re-arranging, one has the following relation:

$$\begin{aligned}
& \int_{\Delta\Omega_l} \mathbf{s} \cdot \int_{V_e} \phi \nabla I(\mathbf{r}, \mathbf{s}) dV d\Omega + \int_{\Delta\Omega_l} \int_{\Gamma} \phi [I] \mathbf{n} \cdot \mathbf{s} d\Gamma d\Omega \\
& = \int_{\Delta\Omega_l} \int_{V_e} [-\beta(\mathbf{r}) \phi I(\mathbf{r}, \mathbf{s}) + \phi S(\mathbf{r}, \mathbf{s})] dV d\Omega
\end{aligned} \tag{7.18}$$

which is the final form of the integral presentation of the radiative transfer equation. It is noted that Eq. (7.18) reduces to the finite volume formulation if a constant shape function $\phi(\mathbf{r})$ is used, and to the finite element formulation when $[I] = 0$ across the element interface is enforced. From this perspective, Eq. (7.18) represents a general integral formulation for all these integral-based methods.

Because the step function is used to approximate the solid angle, the surface integration term can be separated into terms involving the surfaces perpendicular to the axisymmetry plane and into terms along the φ_c direction,

$$\int_{\Delta\Omega_l} \int_{\Gamma} \phi [I] \mathbf{n} \cdot \mathbf{s} d\Gamma d\Omega = \int_{\Delta\Omega_l} \int_{\Gamma_p} \phi [I] \mathbf{n} \cdot \mathbf{s} d\Gamma d\Omega + \int_{\Delta\Omega_l} \int_{\Gamma_\varphi} \phi [I] \mathbf{n} \cdot \mathbf{s} d\Gamma d\Omega \tag{7.19}$$

Note that the surface Γ_φ is obtained by simply rotating the 2-D element, such as the top surface (surface 4-5-6, at $\varphi_c = \Delta\varphi/2$ and bottom surface (surface 3-2-1, at $\varphi_c = -\Delta\varphi/2$) as appears in Figure 7.3b. Γ_p is the lateral surface such as the surfaces 1-2-5-4, 2-3-6-5, 3-1-4-6 in Figure 3b. The integration over the surface Γ_φ requires the use of the axisymmetry and periodic conditions. The numerical implementation of the above integral formulation is given below.

7.4. NUMERICAL IMPLEMENTATION

Let us consider a typical element, that is, the i th triangular element and its neighbors, as shown in Figure 7.3a. Remember that this 2-D triangular element generates a corresponding 3-D element by rotating around the z -axis by a prescribed angle. For the sake of discussion, the inter-element boundaries are plotted separately. The nodal values of the variable are defined within the element, to conform to the rule of selecting interpolation functions from the finite element broken space. Because the discontinuity is allowed across the element boundaries in the discontinuous formulation, the common geometric node does not have the same field variable value. This is a crucial difference between the conventional and the discontinuous finite element formulations.

For a 2-D linear triangular element located on the r - z plane, the shape functions may be constructed as follows:

$$\begin{bmatrix} \phi_1 \\ \phi_2 \\ \phi_3 \end{bmatrix} = \frac{1}{2A_e} \begin{bmatrix} M_{23} & -Z_{23} & R_{23} \\ M_{31} & -Z_{31} & R_{31} \\ M_{12} & -Z_{12} & R_{12} \end{bmatrix} \begin{bmatrix} 1 \\ z \\ r \end{bmatrix} \quad (7.20)$$

where A_e is the triangular area on the r - z plane and the elements of the matrix in Eq.

(7.20) are calculated by,

$$M_{ij} = \begin{vmatrix} z_i & z_j \\ r_i & r_j \end{vmatrix}, \quad R_{ij} = \begin{vmatrix} 1 & 1 \\ r_i & r_j \end{vmatrix}, \quad Z_{ij} = \begin{vmatrix} 1 & 1 \\ z_i & z_j \end{vmatrix} \quad (7.21)$$

The radiation intensity inside the element is interpolated using the above shape functions,

$$I(z, r; \mathbf{s}) = I_1(\mathbf{s})\phi_1(z, r) + I_2(\mathbf{s})\phi_2(z, r) + I_3(\mathbf{s})\phi_3(z, r) \quad (7.22)$$

Substituting the above equation into Eq. (7.18), and noticing that the intensity with control angles is constant due to a step function approximation, one obtains the following expression:

$$\begin{aligned} & \int_{\Delta\Omega_i} \mathbf{s} \cdot \int_{V_e} \begin{bmatrix} \phi_1 \\ \phi_2 \\ \phi_3 \end{bmatrix} [\nabla\phi_1, \nabla\phi_2, \nabla\phi_3] \begin{bmatrix} I_1 \\ I_2 \\ I_3 \end{bmatrix} dV d\Omega + \int_{\Delta\Omega_i} \int_{\Gamma_p} \begin{bmatrix} \phi_1 \\ \phi_2 \\ \phi_3 \end{bmatrix} [\phi_1 \quad \phi_2 \quad \phi_3] \begin{bmatrix} [I]_1 \\ [I]_2 \\ [I]_3 \end{bmatrix} (\mathbf{n} \cdot \mathbf{s}) d\Gamma d\Omega \\ & + \int_{\Delta\Omega_i} \int_{\Gamma_\varphi} \begin{bmatrix} \phi_1 \\ \phi_2 \\ \phi_3 \end{bmatrix} [\phi_1 \quad \phi_2 \quad \phi_3] \begin{bmatrix} [I]_1 \\ [I]_2 \\ [I]_3 \end{bmatrix} (\mathbf{n} \cdot \mathbf{s}) d\Gamma d\Omega \\ & = \int_{\Delta\Omega_i} \int_{V_e} \left\{ -\beta(\mathbf{r}) \begin{bmatrix} \phi_1 \\ \phi_2 \\ \phi_3 \end{bmatrix} [\phi_1, \phi_2, \phi_3] \begin{bmatrix} I_1 \\ I_2 \\ I_3 \end{bmatrix} + \begin{bmatrix} \phi_1 \\ \phi_2 \\ \phi_3 \end{bmatrix} S(\mathbf{r}, \mathbf{s}) \right\} dV d\Omega \end{aligned} \quad (7.23)$$

Volume integration

Let us consider the first term in Eq. (7.18), which involves the volume integration over a 3-D element generated by the i th triangular element. Taking the derivative of the shape functions,

$$\begin{bmatrix} \nabla \phi_1 \\ \nabla \phi_2 \\ \nabla \phi_3 \end{bmatrix} = \frac{1}{2A_e} \begin{bmatrix} -Z_{23} & R_{23} \\ -Z_{31} & R_{31} \\ -Z_{12} & R_{12} \end{bmatrix} \begin{bmatrix} \hat{k} \\ \hat{r} \end{bmatrix} \quad (7.24)$$

and noticing that $\nabla \phi_i$ ($i=1,2,3$) is independent of the area integral, one has the following result:

$$\begin{aligned} & \int_{\Delta\Omega_l} \mathbf{s} \cdot \int_{V_e} \begin{bmatrix} \phi_1 \\ \phi_2 \\ \phi_3 \end{bmatrix} [\nabla \phi_1, \nabla \phi_2, \nabla \phi_3] \begin{bmatrix} I_1 \\ I_2 \\ I_3 \end{bmatrix} dV d\Omega \\ &= \begin{bmatrix} \bar{\mathbf{s}} \cdot \mathbf{A}_{11} & \bar{\mathbf{s}} \cdot \mathbf{A}_{12} & \bar{\mathbf{s}} \cdot \mathbf{A}_{13} \\ \bar{\mathbf{s}} \cdot \mathbf{A}_{21} & \bar{\mathbf{s}} \cdot \mathbf{A}_{22} & \bar{\mathbf{s}} \cdot \mathbf{A}_{23} \\ \bar{\mathbf{s}} \cdot \mathbf{A}_{31} & \bar{\mathbf{s}} \cdot \mathbf{A}_{32} & \bar{\mathbf{s}} \cdot \mathbf{A}_{33} \end{bmatrix} \begin{bmatrix} I_1 \\ I_2 \\ I_3 \end{bmatrix} \end{aligned} \quad (7.25)$$

where $\bar{\mathbf{s}}$ is calculated by the expression,

$$\begin{aligned} \bar{\mathbf{s}} &= \int_{\Delta\Omega_l} \mathbf{s} d\Omega = [0.5(\theta_2 - \theta_1) - 0.25(\sin 2\theta_2 - \sin 2\theta_1)][(\sin \varphi_2 - \sin \varphi_1)\hat{i} + (\cos \varphi_1 - \cos \varphi_2)\hat{j}] \\ &+ 0.25(\cos 2\theta_1 - \cos 2\theta_2)(\varphi_2 - \varphi_1)\hat{k} \end{aligned} \quad (7.26)$$

and \mathbf{A}_{ij} is a vector given by

$$\mathbf{A}_{ij} = \int_{V_e} \phi_i \nabla \phi_j dV = \Delta\varphi_c \sum_{m=1}^{N_g} \phi_i(r_m, z_m) \nabla \phi_j(r_m, z_m) w_m r_m |J(r_m, z_m)| \quad (7.27)$$

Here the integral is evaluated numerically using the Gaussian quadrature, $\Delta\varphi_c$ is the rotation angle of the 3-D slice shown in Figure 7.3a, and N_g is the number of integration points. Also, J is the Jacobian.

The first volume integral on the right hand side of Eq. (7.18) may be calculated numerically with the result,

$$\int_{\Delta\Omega_l} d\Omega \int_{A_e} \begin{bmatrix} \phi_1 \\ \phi_2 \\ \phi_3 \end{bmatrix} [\phi_1, \phi_2, \phi_3] \beta(\mathbf{r}) dV = \begin{bmatrix} B_{11} & B_{12} & B_{13} \\ B_{21} & B_{22} & B_{23} \\ B_{31} & B_{32} & B_{33} \end{bmatrix} \quad (7.28)$$

where the matrix element B_{ij} is calculated by

$$B_{ij} = \Delta\Omega_l \Delta\varphi_c \sum_{m=1}^{N_g} \phi_i(r_m, z_m) \beta(r_m, z_m) \phi_j(r_m, z_m) w_m r_m |J(r_m, z_m)| \quad (7.29)$$

4.2 Surface integration over Γ_p

The second integral in Eq. (7.18) represents the jump condition (or numerical fluxes) across the boundary of the i th element and its neighbor (see Figure 7.3a). For a linear triangular element, the second integral is split into three terms, one for each side of the element,

$$\begin{aligned} \int_{\Delta\Omega \Gamma_p} \int \begin{bmatrix} \phi_1 \\ \phi_2 \\ \phi_3 \end{bmatrix} [\phi_1, \phi_2, \phi_3] \begin{bmatrix} [I]_1 \\ [I]_2 \\ [I]_3 \end{bmatrix} (\mathbf{n} \cdot \mathbf{s}) d\Gamma d\Omega &= \Delta\varphi_c \int_{L_1} \begin{bmatrix} \phi_1 \\ \phi_2 \\ \phi_3 \end{bmatrix} [\phi_1, \phi_2, \phi_3] \begin{bmatrix} [I]_1 \\ [I]_2 \\ [I]_3 \end{bmatrix} d\gamma \int_{\Delta\Omega} (\mathbf{n}_1 \cdot \mathbf{s}) d\Omega \\ + \Delta\varphi_c \int_{L_2} \begin{bmatrix} \phi_1 \\ \phi_2 \\ \phi_3 \end{bmatrix} [\phi_1, \phi_2, \phi_3] \begin{bmatrix} [I]_1 \\ [I]_2 \\ [I]_3 \end{bmatrix} d\gamma \int_{\Delta\Omega} (\mathbf{n}_2 \cdot \mathbf{s}) d\Omega &+ \Delta\varphi_c \int_{L_3} \begin{bmatrix} \phi_1 \\ \phi_2 \\ \phi_3 \end{bmatrix} [\phi_1, \phi_2, \phi_3] \begin{bmatrix} [I]_1 \\ [I]_2 \\ [I]_3 \end{bmatrix} d\gamma \int_{\Delta\Omega} (\mathbf{n}_3 \cdot \mathbf{s}) d\Omega \end{aligned} \quad (7.30)$$

where L_1 , L_2 , and L_3 are the lengths of the corresponding three sides of the

triangular element on the symmetry plane (see Figure 7.3b). The surface integrals can be evaluated numerically,

$$\int_{\Delta\Omega\Gamma_p} \begin{bmatrix} \phi_1 \\ \phi_2 \\ \phi_3 \end{bmatrix} [\phi_1, \phi_2, \phi_3] \begin{bmatrix} [I]_1 \\ [I]_2 \\ [I]_3 \end{bmatrix} (\mathbf{n} \cdot \mathbf{s}) d\Gamma d\Omega = \sum_{k=1}^3 \text{Cof}_{(4-k, 4-k)} \begin{bmatrix} C_{11}^k & C_{12}^k & C_{13}^k \\ C_{21}^k & C_{22}^k & C_{23}^k \\ C_{31}^k & C_{32}^k & C_{33}^k \end{bmatrix} \begin{bmatrix} [I]_1 \\ [I]_2 \\ [I]_3 \end{bmatrix} \quad (7.31)$$

where the matrix elements are calculated by the following numerical integration,

$$C_{ij}^k = \Delta\varphi_c \int_{L_k} \phi_i \phi_j d\gamma \int_{\Delta\Omega} (\mathbf{n}_k \cdot \mathbf{s}) d\Omega = \Delta\varphi_c \mathbf{n}_k \cdot \bar{\mathbf{s}} \sum_{m=1}^{N_g} \phi_i(r_m, z_m) \phi_j(r_m, z_m) w_m r_m |J(r_m, z_m)| \quad (7.32)$$

Also, $\text{Cof}_{(4-k, 4-k)}$ ($k=1,2,3$) means the matrix C , whose in which the $(4-k)$ th row and the $(4-k)$ th column are changed to zero; for example, $\text{Cof}_{(3, 3)}$ means forming the matrix by setting the elements in the 3rd column and the 3rd row of the matrix C to zero. Note that the above expression has been written for a curved element. For a linear element, the Jacobian J is a constant, which can be taken out of the summation sign.

In the DFE treatment, the jump terms have to be selected depending on the sign of $\mathbf{n}_j \cdot \bar{\mathbf{s}}$. This is different from the conventional finite element formulation in which the across-element continuity is enforced, and the inter-element boundary terms cancel each other such that a jump condition does not arise. One treatment of these jump terms that works effectively with linear elements is the upwinding scheme [Cui and Li, 2004a, b].

This scheme is also used here,

$$(\mathbf{n}_j \cdot \bar{\mathbf{s}}) \begin{bmatrix} [I]_1 \\ [I]_2 \\ [I]_3 \end{bmatrix} = -(-\mathbf{n}_j \cdot \bar{\mathbf{s}}) \begin{bmatrix} [I]_1 \\ [I]_2 \\ [I]_3 \end{bmatrix} = -\max(0, -\mathbf{n}_j \cdot \bar{\mathbf{s}}) \left\{ \begin{bmatrix} I_1 \\ I_2 \\ I_3 \end{bmatrix}_{NB} - \begin{bmatrix} I_1 \\ I_2 \\ I_3 \end{bmatrix}_{Elemi} \right\} \quad (7.33)$$

By the same token, the calculations for the other two sides can also be performed analytically. Note that $(I_j)_{NB} = (I_j^+)_{Elemi}$ by definition (see Figure 4b and also Eq. (7.16)).

Integration over Γ_φ

The surface integration over Γ_φ makes the evaluation of the following two terms,

$$\begin{aligned} \int_{\Delta\Omega_l} \int_{\Gamma_\varphi} \begin{bmatrix} \phi_1 \\ \phi_2 \\ \phi_3 \end{bmatrix} [\phi_1 \quad \phi_2 \quad \phi_3] \begin{bmatrix} [I]_1 \\ [I]_2 \\ [I]_3 \end{bmatrix} (\mathbf{n} \cdot \mathbf{s}) d\Gamma d\Omega &= \int_{\Delta\Omega_l} \int_{\Gamma_t} \begin{bmatrix} \phi_1 \\ \phi_2 \\ \phi_3 \end{bmatrix} [\phi_1 \quad \phi_2 \quad \phi_3] \begin{bmatrix} [I]_1 \\ [I]_2 \\ [I]_3 \end{bmatrix} (\mathbf{n}_t \cdot \bar{\mathbf{s}}) d\Gamma d\Omega \\ + \int_{\Delta\Omega_l} \int_{\Gamma_b} \begin{bmatrix} \phi_1 \\ \phi_2 \\ \phi_3 \end{bmatrix} [\phi_1 \quad \phi_2 \quad \phi_3] \begin{bmatrix} [I]_1 \\ [I]_2 \\ [I]_3 \end{bmatrix} (\mathbf{n}_b \cdot \bar{\mathbf{s}}) d\Gamma d\Omega & \end{aligned} \quad (7.34)$$

where Γ_t and Γ_b denote the top and bottom surfaces, respectively (see Figure 7.2b). For an axisymmetric problem, the surface normals for these two surfaces are calculated by the following expressions:

$$\mathbf{n}_t = -\sin(\Delta\varphi_c / 2)\hat{i} + \cos(\Delta\varphi_c / 2)\hat{j}, \quad \mathbf{n}_b = -\sin(\Delta\varphi_c / 2)\hat{i} - \cos(\Delta\varphi_c / 2)\hat{j} \quad (7.35)$$

Examination of the above integrals shows that the surface integrals can be carried out over the triangular element on the r-z plane. Consequently, we have the following

expressions:

$$\begin{aligned}
& \int_{\Delta\Omega_t} \int_{\Gamma_\varphi} \begin{bmatrix} \phi_1 \\ \phi_2 \\ \phi_3 \end{bmatrix} \begin{bmatrix} \phi_1 & \phi_2 & \phi_3 \end{bmatrix} \begin{bmatrix} [I]_1 \\ [I]_2 \\ [I]_3 \end{bmatrix} (\mathbf{n} \cdot \mathbf{s}) d\Gamma d\Omega \\
& = \begin{bmatrix} D_{11} & D_{12} & D_{13} \\ D_{21} & D_{22} & D_{23} \\ D_{31} & D_{32} & D_{33} \end{bmatrix} \left\{ (\mathbf{n}_t \cdot \bar{\mathbf{s}}) \begin{bmatrix} [I]_1 \\ [I]_2 \\ [I]_3 \end{bmatrix}_t + (\mathbf{n}_b \cdot \bar{\mathbf{s}}) \begin{bmatrix} [I]_1 \\ [I]_2 \\ [I]_3 \end{bmatrix}_b \right\}
\end{aligned} \tag{7.36}$$

where the matrix element D_{ij} involves a pure 2-D calculation and may be calculated numerically using the standard Gaussian quadrature,

$$D_{ij} = \int_{\Gamma_{r-z}} \phi_i \phi_j d\Gamma = \sum_{m=1}^{N_g} \phi_i(r_m, z_m) \phi_j(r_m, z_m) w_m |J(r_m, z_m)|$$

Here Γ_{r-z} means the area on the r-z plane is used. Note that for a linear triangular element, the above expression may also be evaluated analytically, as shown in the Chapter 6.

The jump conditions across the element interface can be also treated using the upwinding scheme also for both the top and bottom surfaces. The use of this scheme leads to the following expressions:

$$(\mathbf{n}_t \cdot \bar{\mathbf{s}}) \begin{bmatrix} [I]_1 \\ [I]_2 \\ [I]_3 \end{bmatrix} = -\max(0, -\mathbf{n}_j \cdot \bar{\mathbf{s}}) \left\{ \begin{bmatrix} I_1 \\ I_2 \\ I_3 \end{bmatrix}_{NB,t} - \begin{bmatrix} I_1 \\ I_2 \\ I_3 \end{bmatrix}_{Elemi,t} \right\} \tag{7.37}$$

are stored in memory during calculation. The intensities at any other location in the entire cylinder can be obtained from the intensity values stored at the triangular element through an appropriate mapping procedure. The mapping procedure exploits the symmetry and periodic conditions associated with the axisymmetry of the problem. If the angle of the rotation $\Delta\varphi_c$ is appropriately selected, then the intensities in the neighboring elements along the φ direction can be mapped from those at nodes P1, P2, and P3, respectively. This procedure will allow the 3-D calculations to be performed using the 2-D mesh on the r-z plane only.

The mapping procedure was studied by Chui and Raithby (1992) and Murthy and Mathur (1998a) for finite volume analysis of radiative heat transfer. Here a similar idea is applied to incorporate the mapping into the DFE formulation to facilitate the radiative heat transfer calculations over a 2-D mesh only. As shown in Figure 7.4, the rotation angle is deliberately chosen as to be the same as the control angles in the φ direction, which equals $2\pi/N_\varphi$ where N_φ is the number of discretization of angular space in the φ direction. From Eq. 7.23, it is clear that when the upwinding procedure is used, intensity values at the adjacent elements are needed in order to calculate the in-flow contributions from either the top or the bottom surface. Since the intensity is stored at the nodal points of the element on the r-z plane, the intensity field at the neighboring elements may be obtained using the axisymmetry and periodic conditions. As shown in

Figure 7.4, the element a-b-c-d is on the middle (or r-z) plane, and a-b-c_t-d_t is the element that shares the same boundary with the top surface a-b-c-d, while the element a-b-c_b-d_b shares the same boundary with the bottom surface a-b-c-d. The angle between the lines P1P2 and P1_t P2_t and that between the lines P1P2 and P1_b P2_b is equal to $\Delta\varphi$ and $-\Delta\varphi$ respectively, because of the angular discretization.

Because the radiative intensity possesses axisymmetry or rotational symmetry, one thus has the following relation for the intensities at the three elements under consideration,

$$I_i(\varphi_c = 0) = I_i(\varphi_c = -\Delta\varphi) = I_i(\varphi_c = \Delta\varphi) \quad i = 1, \dots, N_\varphi \quad (7.39)$$

where N_φ is the number of discretized azimuthal angles. The indices on $i+1$ and $i-1$ are cyclic such that $i+1 \rightarrow 1$ if $i = N_\varphi$ and $i-1 \rightarrow N_\varphi$ if $i=1$. Thus, all the intensities on the other planes are the same as those on the symmetry (i.e. r-z) plane with an appropriate rotation. Also, to comply with the condition of axisymmetry, the net radiation energy flux across any plane passing through the $r=0$ axis should be zero. Thus, the following relation among the intensities at $\varphi_c = 0$ is,

$$I_i(\varphi = 0) = I_{N_\varphi - i + 1}(\varphi = 0) \quad (7.40)$$

This condition implies that to avoid numerical errors N_φ needs to be an even number, which imposes a constraint on the way the polar angle discretization is made.

While this constraint may be a nuisance, it is beneficial in that only half of the directions need be solved, thereby speeding up the computations.

With reference to Figure 7.4, the intensity in the direction 1 at $\varphi_c = 0$ is parallel to that in the direction 2 at $\varphi_c = -\Delta\varphi$ and also to that in the direction 6 at $\varphi_c = \Delta\varphi$. This periodic condition should hold true for other corresponding directions as well. This condition, in combination with the axisymmetry condition discussed above, allows us to obtain information on the intensities at the top Γ_t and bottom Γ_b from those saved at the element defined at the r-z plane. To see that, we first consider the intensity I_{t2} of direction 2 at the top surface. The quantity I_{t2} is mapped from the known values at the r-z plane as follows:

$$I_{t2}^- = I_2(\varphi_c = 0) \text{ and } I_{t2}^+ = I_1(\varphi_c = \Delta\varphi) = I_1(\varphi_c = 0) \quad (7.41)$$

The same relation applies to the intensities at the other directions. The mapping can be applied in a similar fashion to the intensities at the bottom surface with the results,

$$I_{b2}^- = I_2(\varphi_c = 0) \text{ and } I_{b2}^+ = I_3(\varphi_c = -\Delta\varphi) = I_3(\varphi_c = 0) \quad (7.42)$$

Clearly, the same relation can be used for the other directions as well. Here to be consistent with our notations, the subscript + refers to the outside of the elements.

Treatment of the scattering term

It is known that particles present in a medium will scatter the radiative intensity traveling in one direction into all other directions. Likewise, the radiation in other directions may also be scattered by the particles into the given direction in a scattering medium. Scattering effects are usually classified into isotropic scattering and anisotropic scattering. The former scatters energy to all other directions with the same energy distribution, whereas anisotropic scattering redirects radiation energy to different directions with varying energy distributions. The isotropic scattering function is simple and easy to calculate by Eq. (7.43),

$$\Phi(\mathbf{s}, \mathbf{s}') = 1 \quad (7.43)$$

Anisotropic scattering is more complex and certainly needs more computing time since the scattering function is directionally dependent. There are two different models being used for anisotropic scattering functions: the forward scattering and backward scattering. The scattering functions, either forward or backward, may be described by the following generic expression:

$$\Phi(s, s') = \sum_{j=1}^{N_s} c_j P_j(\cos \varpi) \quad (7.44)$$

where ϖ is calculated by

$$\varpi = \cos \theta \cos \theta' + (1 - \cos^2 \theta)(1 - \cos^2 \theta')^{1/2} \cos(\varphi' - \varphi) \quad (7.45)$$

and P_j is the Legendre polynomial, which can be calculated by Eq. (7.46),

$$\begin{cases} p_0(x) = 1 \\ p_1(x) = x \\ p_{n+1}(x) = \frac{2n+1}{n+1}xp_n(x) - \frac{n}{n+1}p_{n-1}(x) \end{cases} \quad (7.46)$$

For the calculations given here, the values of coefficient c_j in Eq. (7.44) are taken from Kim and Lee (1988), where the coefficients of the polynomial for different models are obtained by slightly modifying the Mie coefficients [Wiscombe, 1980]. The four different scattering functions are shown in Figure 7.7(a).

Eqs. (7.45) and (7.46) describe the dependence of the scattering function on the directions for anisotropic scattering phenomena. In calculations, the angular space is discretized into a finite number of control angles. While the scattering function at the axial direction of a control angle may be used as the average scattering function, a better approach is to average the scattering function over each control angle using the following expression [Chai and Partankar, 2000]:

$$\overline{\Phi}(\mathbf{s}, \mathbf{s}') = \frac{\int_{\Delta\Omega} \int_{\Delta\Omega'} \Phi(\mathbf{s}, \mathbf{s}') d\Omega d\Omega'}{\int_{\Delta\Omega} \int_{\Delta\Omega'} d\Omega d\Omega'} \quad (7.47)$$

The above procedure and scattering functions can be readily incorporated into the

discontinuous finite element formulation as a source term. The integration of the source term may be made using the integration quadrature rules,

$$\begin{aligned}
F_i &= \int_{V_e} \frac{\sigma(\mathbf{r})}{4\pi} \int_{\Delta\Omega_l} \sum_{j=1}^{N\Omega} \int_{\Delta\Omega'_j} \phi_i(\mathbf{r}) I(\mathbf{r}, \mathbf{s}'_j) \Phi(\mathbf{s}, \mathbf{s}') d\Omega' d\Omega dV \\
&= \Delta\varphi_c \sum_{m=1}^{N_g} \frac{\sigma(r_m, z_m)}{4\pi} w_m \phi_i(r_m, z_m) r_m |J(r_m, z_m)| \sum_{j=1}^{N\Omega} I(\mathbf{r}_m, \mathbf{s}'_j) \bar{\Phi}(\mathbf{s}_l, \mathbf{s}'_j) \Delta\Omega_l \Delta\Omega'_j
\end{aligned} \tag{7.48}$$

where subscript i refers to the node number local to the element. The force, calculated as described above, is then added to the i th node of the element.

Summary

Assembling all these discretized terms together, the equation for the i th element can be written in terms of the following matrix form:

$$[K]\{I\} = \{f\} \tag{7.49}$$

where the expressions for the matrix elements are summarized as follows:

$$k_{ij} = \int_{V_e} \phi_i \nabla \phi_j \cdot \int_{\Delta\Omega_l} \mathbf{s} d\Omega dV + \int_{V_e} \phi_i \phi_j \beta dV \int_{\Delta\Omega_l} d\Omega + \sum_{k=1}^{Nd} \max(0, - \int_{\Delta\Omega_l} \mathbf{s} \cdot \mathbf{n}_k d\Omega) \int_{\Gamma_k} \phi_i \phi_j d\Gamma \tag{7.50}$$

$$f_i = \int_{V_e} \phi_i S dV \int_{\Delta\Omega_l} d\Omega + \sum_{k=1}^{Nd} \max(0, - \int_{\Delta\Omega_l} \mathbf{s} \cdot \mathbf{n}_k d\Omega) \int_{\Gamma_k} \phi_i \phi_j I_{NB} d\Gamma \tag{7.51}$$

with Nd being the number of boundaries associated with the i th element.

For those elements associated with a boundary element, where the boundary

condition is imposed as follows if the boundary is gray:

$$I^+(\mathbf{r}, \mathbf{s}_l) = \varepsilon(\mathbf{r})I_b(\mathbf{r}) + \frac{1 - \varepsilon(\mathbf{r})}{\pi} \sum_{j=0, \mathbf{s}_j \cdot \mathbf{n} > 0}^{N_\Omega} I^-(\mathbf{r}, \mathbf{s}_j') |\mathbf{s}_j' \cdot \mathbf{n}| \Delta\Omega'_j \quad (7.52)$$

The following equation is used for the symmetry boundary condition:

$$I^+(\mathbf{r}, \mathbf{s}_l) = I^-(\mathbf{r}, \mathbf{s}_l^*) \quad (7.53)$$

Here \mathbf{s}^* is the symmetric direction of \mathbf{s} with respect to the boundary, and can be calculated by Eq. (7.4). Eq. (7.49) can be obtained for each element and its neighbors, and the calculations are then performed element by element. Thus, with Eq. (7.49), the calculation for the i th element starts with selecting a direction and continues element by element until the entire domain and all directions are covered. Because of the boundary conditions, iterative procedures are required to reach convergence criteria. Experience suggests that the successive substitution method seems to work well for these types of problems.

7.5. RESULTS AND DISCUSSION

In this section, the above formulation is applied to study several cases of radiative transfer in participating medium with and without scattering. The coupling of the discontinuous and conventional finite elements for the mixed-mode heat transfer

calculations including conduction and convection is discussed in the last example. In the results plotted below, the nondimensionalized radiative heat flux $q^*(\mathbf{r}) = -q(\mathbf{r})/(\sigma_s T_{ref}^4)$ is used as the vertical axis and a positive $q^*(\mathbf{r})$ means the wall flux goes into the wall. This definition is used in order to compare with results reported in literature. Here the radiative heat flux $q(\mathbf{r})$ from the wall into the medium is calculated either by

$$q(\mathbf{r}) = \mathbf{q}(\mathbf{r}) \cdot \mathbf{n}_w = \int_{4\pi} I(\mathbf{r}, \mathbf{s}) \mathbf{s} \cdot \mathbf{n}_w d\Omega \quad (7.54)$$

or equivalently by

$$q(\mathbf{r}) = \mathbf{q}(\mathbf{r}) \cdot \mathbf{n}_w = \varepsilon \left(\sigma_s T_w^4 - \int_{\mathbf{s} \cdot \mathbf{n}_w < 0} I(\mathbf{r}, \mathbf{s}) \mathbf{s} \cdot \mathbf{n}_w d\Omega \right) \quad (7.55)$$

where \mathbf{n}_w is the wall normal pointing into the medium.

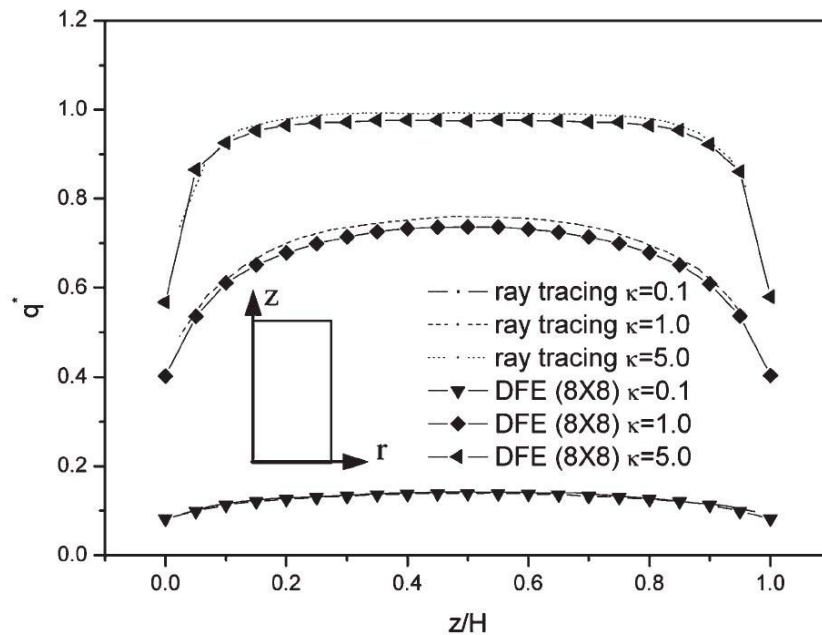
Case 1: Radiative transfer in a finite cylinder

As the first example, the DFE formulation is applied to compute the radiative transfer in a cylindrical enclosure filled with an emitting, absorbing, and non-scattering medium. The temperature of the medium is set at a constant $T_{ref} = 100$ K. The height and radius of the cylinder are 2m and 1m, respectively. All the walls are black ($\varepsilon_w = 1$) and at

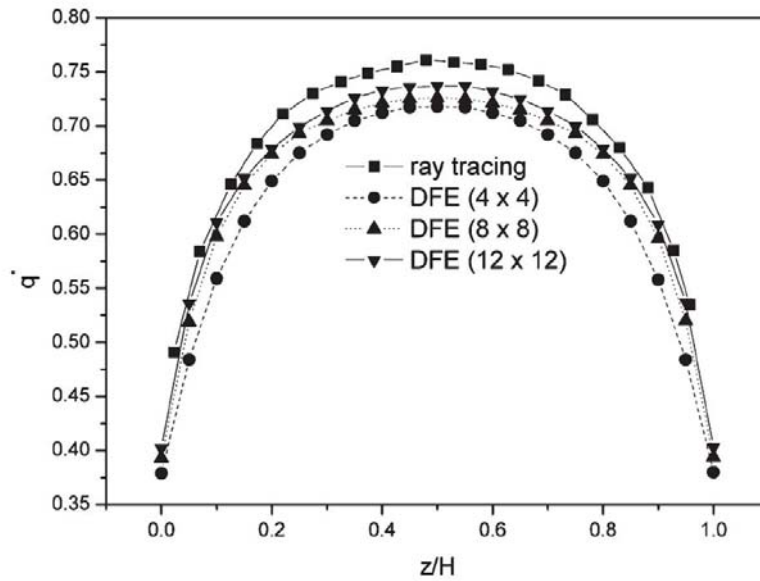
$T_w=0$ K. This is perhaps an unproclaimed benchmark problem against which many different numerical schemes are checked [Murthy and Mathur, 1998]. For this case, the DFE calculation used a structured mesh consisting of 400 linear triangular elements and an angular discretization of $8(\theta) \times 8(\varphi)$. Figure 7.5a compares the results of dimensionless heat flux along the side wall of the cylinder obtained by the DFE method with the calculations using the ray tracing method for three different absorption coefficients. The radiative heat flux attains a maximum at the middle of the side wall and a minimum at the top and the bottom of the cylinder. This is attributed to the fact that more energy is emitted into the wall at the middle than at the end walls, or the sum of the intensities is largest and decreases as it gets closer to the ends. The heat flux is also affected by the absorption coefficient of the medium. As suggested by the term $\kappa(\mathbf{r})I_b(\mathbf{r})$ in Eq. (7.1), a more absorbing medium also emits more energy to the wall, thereby leading to a larger wall heat flux. These characteristics of thermal radiative transfer are predicted very well by the DFE method, as appears in Figure 7.5a. As seen from the figure also, good agreement exists between the present and reported results [Murthy and Mathur, 1998], with the error in the maximum q^* being of 0.46% and 3.01% and 1.67% for $\kappa = 0.1$, $\kappa = 1.0$ and $\kappa = 5.0$.

It is known from experience that for radiative transfer calculations, the angular space and volume space discretization affects the numerical accuracy. Simulations were

performed to determine these discretization effects and some of the results are given in Figure 7.5b, where the wall heat flux is plotted as a function of angular discretization. As expected, a better numerical accuracy is obtained when a finer control angle discretization is used. It is noted that the errors are enlarged by using a different vertical range to display the effect of angle discretization. Although not shown, the element size also affects the numerical accuracy, but to a much smaller degree if a finer mesh is used. Further calculations also confirm that the azimuthal angle must be discretized evenly so that the heat flux in any plane in the φ_c direction is zero. An uneven discretization of the control angle would produce poor accuracy in the calculated heat fluxes.



(a)



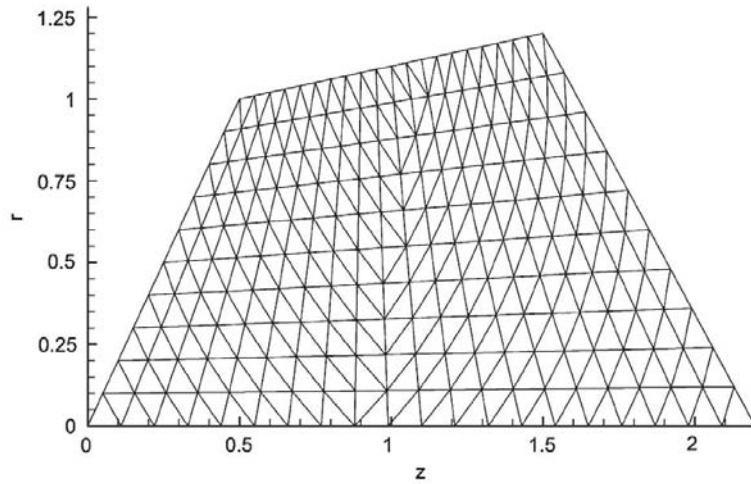
(b)

Figure 7.5 Computed non-dimensional heat flux distribution along the sidewall of a finite cylinder: (a) comparison with the results reported in the literature at $\kappa=0.1$, $\kappa=1.0$ and $\kappa=5.0$ and (b) effects of angular discretization on calculated wall heat flux distribution.

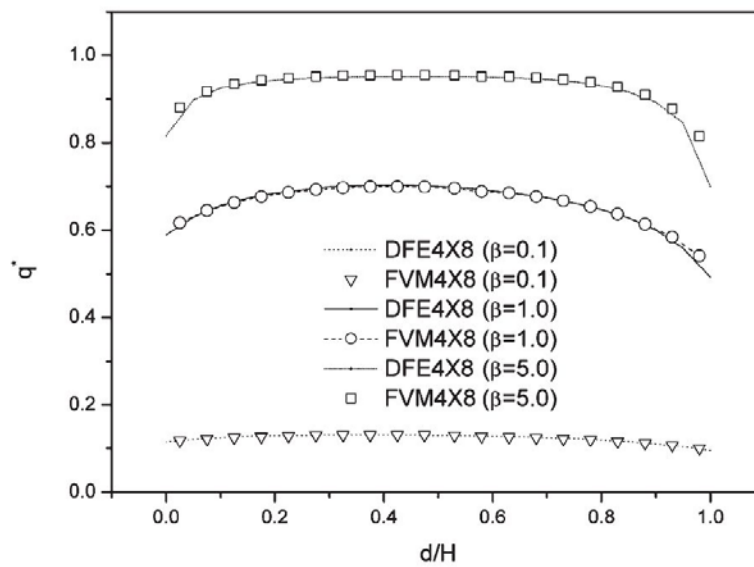
Case 2: Radiation in an irregular enclosure

In this case the geometry is a quadrilateral domain filled with an absorbing and emitting medium with $\kappa=1.0$ at a constant temperature $T_{\text{ref}}=100$ K, and the scattering effect is neglected. All boundaries are black and cold, the domain is defined by the vertices in an anticlockwise order, (0.0, 0.0), (2.2, 0.0), (1.5, 1.2) and (0.5, 1.0). The mesh used in this case is given in Figure 7.6(a), which consists of 400 triangular elements, and

4 × 8 ($\theta \times \varphi$) solid control angles. The calculated heat flux along the side wall from (0.5, 1.0) to (1.5, 1.2) is plotted in Figure 7.6(b) as a function of the medium optical thickness, along with the solutions obtained using the finite volume method, the two agree very well for the range of absorption coefficients studied.



(a)

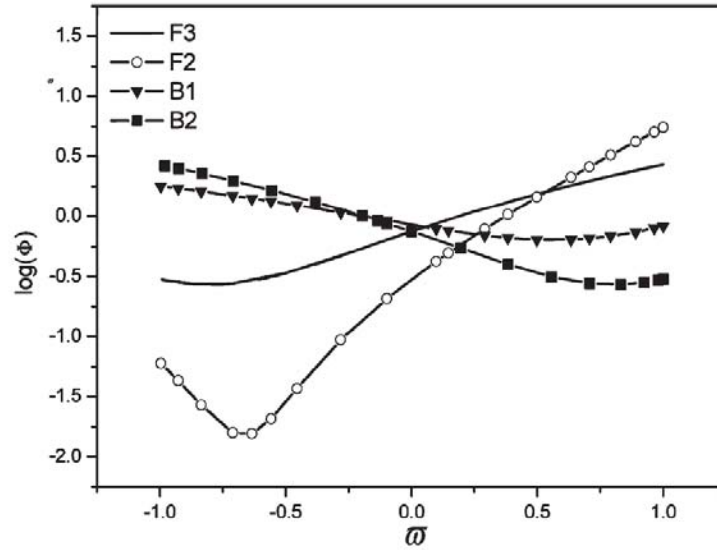


(b)

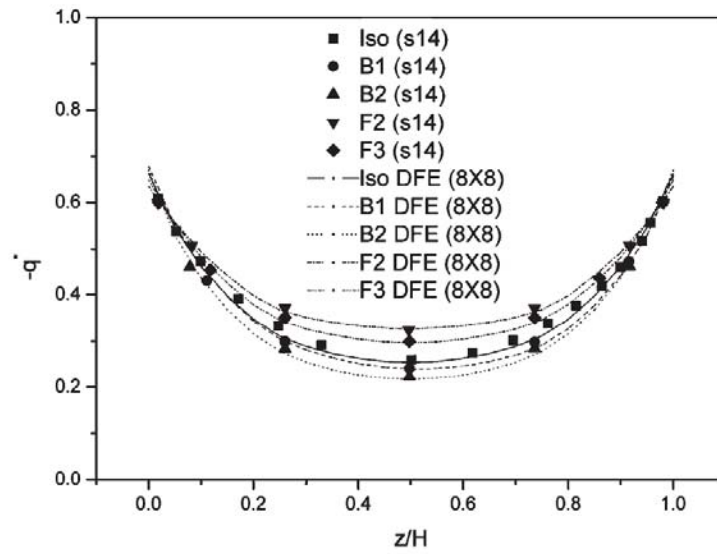
Figure 7.6 Radiative transfer in an irregular quadrilateral of axisymmetry: (a) structured mesh consisting of 400 structured triangular elements and (b) comparison of heat flux q^* on the wall (defined by points (0.5, 1.0) and (1.5, 1.2)) calculated by the DFE and finite volume methods for different absorption coefficients, $\kappa=0.1$, $\kappa=1.0$ and $\kappa=5.0$.

Case 3: Pure scattering problem

The geometry is the same as that in Case 1, but the medium is purely scattering, that is, the scattering albedo is $\omega=1.0$. The optical thickness is fixed at $\beta R=1.0$. The medium is cold, i.e., $T_{\text{ref}}=0$ K. The wall of the enclosure is black, with its two ends being cold and the side wall kept at a constant temperature, $T_{\text{ref}}=100$ K. Figure 7.7 depicts the net radiative heat flux distribution along the side-wall of the enclosure as a function of scattering phase functions F2, F3, B1, and B2. The coefficients of the phase function are taken from Kim and Lee [1988] and Jendoubi and Lee (1993). The results calculated by the DFE method once again compare well with the results reported in Jendoubi and Lee (1993). Once again, the basic radiative transfer characteristic is also predicted correctly in that near the hot wall the medium with a stronger back scattering function irradiates more energy into the wall, which in turn results in a smaller heat flux into the wall (see Eq.7.54). The opposite is true when the medium scatters strongly in the forward direction.



(a)



(b)

Figure 7.7. Computed results for radiative transfer in a cylinder filled with scattering media: (a) scattering phase functions and (b) comparison of heat flux distribution on the side wall between DFE and Discrete Ordinates method for different scattering phase functions (Isotropic, F2, F3, B1, and B2). Conditions used for calculations: $\beta=1.0$ and

$\omega=1.0$.

Case 4: Mixed heat transfer in a rotating cylinder

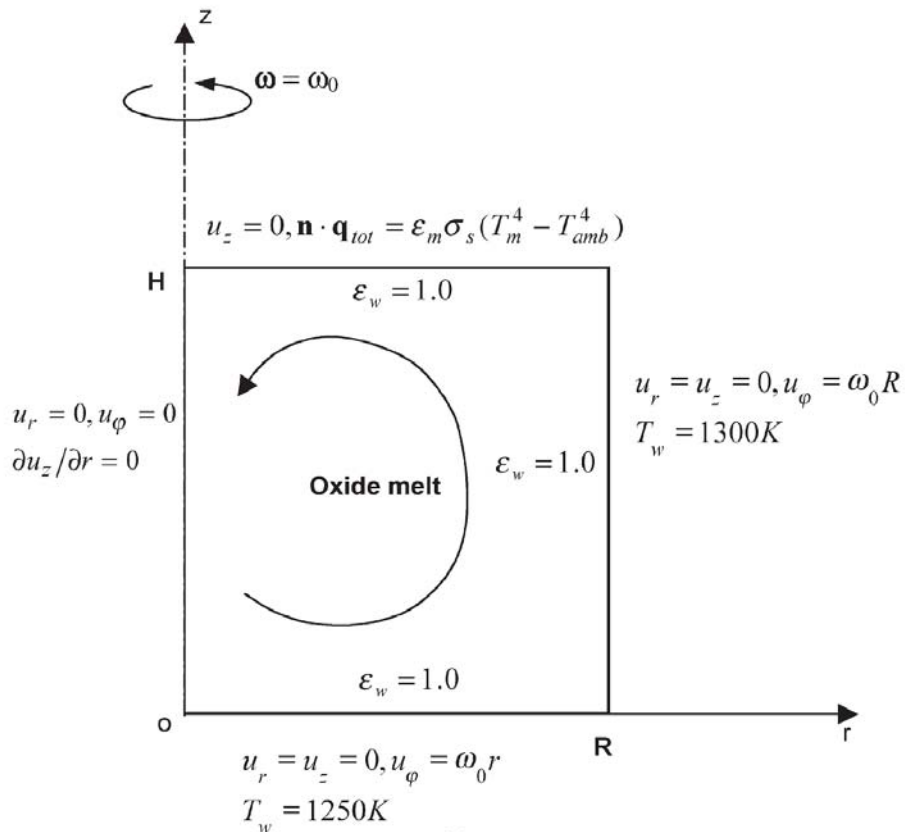
As the last case, we consider a mixed heat transfer involving conduction, convection and radiation in a cylindrical container of axisymmetry under a given rotation. This case is just used to illustrate the coupling of the discontinuous and convection finite element methods for mixed mode heat transfer calculations. The container is filled with a high temperature semitransparent melt, which is absorbing and emitting in the infrared range, and as such the radiative heat transfer must be considered along with conduction and convection, as shown in Figure 7.8a. The equations governing the momentum and thermal transport processes are the Navier-Stokes and the energy balance equations,

$$\rho c_p \frac{\partial T}{\partial t} + \rho c_p \mathbf{u} \cdot \nabla T = \nabla \cdot (k \nabla T - \mathbf{q}_r) + q''' \quad (7.56)$$

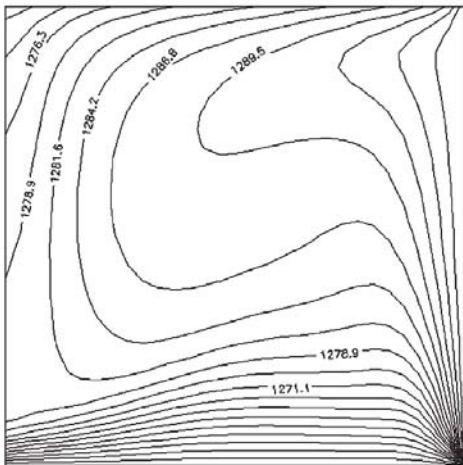
$$\nabla \cdot \mathbf{u} = 0 \quad (7.57)$$

$$\rho \frac{\partial \mathbf{u}}{\partial t} + \rho \mathbf{u} \cdot \nabla \mathbf{u} = -\nabla p + \nabla \cdot \mu (\nabla \mathbf{u} + (\nabla \mathbf{u})^T) \quad (7.58)$$

where $\mathbf{u}(r, z) = (u_r, u_{\phi}, u_z)$ is a function of r and z only. C_p is specific heat at constant pressure, k is thermal conductivity, ρ is density, μ is viscosity, t is time, and p is pressure. The radiative heat transfer is described by Eq. (7.1) and the radiative heat source is calculated by Eq. (2.20). These boundary conditions are also given in Figure 7.8a.

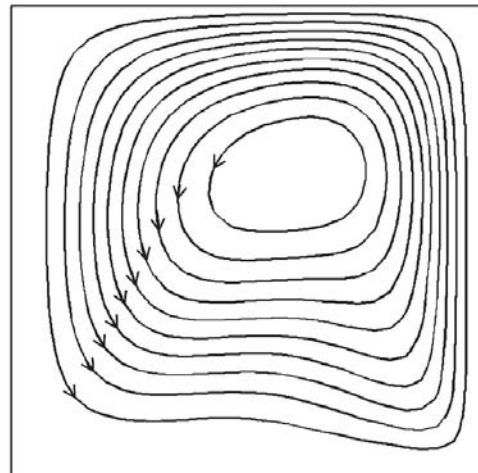


(a)



Temperature K

(b)

maximum $\psi = 0.25363 \times 10^{-2}$

(c)

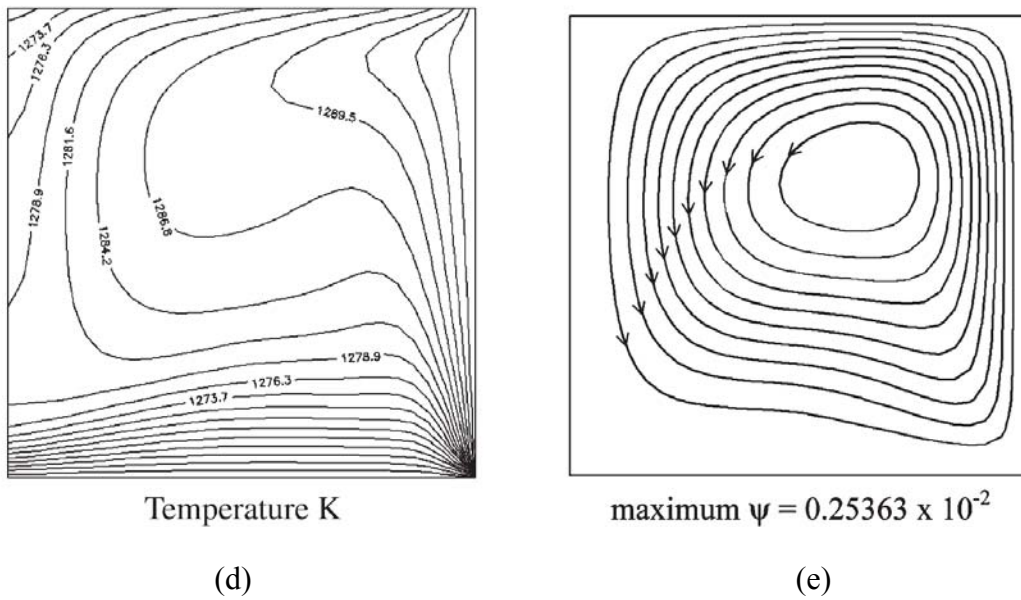


Figure 7.8. Coupled FE/DFE calculation of mixed-mode heat transfer in a rotating cylinder filled with semi-transparent melt: (a) schematic representation of the mixed mode problem involving swirling flows, (b) and (c) distribution of the temperature field and flow field for $\kappa=0.1 \text{ m}^{-1}$, (d) and (e) distribution of the temperature field and flow field for $\kappa=10 \text{ m}^{-1}$. Conditions used for calculations are as follows: rotating speed $\omega=0.05$, $R=0.05\text{m}$, and $H=0.05\text{m}$. All the boundaries are black. The side wall ($R=0.05\text{m}$) temperature is fixed at $T=1300 \text{ K}$, and the bottom surface ($H=0\text{m}$) temperature is 1250K . The ambient temperature is $T_{\text{amb}} = 1240 \text{ K}$ and $\varepsilon_m=1$. The material properties are: $\rho=4073 \text{ kg/m}^3$, $k=4.0 \text{ W/m}\cdot\text{K}$, $\mu=0.046 \text{ kg/s}\cdot\text{m}$, and $C_p=687.0 \text{ J/kg}\cdot\text{K}$.

To obtain information on the temperature and fluid flow distribution in the melt, the Navier-Stokes equations need to be solved along with the energy and radiative

transfer equations. In the present case, the Navier-Stokes and thermal energy balance equations are solved using the conventional finite element method, while the radiative transfer equation is solved using the discontinuous finite element method described in this work. The solution of the Navier-Stokes and thermal transport equations is well documented elsewhere [Song *et al.*, 2003; Lan and Howell, 2003], including numerical accuracy and code verification, and is thus omitted.

Since the radiation heat flux contribution appears as a divergence term in the source part of the heat balance equation, two approaches may be applied to couple the discontinuous and conventional finite elements for the mixed heat transfer calculations. In the first approach, the heat balance equation is formulated following the same procedure as used in the conventional finite element method. This will lead to a global matrix equation with the nodal temperatures as the unknowns. To incorporate the internal radiation effect, $\nabla \cdot \mathbf{q}_r$ is calculated over a finite element where the internal radiation takes place and then coupled to the global matrix equation as a source term. This represents a simple and direct approach. A boundary condition on $\mathbf{n} \cdot \mathbf{q}_c$ is required, which must satisfy the total heat flux ($\mathbf{q}_c + \mathbf{q}_r$) balance along the boundary [Bennett, 2003; Shu and Li, 2004]. It is remarked here that $\nabla \cdot \mathbf{q}_r$ is calculated using the angular integration and thus there is no loss in numerical accuracy.

The second approach is often used within the context of the finite volume

formulations for temperature calculations. When used for the conventional and discontinuous finite element coupling, this approach requires the use of the following integration-by-parts to transfer the divergence operation onto the shape function:

$$\int_{\Omega_i} \nabla \cdot \mathbf{q}_r \phi \, dV = \oint_{\partial\Omega_i} \mathbf{q}_r \cdot \mathbf{n} \phi \, dS - \int_{\Omega_i} \nabla \phi \cdot \mathbf{q}_r \, dV \quad (7.59)$$

Thus information is required on \mathbf{q}_r in the interior of an element and along the domain boundaries. A specification of total heat flux ($\mathbf{n} \cdot \mathbf{q}_r$ and $\mathbf{n} \cdot \mathbf{q}_c$) for the boundary term is required, which is more convenient for problems involving different phases [Shu and Li, 2004].

Either of the two approaches described above for the combined heat conduction and radiation calculations requires an iterative computational procedure. The two approaches described above give the same result. In this study, the first approach is taken.

In a typical iteration process, the temperature distribution is calculated using the conventional finite elements while the internal radiation intensities are determined by the discontinuous finite elements. The iteration starts with the calculation of the fluid flow and temperature without radiative heat transfer. The solution of the intensity distribution and hence the divergence of heat fluxes are then calculated using the temperature information. The radiation heat flux divergence is then treated as a heating source and the

temperature distribution is updated. This process repeats itself until a convergence on the fluid flow, temperature and intensity is reached. For the results presented here, a relative error of 10^{-4} is set as the convergence criterion for all variables. The selection of relaxation parameters for the mixed mode calculations is discussed in Shu and Li, (2004).

The results obtained by the coupled conventional/discontinuous finite element method for the temperature and fluid flow field distributions are compared in Figures 7.8b for two different absorption coefficients. The buoyancy forces drive the recirculating melt flow, which goes upward along the sidewall where temperature is high and comes downward along the centerline. The flow field exerts a strong effect on the temperature distribution. The calculated results also show that both the flow and temperature fields are affected by the internal radiative heat transfer. An increase in the absorption coefficient causes a change in the temperature distribution, which in turn increases the flow intensity in the melt. This is consistent with other reported studies [Kobayashi *et. Al.*, 1997; Shu and Li, 2004].

7.6. CONCLUDING REMARKS

This chapter has presented a discontinuous finite element (DFE) formulation for the numerical solution of internal thermal radiation problems in axisymmetric enclosures. The radiative transfer computation over an axisymmetric geometry is essentially three-

dimensional. However, an appropriate mapping procedure based on the use of the axisymmetric and periodic conditions associated with the enclosures can be applied to perform the 3-D calculations over a 2-D mesh only. This feature is important in that it leads to a significant reduction in both computing time and memory storage requirement. The discontinuous finite element formulation and numerical implementation for axisymmetric internal radiation heat transfer calculations were given. A detailed discussion was made to illustrate the procedures for incorporating the mapping in the discontinuous formulation to convert an essentially 3-D calculation into a 2-D calculation. Several case studies for radiative heat transfer in absorbing, emitting and scattering media were presented and the results compare well with the solutions reported in the literature using other numerical schemes. The effects of both solid-angular and spatial discretization were discussed. The numerical simulations confirm the theory that an even discretization of a solid angle is important to ensure an adequate numerical accuracy. The last example discussed the coupling of the discontinuous and conventional finite element methods for mixed heat transfer calculations, including swirling flow, conduction, convection driven by buoyancy and radiation in participating media.

CHAPTER 8

NUMERICAL SIMULATIONS OF RADIATIVE HEAT TRANSFER IN LASER HYPERTHERMIA

8.1. INTRODUCTION

Hyperthermia is a heat treatment method for cancer. The basic idea is to use a certain energy source to heat local tissue or the whole body, so that the local temperature of the tissue being heated is increased. The body of a human being maintains a stable temperature around $37^{\circ}c$, and can sustain and survive of a body temperature of up to $42^{\circ}c$. However, the tumour is more sensitive than normal tissue to temperature, and is easily damaged by high temperature. Based on this fact, hyperthermia gives at least three benefits in cancer treatment [Sturesson, 1998]. The first is direct kill, which uses high temperature to kill tumour cell. In clinical trial, hyperthermia is applied to the tumour cells directly and the temperature is maintained until the tumour is killed. The second benefit is indirect killing of tumour cells. The tumour will be destroyed due to the microvasculature. The third benefit is the increase of sensitization of other cancer treatments, such as radiology and chemical treatment. But if the temperature of cells is increased to above $50^{\circ}c$, the difference of sensitization of tumour cells and normal cells is disappeared. This means the normal cells will be destroyed with tumour cells at the

same speed.

The cells destroyed or damaged by heat are affected in several different ways. First, when the temperature of cells is increased, the protein structure of the cells change due to the hydrogen bonds breaking and the ionic interactions disturbing [Leper, 1984]. This effect is dependent on the pH value of cells, and tumour cells usually have a lower pH value than normal cell, which causes the tumour cells to be more sensitive than normal tissues [Gerweck, 1985]. The second effect is the blood supply. As we know, excessive heat in tissue is dissipated or transferred by blood circulation and blood circulation in tumour is more restricted, so it takes longer time for tumour dissipates the heat than normal tissue. As a result, the tumour will be kept at a higher temperature than normal tissue.

As many researchers have presented, tumour cells are more sensitive to heat than normal tissue. If the body temperature is increased, the tumour cells are more vulnerable than healthy cell. This fact provides a selective ways to target the tumour cells in normal tissues. In addition, research also shows that the tumour undergoing hyperthermia is more sensitive to other treatments, such as chemical treatment or radiology, since the cancer cells is hard to distinguish from normal tissues. The hyperthermia causes minimal damage to healthy cells. Therefore, if we can target tumour cells precisely, we will provide an effective cancer treatment with a very limit side effect.

Hyperthermia can be applied to the whole body, larger regions, or specific locations. The whole body hyperthermia is used to treat the cancer which has spread to multiple large places of body. Usually a thermal chamber is used to increase the temperature of the whole body, but the body temperature of the patient must be kept under 42°C . The hyperthermia applied to larger regions is usually induced by microwave, radiofrequency, ultrasound, or laser beam. For the specific locations, hyperthermia can be induced externally or by using probe to reach tumour, and laser beam is widely used. All these methods of hyperthermia can be categorized into external methods, since these methods apply energy to the external of body or not deep from skin. Compared with external hyperthermia methods, the internal methods raise the body temperature by using some medicine to induce fever, or to use thermal chamber to elevate the patient's body temperature. The internal methods are treatments to the patient with spread cancer.

Several methods have been used in local position cancer treatment. The most widely used methods are laser beam, microwave, radiofrequency, ultrasound, and magnetic fluid. The microwave and laser beam usually are used in both superficial and deep-seated tumours. For the superficial tumours such as skin cancer, the laser beam or microwave is applied on the tumours directly, for some deep-seated tumours, such as lung cancer, the diffusing fiber is used. Radiofrequency is another method for

hyperthermia or tissue ablation [Mcgahan, 1990]. The idea of radiofrequency hyperthermia is to deliver a high frequency electric current to tumours through a needle electrode. The name of radiofrequency comes from the frequency of electric current, which is about 480 KHz, and this frequency is in the range of radio transmission. Since the electric current changes direction with a high frequency, the ions in the tissues around the needle electrode also changes direction with a high frequency. This causes heat generation due to friction between the ions and tissues. Therefore, the tissues will be heated and temperature of the tissues will arise. Radiofrequency method is also an external method, and the effective range of this method is about 4.5-5 cm sphere around the tip of electrode. [Nazir, *et al.*, 2003]

Magnetic fluid hyperthermia is induced by injecting nanoparticles into tumours, and then applies alternating magnetic fields. The magnetic nanoparticles rotate due to magnetic force, and heat will be generated by nanoparticles in an alternating magnetic fields due to hysteresis loss [Shinkai, *et al.*, 1994] and friction created by the movement of nanoparticles [Hergt *et al.*, 1998]. However, the heat generated by friction is much less than from hysteresis loss. The tumours being injected nanoparticles is heated due to magnetic field and then the temperature of tumours arises, but the normal tissues can keep normal temperature since no nanoparticles are in it.

Laser has several unique features, such as high intensity, coherence,

monochromaticity [Sturesson, 1998]. Due to these unique features, laser has been widely used in many different areas after it was invented in 1960. Lasers are used in surgery for many types of cancers [Stanford cancer center], since these types cancers need treatments with some special requirements. Laser can satisfy these special requirements. One example is that some tumours are hard to reach, and only a small area needs to be heated. Laser can reach these tumours by using fibers. These cancers include Skin, Breast, Cervical, Vocal cord, Vaginal, Lung, Vulvar, Penile, Palliative surgery.

The advantages of laser hypothermia

The laser hypothermia has the following advantages over other methods:

1. Lasers are very precise; therefore, the laser will cause less damage to healthy tissues, less blood, less scars, and less infection.
2. Since laser hypothermia will not cut and burn the tissues of body, the patients will feel less pain.
3. The laser hypothermia will take less time for patient to heal after surgery.

Basically, lasers are electronic magnetic waves as same as microwaves. But the biggest difference is that they have different wave lengths. Laser has been deployed in hyperthermia field, since their energy is high and easy to control. Laser can be absorbed by normal tissues and tumours, but the absorption of energy varies due to different

wavelengths. Since the absorption and scattering effects of tissues are pretty strong, a laser is hard to reach deep-seated tissue and tumours. Among all different type of lasers, the near-infrared laser is the one which can comparatively deeply penetrate into tissues, and it has been used in clinical treatment of oesophageal cancer [Pietraffita and Dwyer, 1986]. In laser hyperthermia, the collateral damage to normal tissue is inevitable, since the laser is always absorbed by the normal tissues above tumours. As the results, how to avoid this problem and obtain better treatment result are very important.

In order to enhance the effect of laser hyperthermia, some new technologies have been implemented in laser hyperthermia. Hirsch *et. al* (2003) and O'Neal (2004) presented a new idea to enhance treatment effects of laser hyperthermia, and obtained very good results. Their basic idea is to inject metal nanoshells which are a class of nanoparticles with tunable optical resonances into tumours. Since these nanoparticles have strong absorption and scattering effects to near infrared light (NIR), the most of the energy of the light will be absorbed by these nanoparticles and then transferred to tumours. Therefore, the temperature of tumours is higher than normal tissues. Based on this idea, lower doses of NIR light is used in treatments and the collateral damage will be decreased.

The penetration of light in tissues can be described by Radiative Transport theory, and the calculation can be approximated by Radiative Transport Equation [Ishimaru,

1978], although for some specific cases, such as ablation of tissues by ultra short laser pulses, needs a wave propagation theory to approximate [Guo and Kim, 2003]. The modeling of laser transport in tissues has been developed with several of numerical schemes, and the most widely used numerical method is Monte Carlo scheme. Flock *et al.* (1989) presented their Monte-Carlo modeling of light propagation in highly scattering tissues, and compared with diffusion theory. Boas *et al.* (2002) developed a three-dimensional Monte Carlo model for photon migration through complex heterogeneous media. Guo *et al.* (2000) also presented their work of the radiation transport of lasers in scattering media for multi-dimensional problems. The discrete-ordinates method is another scheme used to simulate the light transport in tissues. Guo *et al.* (2003) presented their discrete-ordinate method for simulation of the laser propagation in heterogeneous tissues, and they obtained reasonable results [Guo and Kim, 2003].

The discontinuous finite element method presented in the previous chapters is another good numerical scheme to solve laser propagation in tissues. The advantages of discontinuous finite element make it a good choice to solve this kind of problems. Since the laser propagation in tissues usually needs three-dimensional model to simulate, the ability of parallelism of discontinuous finite element method can speed up the calculation if a multiple CPU machine is available.

The formulation of discontinuous finite element method for the laser transport in

tissues can be expressed as Eq. (6.1). Since lasers are induced from outside of tissues, and the light will be reflected on the interfaces between air and surface of tissues, therefore the reflection effect has to be considered in calculation. If the surfaces of tissues are considered with grey surface and the incidence intensity of laser beams is denoted by I_c , the boundary condition for the intensity at the same direction can be described as follows,

$$I(\mathbf{r}, \mathbf{s}) = \varepsilon_w I_{bw} + \frac{1 - \rho_w}{\pi} \int_{\mathbf{n} \cdot \mathbf{s} > 0} |\mathbf{n} \cdot \mathbf{s}| I d\Omega + \rho_w I_c \quad (8.1)$$

where ε is the emissivity of boundary and ρ_w is the reflectivity of the boundary.

$$\rho_w = 1 - \varepsilon_w.$$

8.2. RESULTS AND DISCUSSION

In this section, an idea case is used to show the application of the discontinuous finite element method in solving radiative heat transport in tissues caused by NIR laser beams, and some primary results will be presented.

In order to test our methodology, the following idea case will be used for simulations. Figure 8.1 shows a bulk of normal tissue, and there is a small bulk of tumour in it. The dimension of the normal tissue is $4.0 \times 4.0 \times 4.0 \text{ cm}^3$, and the dimension of cancer is $1.0 \times 1.0 \times 1.0 \text{ cm}^3$. The tumour is right at the center of the normal tissue. Although the real problem is much more complex than this idea case, the main object of

this chapter is to show the application of discontinuous finite element method in laser hyperthermia.

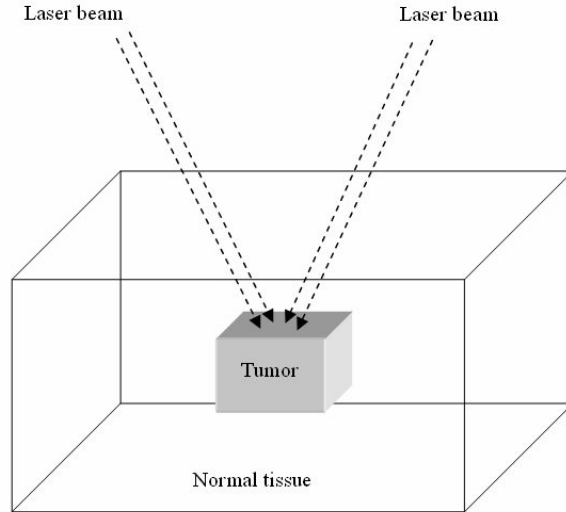


Figure 8.1. Schematic illustration of tumour, normal tissue and laser beams

In this study, in order to observe the heating effects of laser beam to the normal tissue and the tumour, several different optical properties and number of laser beams are adopted in calculation. Since we have known by injecting nanoparticles into tumours, the optical properties of the tumour can be dramatically changed. According to Hirsch *et al.*'s research (2003), the parameters of nanoparticles can be changed by using different production processes.

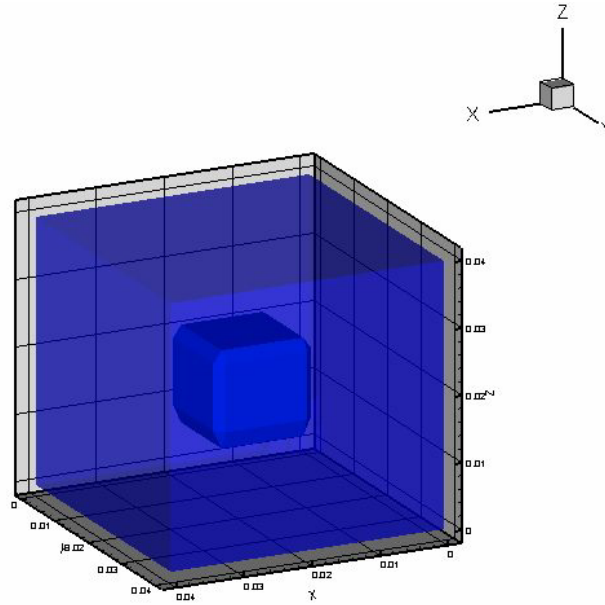


Figure 8.2. Illustration of ideal model for numerical simulation.

In Figure 8.2, the dimension of the tumour is $1.33 \times 1.33 \times 1.33 \text{ cm}^3$, and the dimension of the normal tissue is $4.0 \times 4.0 \times 4.0 \text{ cm}^3$. The tumour is right at the center of the normal tissues, and the coordinates system is as shown in Figure 8.2. The laser beams are induced on the top surface ($z = 4\text{cm}$) of the tissue. In this study, the boundary conditions of tissues are set as a diffuse grey surface boundary condition so that we can concentrate the main object of this study. Based on the above assumptions, the following mathematical model is established,

$$\left\{ \begin{array}{l} \frac{\partial I(\mathbf{r}, \mathbf{s})}{\partial s} = -\beta(\mathbf{r})I(\mathbf{r}, \mathbf{s}) + \kappa(\mathbf{r})I_b(\mathbf{r}) + \frac{\sigma(\mathbf{r})}{4\pi} \int_{4\pi} I(\mathbf{r}, \mathbf{s}')\Phi(\mathbf{s}, \mathbf{s}')d\Omega' \\ I(\mathbf{r}, \mathbf{s}) = \varepsilon_b I_{bw} + \frac{1-\rho_w}{\pi} \int_{\mathbf{n}\cdot\mathbf{s}>0} |\mathbf{n}\cdot\mathbf{s}| I d\Omega + \rho_w I_c \quad \mathbf{r} \in \Gamma_{in} \\ I(\mathbf{r}, \mathbf{s}) = \varepsilon(\mathbf{r})I_b(\mathbf{r}) + \frac{1-\varepsilon(\mathbf{r})}{\pi} \int_{\mathbf{s}'\cdot\mathbf{n}<0} I(\mathbf{r}, \mathbf{s}')|\mathbf{s}'\cdot\mathbf{n}| d\Omega' \quad \mathbf{r} \in \Gamma_b \end{array} \right. \quad (8.2)$$

where Γ_{in} denotes the portion of top surface which is applied with laser beam, and Γ_b denotes the other portion of boundary surfaces. In this study, the following parameters are used, the top surface reflectivity is 0.12, and the emissivity of all surfaces is 0.2.

In the first case, the intensity of one laser beam is set to $10000 \frac{W}{cm^2 sr}$, and the absorption and scattering coefficient of cancer is 1.0, and only one beam is used to heat the tissue and tumour. The model in Eq. 8.2 is solved by discontinuous finite element method developed in Chapter 6. The heating effect can be displayed by the radiative heat flux divergence (Divq), which is the source term in heat conduction equation, and it denotes the heating effect directly. The radiative heat flux divergence is expressed by the following equation,

$$\nabla \cdot q(\mathbf{r}) = \kappa(4\sigma T^4 - \int_{4\pi} I(\mathbf{r}, \mathbf{s})d\Omega) \quad (8.3)$$

The calculation results are plotted by program FLOWVI developed by Dr. Ben Q. Li's lab. In order to clearly show the heat generation inside of the normal tissue and the

tumour, plane section display is used to show the contour of the radiative heat flux divergence.

At first, two cases are used to show how the different optical parameters of normal tissue and tumour give different results. The first figure is used to show the divergence of radiative heat flux distribution in the normal tissue and the tumour if their optical parameters, absorption coefficient and scattering coefficient, are the same; both scattering coefficient and absorption coefficient are 1.0 m^{-1} . As shown in Figure 8.3, it clearly shows the energy from laser beam penetrates the normal tissue and the tumour, and heat generation in both places are almost the same. This is not good for laser hyperthermia, since when the tumour is heated and destroyed by laser, the normal tissue will be also damaged or destroyed, this result is what we want to avoid in clinical trial.

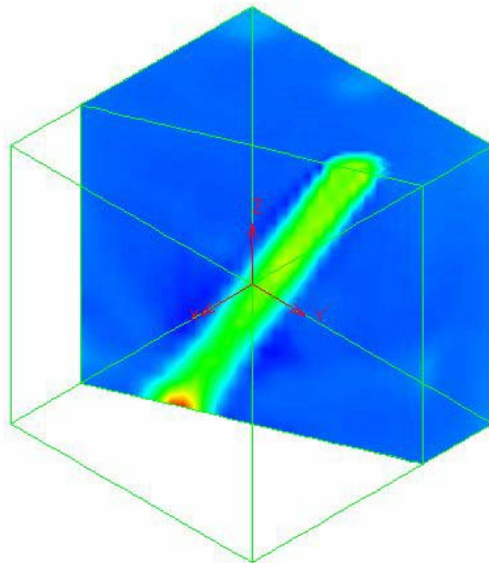


Figure 8.3 Radiative heat flux divergence at both absorption and scattering coefficients of

tissue and cancer are 1.0m^{-1} .

The second result is the distribution of divergence of radiative heat flux when the optical parameters of the normal tissue and the tumour are different. In this case, the absorption coefficient of normal tissue is 0.5m^{-1} , and the scattering coefficient is 1.0m^{-1} ; the absorption coefficient of the tumour is 1.0m^{-1} , and the scattering coefficient is 10.0m^{-1} . The intensity of incident laser beam is $10000 \frac{w}{\text{cm}^2 \text{sr}}$. The calculation result is shown as in Figure 8.5. In this case, we can see the energy of laser beam absorbed by the tumour is much more than absorbed by normal tissue. This result proves the different optical parameters affect the effect of laser hyperthermia.

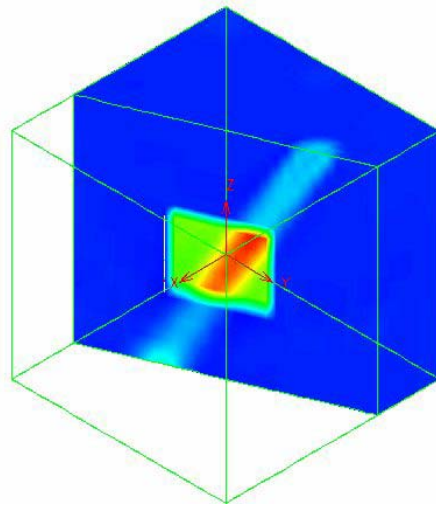


Figure 8.4 Distribution of the radiative heat flux at the following optical parameters: The absorption coefficient of skin is 0.5m^{-1} , scattering coefficient is 1.0m^{-1} ; the absorption coefficient of cancer is 1.0m^{-1} , scattering coefficient is 10.0m^{-1}

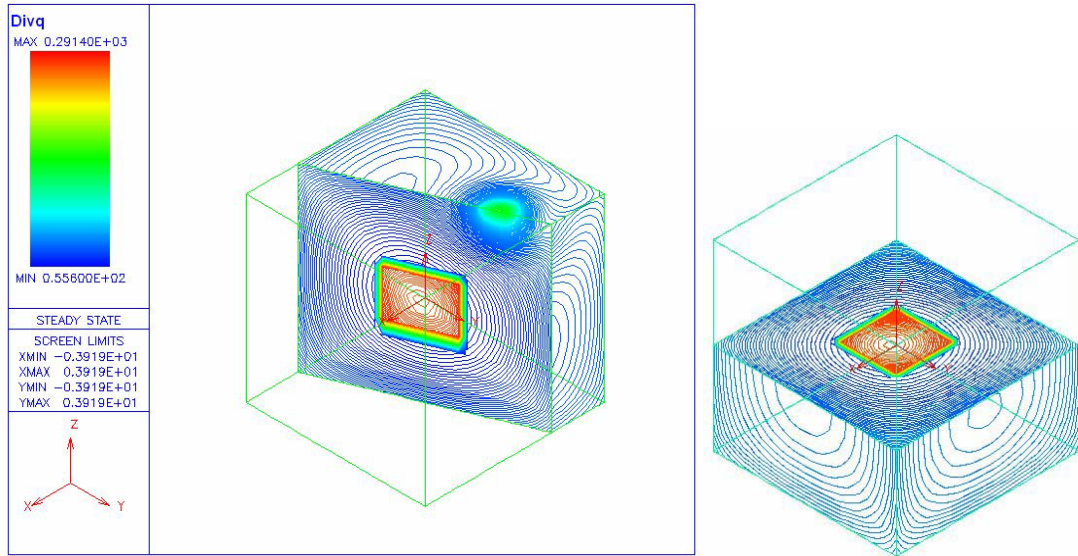
From the above two cases, we have known optical parameters affect the laser hyperthermia greatly. Although the energy absorbed by normal tissue is less than absorbed by the tumour, as shown in the above cases, the normal tissue is still heated by laser beam; especially the absorption coefficient and scattering coefficient of the normal tissue and the tumour are at the same magnitude. In order to decrease the energy absorbed by the normal tissue, instead of using one high power laser beam, we can focus multiple lower power laser beams to tumours, just like convex lens effect. By author's knowledge, this idea has not been found in other references so far. As shown in Figure 8.1, two laser beams are used to heat the tumour. The laser beams are not vertically applied on the top surface of the tissue, but with a certain angle so that they can focus at the center of the tumour. In the following cases, one, two, and four laser beams are applied on the top surface of the normal tissue respectively and the radius of laser beam is 0.3 cm. The distribution of radiative heat flux divergence will be calculated based on the different laser beam schemes.

The following cases show the effects of different number of laser beams in laser hyperthermia. In these cases, the optical parameters of normal tissue are from Guo's work (2000), the absorption coefficient of normal tissue is 0.01cm^{-1} and scattering coefficient is 10cm^{-1} . The absorption coefficient and scattering coefficient of tumour are set to 5 times of parameters of the normal tissue. The intensity of incident laser beam

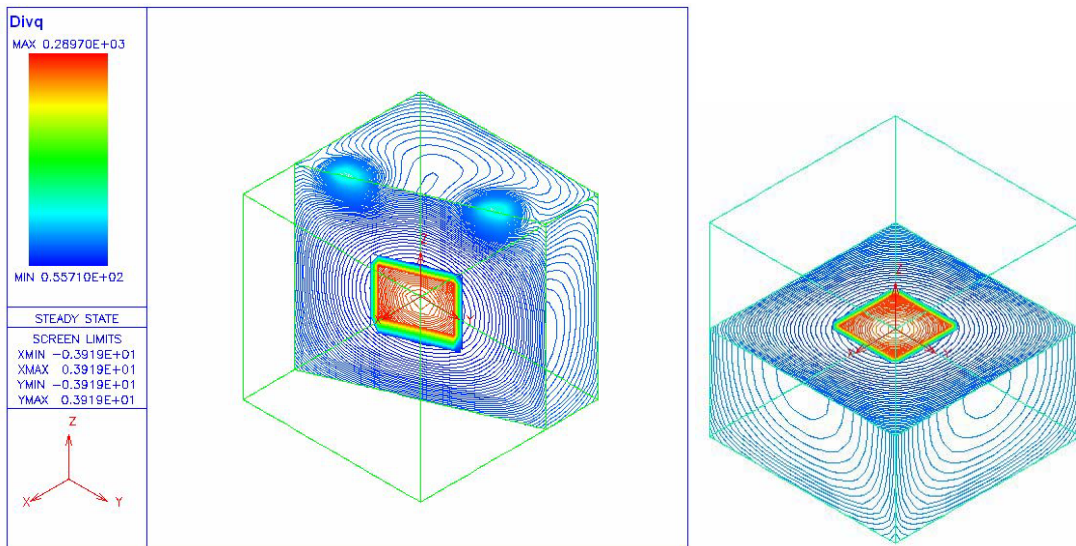
is $10000 \frac{w}{\text{cm}^2 \text{sr}}$ for one beam, $5000 \frac{w}{\text{cm}^2 \text{sr}}$ for each of two laser beams, and $2500 \frac{w}{\text{cm}^2 \text{sr}}$

for each of four laser beams. The distribution of the radiative heat flux divergence is

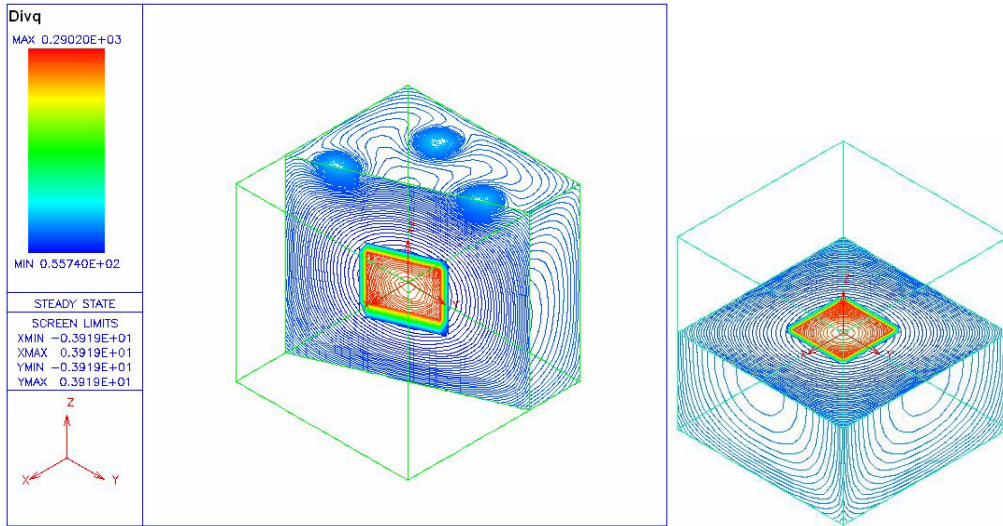
shown in Figure 8.5 (a), (b), and (c).



(a)



(b)



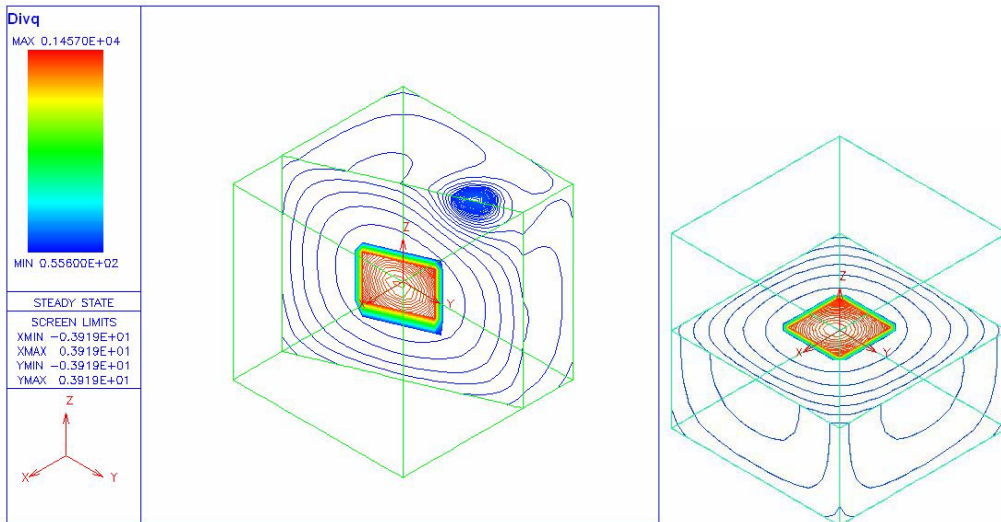
(c)

Figure 8.5 Vertical and horizontal section plane display of the distribution of the radiative heat flux divergence for three different laser beam schemes; the absorption coefficient of the normal tissue is 0.01cm^{-1} , and the scattering coefficient of the normal tissue is 10cm^{-1} ; the absorption coefficient of the tumour is 0.05cm^{-1} , and the scattering coefficient of the tumour is 50cm^{-1} . (a): one laser beam, and the intensity of is $10000\frac{w}{\text{cm}^2\text{sr}}$. (b) two laser beams, and the intensity of each laser beam is $5000\frac{w}{\text{cm}^2\text{sr}}$; (c) four laser beams, and the intensity of each laser beam is $2500\frac{w}{\text{cm}^2\text{sr}}$.

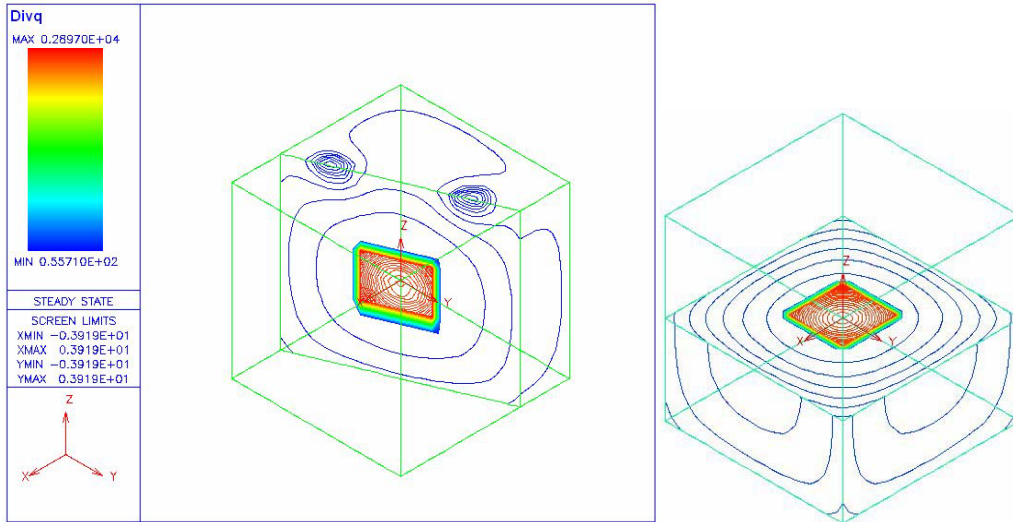
Comparing the results of above three different laser beam scheme, we can find the radiative heat flux divergence in the tumour keeps almost the same in three different laser beam schemes, and the maximum values in three different schemes are close to $290\frac{w}{\text{cm}^3}$. But the radiative heat flux distributions near the incident point of laser beams are clearly

different. In the one-beam scheme, the value at the incident point of laser beam is the highest in the three schemes; four-beam scheme gets the lowest value, and two-beam gets the value in the middle of one-beam results and four-beam results. The above results prove that the idea of multiple low power laser beams scheme works.

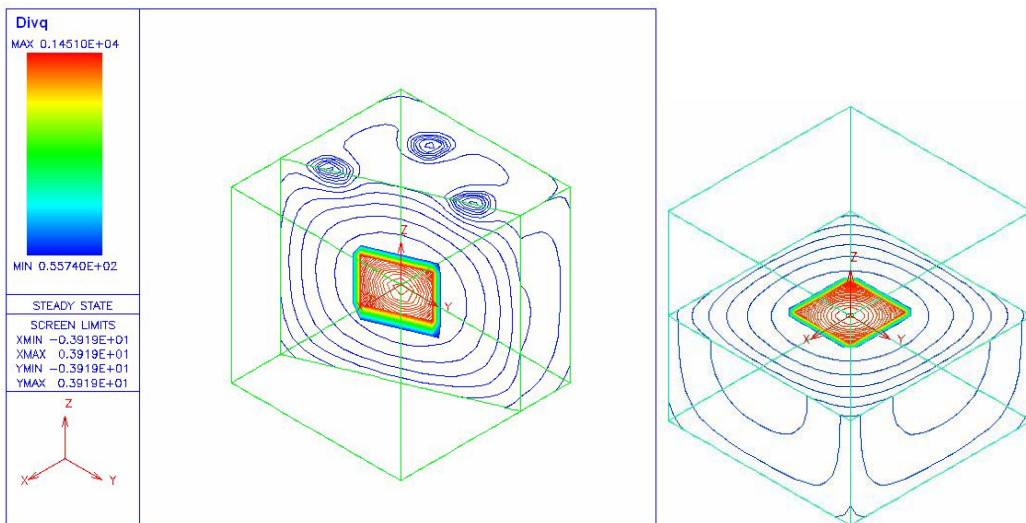
Besides the above simulations for different laser beam schemes, more simulations with different optical parameters have been done. Figure 8.6 shows the distribution of divergence of radiative heat flux with three different laser schemes at the condition that the absorption coefficient and scattering coefficient of the tumour are 25 time of the coefficients of the normal tissue.



(a)



(b)



(c)

Figure 8.6. The distribution of the divergence of radiative heat flux for three different laser beam scheme; the absorption coefficient of the normal tissue is 0.01 cm^{-1} , and the scattering coefficient of the normal tissue is 10 cm^{-1} ; the absorption coefficient of the tumour is 0.25 cm^{-1} , and the scattering coefficient of the tumour is 250 cm^{-1} . (a) one laser

beam, and the intensity of is $10000 \frac{w}{cm^2 sr}$. (b) two laser beams, and the intensity of each laser beam is $5000 \frac{w}{cm^2 sr}$; (c) four laser beams, and the intensity of each laser beam is $2500 \frac{w}{cm^2 sr}$.

Compared with Figure 8.5, the maximum radiative heat flux divergence in Figure 8.6 is higher than the maximum radiative heat flux divergence in Figure 8.5. The maximum of radiative heat flux divergence in Figure 8.5 is 290, but in Figure 8.6, the maximum is 1457. The reason is the absorption coefficient and scattering coefficient in Figure 8.6 is greater than the coefficients in Figure 8.5, which means more energy is absorbed by the tumour.

8.3 CONCLUSION REMARK

This chapter presented a discontinuous finite element (DFE) modeling for the laser hyperthermia. The laser transport in a 3-D geometry model is calculated. The computation results explained the reasons of great effects of injecting nanoparticles into tumour. This is a very important application in laser hyperthermia. The discontinuous finite element model and numerical implementation for laser hyperthermia calculations were given. A new idea of using multiple lower power laser beams in laser hyperthermia was introduced, and detailed discussion and computation results of different laser beam scheme were presented. The computation results show the new idea gives a good result in

laser hyperthermia, and it has a great potential in real applications.

BIBLIOGRAPHY

Ainsworth, M. and Oden, J. T., 2000, A Posteriori Error Estimation in Finite Element Analyses. Wiley, New York, NY.

Asadzadeh, M., 1998, A Finite Element Method for the Neutron Transport Equation In An Infinite Cylindrical Domain, *SIAM J. Numer. Anal.*, vol. 35, pp.1299-1314.

Bastian, M. and Li, B. Q., 2002, An Efficient Automatic Mesh Generator for Quadrilateral Elements Implemented Using C++, *Finite elements in Analysis and Design*.

Bennett, T. D., 2003, Complex Combination Solution for Radiation-conduction Transport with Periodic Boundary Conditions, *Int. J. Heat Mass Transfer*, vol. 46, pp. 2341-2351.

Blobner, J., Bialecki, R. A. and Kuhn, G, 2001, Boundary Element Solution of Coupled Heat Conduction-Radiation Problems in the Presence of Shadow Zones, *Numerical Heat Transf., Part B.*, Vol. 39, 451-478.

Boas, D. A., Culver, J. P., Stott, J. J., and Dunn, A. K. 2002, Three Dimensional Monte Carlo Code for Photon Migration Through Complex Heterogeneous Media Including the Adult Human Head, *Opt. Express*, vol. 10, pp159-170.

Brebbia, C., Telles, J. and Wrobel, L., 1984, *Boundary element techniques*. New York, NY: Springer.

Breitbach, G., Altes, J. and Sczimarowsky, M., 1988, Solution of radiative problems using variational based finite element method, *Int. J. Numer. Meth. Eng.*, vol. 29, pp. 1701-1714.

Burns, S. P. and Christon, M. A, 1997, Spatial Domain-Based Parallelism In Large-Scale, Participating-Media Radiative Transport Applications, *Numerical Heat Transfer, Part B*, Vol 31, pp. 401-421.

Chai, J. C., and Patankar, S. V., 2000, Finite-Volume Method for Radiation Heat Transfer, *Advances in Numerical Heat Transfer*, vol. 2, Chapter 4, Taylor & Francis, pp. 109 – 138.

Chandrasekhar, S., 1960, *Radiative Transfer*, Dover Publications, Inc., New York.

Chui, E. H., and Raithby, G. D., 1992, Prediction of Radiative Transfer in Cylindrical Enclosures with the Finite Volume method, *J. Thermophys. Heat Transfer*, vol. 6, pp. 605-611.

Chui, E. H., and Raithby, G. D., 1993, Computation Of Radiant Heat Transfer On A Non-Orthogonal Mesh Using The Finite-Volume Method, *Numerical Heat Transfer, Part B*, Vol. 23, Pp.269-288.

Chung, T. J. and Kim, J. Y., 1982, Radiation view factors by finite elements, *J. heat transfer*, vol. 104, pp. 792-295.

Cui, X. and Li, B. Q., 2004a, A Discontinuous Finite Element Formulation for Internal Radiation Problems, *Numer. Heat Transfer B*, vol.46, pp.223.-242.

Cui, X. and Li, B. Q., 2004b, A Discontinuous Finite element Formulation for Multi-dimensional Radiative Transfer in Absorbing, Emitting and Scattering Medium, *Numer. Heat Transfer B*, vol. 46, pp.399-428.

Cockburn, B., Karniadakis, G. E., and Shu, C-W., 2000, The development of discontinuous Galerkin methods. in *Discontinuous Galerkin Methods: Theory, Computation and Applications*. (Ed. B. Cockburn, G. E. Karniadakis, and C-W. Shu), Springer-Verlag, Berlin.

Dupret, F., Nicodeme, P., Ryckmans, Y., Wouters, P., Crochet, M. J., 1990, Global Modeling of Heat Transfer in Crystal Growth Furnaces. *International Journal of Heat and Mass Transfer*, vol.33, n.9, pp.1849–1871.

Cumber, P. S., And Beerli, Z., 1998, A Parallelization Strategy For The Discrete Transfer Radiation Model, *Numerical Heat Transfer, Part B*, Vol 34, pp. 401-421.

Emery, A. F., Johansson, and Abrous, A., 1987, Radiation Heat Transfer Shape Function for Combustion Systems, in A. M. Smith (eds.), *Fundamental and applications of radiation heat transfer*, ASME HTD, vol. 72, pp.119-126.

Fernandes, R. and Francis, J., 1982, Combined Conductive and Radiative Heat Transfer in an Absorbing, Emitting, and Scattering Cylindrical Medium, *J. Heat Transfer*, vol. 104, pp. 594-601.

Fiveland, W. A., 1982, A Discrete-Ordinates Method for Predicting Radiative Heat Transfer in Axisymmetric Enclosure, American Society Of Mechanical Engineering, Paper 82-HT-20.

Fiveland, W. A., 1991, The selection of discrete ordinate quadrature sets for anisotropic scattering, *Fundam. Radiation heat Transfer* HTD-160, pp.89-96.

Flock, S. T., Patterson, M. S., Wilson, B. C. and Wyman, D. R., 1989, Monte-Carlo modeling of light propagation in highly scattering tissues. I. prediction and comparison with diffusion theory, *IEEE Trans. Biomed. Eng.* Vol. 36, pp. 1162-1168.

Foley, J. D., 1997, *Computer Graphics: Principles and Practice*. Addison-Wesley Publishing Company, MA.

Gerweck, L.E., 1985, Hyperthermia in cancer therapy: The biological basis and unresolved questions, *Cancer Res.* Vol. 45: pp. 3408-3414.

Guo, Z., Kumar, S., and San, K. C., 2000, Multi-dimensional Monte Carlo simulation of short pulse laser radiation transport in scattering media, *J. Thermophys. Heat Transfer*, vol. 14, pp. 504-511.

Guo, Z., and Kim, K., 2003, Ultrafast-Laser-Radiation Transfer in Heterogeneous Tissues with the Discrete-Ordinates Method, *Applied Optics*, Vol. 42, n. 16, pp.2897-2905.

Hergt, R., Andr̃a, W.; d'Ambly, C. G., Hilger, I., Kaiser, W. A., Richter, U., and Schmidt, H., 1998, Physical Limits of hyperthermia using magnetic fine particles, *IEEE Transaction on Magnetics*, vol. 34., n.5, pp. 3745-3754.

Hirsch, L. R., Stafford, R. J., Bankson, J. A., Sershen, S. R., Rivera, B., Price, R. E., Hazle, J. D., Hala, N. J., and West, J. L., 2003, *Proc Natl Acad Sci USA.* , vol. 100, n.23, pp.13549-13554.

Honda, J., Zhang, C., Li, B. Q. and de Groh, H. C., 2001, A 3-d model for magnetic damping of g-jitter induced convection and solutal transport in a simplified Bridgman configuration, in *Proceedings of the ASME Heat Transfer Division*, New York ; Paper #: IMECE2001/HTD-24291: 1-18.

Hottel, H. C., 1931, Radiant heat transmission between surfaces separated by non-absorbing media, *Trans ASME*, vol. 53, pp. 265-273.

Howell, J. R. and Perlmutter, M., 1964, Monte Carlo solution of thermal transfer through radiant media between gray walls, *J. Heat transfer*, vol. 86, pp. 116-122.

Hughes, T. J. R., Engel, G., Mazzei, L., and Larson, M. G., 2000, A Comparison of Discontinuous and Continuous Galerkin Methods Based on Error Estimates, Conservation, Robustness And Efficiency. in *Discontinuous Galerkin Methods: Theory, Computation and Applications*. (Ed. B. Cockburn, G. E. Karniadakis, and C-W. Shu), Springer-Verlag, Berlin, pp. 135-146.

Jendoubi, S. and Lee, H. S., 1993, Discrete Ordinates Solutions for Radiatively Participating Medium in a Cylindrical Enclosure, *J. Thermophys. Heat Transfer*, vol. 7, pp. 213-219.

Johnson, C., 1987, Numerical solution of partial differential equations by the finite element method, Cambridge University.

Ishimaru, A., 1978, Wave propagation and scattering random media, Academic Press, New York.

Kim, T. K. and Lee, H., 1988, Effect of Anisotropic Scattering on Radiative Heat Transfer in Two-Dimensional Rectangular Enclosures, *J. Heat Transfer*, vol. 31, pp.1711-1721.

Kobayashi, M., Tsukada, T. and Hozawa, M., 1997, Effect of Internal Radiative Heat Transfer on the Convection in CZ Oxide Melt, *Journal of Crystal Growth*, vol. 180, pp. 157-166.

Koenigsdorff, R., Miller, F. and Ziegler, R., 1991, Calculation of scattering fractions for use in Radiative flux models, *Int. J. Heat Mass Transfer*, vol. 34, no. 10, pp. 2673-2676.

Kuppurao, S., and Derby, J. J., 1993, Finite element formulations for accurate calculation of radiant heat transfer in diffuse-grey enclosures. *Numerical heat transfer, B*, vol. 24, pp. 431-454.

Lan, C. H., Ezekoye, O. A., Howell, J. R. and Ball, K. S., 2003, Stability Analysis for Three-dimensional Rayleigh–Bénard Convection with Radiatively Participating Medium Using Spectral Methods, *Int. J. Heat Mass Transfer*, vol. 46, pp. 1371-1383.

Lathrop, K. D. and Carlson, B. G. 1965, Discrete Ordinates Angular quadrature of the

neutron transport equation, LA-3186, UC-32 Mathematics and Computers TID-4500 (36th Ed.).

Leper, D. B., 1984, Molecular and cellular mechanisms of hyperthermia alone or combined with other modalities, in Hyperthermic oncology, J. Overgaard, ed., Taylor and Francis. London.

McGahan, J. P., Browning P. D., Brock J. M., Tesluk H. 1990, Hepatic ablation using radiofrequency electrocautery. *Invest Radiol*; Vol. 25, pp.267-270.

Moder, J. P, Kumar, G. N., and Chai, J. C., 2000, An Unstructured-Grid Radiative Heat Transfer Module For The National Combustion Code, 38th Aerospace Sciences Meeting & Exhibit, Reno, NV.

Modest, M. F., 1993, *Radiative Heat Transfer*, New York: McGraw-Hill.

Murthy, J. Y. and Mathur, S. R., 1998a, Radiative Heat Transfer in Axisymmetric Geometries Using an Unstructured Finite-Volume Method, *Numer. Heat Transfer B*, vol. 33, pp. 397-416.

Murthy, J. Y., and Mathur, S. R., 1998b, Finite Volume Method For Radiative Heat Transfer Using Unstructured Meshes. *Journal Of Thermophysics And Heat Transfer*, Vol.12, No. 3, pp. 313-321.

Naraghi, M. N., and Chung, B. T. F., 1984, A stochastic approach for radiative exchange in enclosures with nonparticipating medium, *J. Heat Transfer*, vol. 106, pp.690-698.

Nazir, B., Chaturvedi, A. K., and Rao, A., 2003, Image-Guided Radiofrequency Ablation of Tumours: Current Status, *Ind J Radiol Imag*, Vol. 13, n.3, pp.315-322.

Nusselt, W., 1928, Graphische bestimmung des winkilverhaltiness bei der Wärmestrahlung, *VDI Z.*, vol 72, pp.673.

Oden, J. T., Babuka, I. and Baumann, C., 1998, A discontinuous hp finite element method for diffusion problems, *Journal of Computational Physics*, vol. 146, n. 2, pp.491-519.

Oden, J., and Carey, G., *Finite elements V: Mathematical Foundations*, Prentice Hall, 1983.

O'Neal, D. P., Hirsch, L. R., Halas, N. J., Payne, J. D. and West, J. L., 2004, Photothermal Tumour Ablation in mice using near infrared absorbing nanoshells. *Cancer Letters*, 209, pp.171-176.

Özisik , M. N., 1973, *Radiative Transfer And Interactions With Conduction And Convection*, Wiley-Interscience, New York, 1973.

Pietraffita, J., and Dwyer, R., 1986, Endoscopic laser therapy of malignant esophageal obstruction, *Arch. Surg.* Vol. 121, pp. 395-400.

Raithby, G. D., and Chui, E. H., 1990, A Finite-Volume Method for Predicting a Radiant Heat Transfer in Enclosure with Participating Media, *J. Heat Transfer*, vol. 112, pp. 415-423.

Rogers, D., 1998, *Procedural elements for computer graphics*. McGraw-Hill, New York.

Schuster, A., 1905, Radiation through a foggy atmosphere, *Astrophysical journal*, vol. 21, pp1-22.

Schwarzschild, K., 1906, Über das gleichgewicht der sonnenatmosphären, akademie der wissenschaften in goettingen, *Nachrichten. Mathematisch-physikalische klasse*, vol. 1, pp.41-53.

Shu, Y., Li, B. Q. and Lynn, K. G., 2004, Numerical Modeling of Internal Radiation and Solidification in Semitransparent Melts in Magnetic Field, *Numer. Heat Transfer A*, vol. 45, pp. 1-20.

Siegel, R. and Howell, J. R., 1992, *Thermal Radiation Heat Transfer*, 3rd Ed. Washington, D.C.: Hemisphere Publishing Company.

Song, S. P. and Li, B. Q., 1998, Boundary/finite Element Analysis of Magnetic Levitation Systems: Surface Deformation And Thermal Phenomena, *J. Heat Transfer*, vol. 120, pp. 492-504.

Song, S. P. and Li, B. Q., 1999, Coupled Boundary/Finite Element Computation of Magnetically and Electrostatically Levitated Droplets, *Int. J. Num. Meth. Eng.* vol. 44, n.8, pp.1055-1077.

Song, S. P. and Li, B. Q., 2001, Finite element computation of shapes and Marangoni convection in droplets levitated by electric fields, *Int. J. Comp. Fluid Dynamics*, vol. 15, pp.293-308.

Song, S. P., Li, B. Q. and K. G. Lynn, 2003, An Integrated Model for Czochralski Melt Growth of Optical Crystals, ASME Heat Transfer Summer Conference, Los Vegas, HT2003-40403.

Sparrow, E. M., 1960, Application of variational methods to radiation heat transfer calculations, *J. of Heat Transfer*, Transactions of ASME, Series C82 (4), pp.375-380.

Steward, F. R. and Cannon, P., 1971, the calculation of radiative heat flux in a cylindrical furnace using the Monte-Carlo method / *Int. Journal of Heat & Mass Transfer*. vol. 14, n.2, pp.45-261.

Sturesson, C., 1998, Medical Laser-Induced Thermotherapy Models and Applications, Ph.D. dissertation, Lund Institute of Technology.

Wiscombe, W. J., 1980, Improved Mie Scattering Algorithms, *Appl. Optics* Vol. 19, no 9, pp.1505-1509, 1980.

Zhang, X., 2001, Data visualization and mesh generation for finite element simulation of fluid flow and heat transfer, MS. Thesis, Washington State University, Pullman.

Zienkiewicz, O. C., and Taylor, R. L., 1989, *The Finite Element Method*. McGrawHill.